INVESTIGATION OF SINGLE CRYSTAL AND BI-CRYSTAL DEFORMATION IN BODY-CENTERED CUBIC TANTALUM USING INDENTATION

By

Bret Elliott Dunlap

A DISSERTATION

Submitted to
Michigan State University
in partial fulfillment of the requirements
for the degree of

Materials Science and Engineering – Doctor of Philosophy

2018

ABSTRACT

INVESTIGATION OF SINGLE CRYSTAL AND BI-CRYSTAL DEFORMATION IN BODY-CENTERED CUBIC TANTALUM USING INDENTATION

By

Bret Elliott Dunlap

To understand how polycrystalline tantalum (Ta) deforms and develops damage that can lead to fracture, it is necessary to have an understanding of the single crystal deformation as well as deformation at grain boundaries. Metallic crystals generally deform from the motion of dislocations on crystallographic planes and this motion is dependent on the orientation of the individual crystals in relation to the imposed deformation. In order to study the effects that crystal orientation and grain boundaries have on deformation, as well as quantify and characterize the dislocations involved, three primary experiments were carried out.

The first set of experiments involved single crystal microindentation, single crystal nanoindentation, and bi-crystal nanoindentation. The topographies developed were mapped using confocal microscopy for microindentations and atomic force microscopy (AFM) for nanoindentations. The single crystal indents revealed the effect crystal orientation has on topography and the bi-crystal nanoindentations reveal the effect that grain boundaries have on topography. In this work, three grain boundaries were targeted for analysis, with one indent made on each side of the grain boundary. Analysis shows that deformation across the grain boundary is dependent on the side from which deformation is approaching. The single crystal and bi-crystal nanoindentations were coupled with crystal plasticity finite element modeling (CPFEM) simulations in order to compare the experiments with predictive models.

The second set of experiments characterized and quantified the dislocations involved in the underlying plastic deformation of single crystal and bi-crystal nanoindentations using

electron channeling contrast imaging (ECCI) and cross-correlation electron backscattered diffraction (CC-EBSD). ECCI directly images and characterizes dislocations using contrast analysis. On the other hand, CC-EBSD calculates the geometrically necessary dislocation (GND) density from the subtle shifts in the EBSD patterns. CC-EBSD can also split the GND density onto the specific slip systems. The effectiveness of these two techniques to quantify and characterize dislocations were compared and the advantages and disadvantages of both outlined.

In the third experiment, the sub-surface deformation of a single crystal wedge indentation was analyzed using ECCI and EBSD. The wedge indentation was specifically aligned to the crystal orientation so that when the sample was cut in half, all deformation was manifested as plane-strain in the analyzed surface plane. ECCI and EBSD were carried out on a small area underneath the area where the indenter tip was in contact with the sample. Backscattered electron (BSE) imaging and EBSD mapping reveal thin needle like bands that resemble that of twinning. The crystal orientation alternates between thin bands of rotated crystal orientation and thick bands of the original crystal orientation. ECCI shows high dislocation densities within the bands and at the boundaries between bands. Due to the fact that the alternating banding leaves no residual lattice curvature, it is concluded that all dislocations within a given band are statistically stored dislocations (SSDs).

This work reveals that the surface topography and the dislocation distributions that result from indentation reflect the symmetry of the indented crystal orientation. Also, deformation at grain boundaries is dependent on the direction from which deformation is approaching. Even further, this work shows that the combination of indentation, AFM, ECCI, and CC-EBSD is a great method for investigating deformation but the limitations of each of these tools need to be understood in order to be fully utilized

For all of my family. Thank you for encouraging me to do the things I thought were impossible.

ACKNOWLEDGEMENTS

First, I would like to thank my advisor, Dr. Martin Crimp, for his guidance throughout my PhD work. His influence has greatly enhanced my growth as a researcher, writer, and as an overall person. I have thoroughly appreciated our discussions that have covered research and non-research related topics.

I would also like to thank my committee members, Dr. Philip Eisenlohr, Dr. Thomas Bieler, and Dr. Rebecca Anthony, for their guidance and their flexibility that allowed them to be easily accessible to discuss ongoing research. I also want to thank Dr. Carl Boehlert for insightful feedback in group meeting discussions. I would like to thank Dr. Per Askeland as well as former and current graduate students in the "metals group" for helping me learn how to use scanning electron microscopes and other research equipment.

Most of all, I want to thank my wife Michelle for all of her loving support throughout my undergraduate and graduate work.

TABLE OF CONTENTS

LIST OF TABLES

LIST OF FIGURES

KEY TO ABBREVIATIONS AND SYMBOLS

AFM	atomic force microscopy
bcc	body-centered cubic crystal structure
BSE	backscattered electron
CC-EBSD	cross-correlation electron backscattered diffraction
CPFEM	crystal plasticity finite element modeling
Cr	chromium
CRSS	critical resolved shear stress
EBSD	electron backscattered diffraction
ECCI	electron channeling contrast imaging
ECP	electron channeling pattern
EDM	electronic discharge machining
fcc	face-centered cubic crystal structure
Fe-Si	iron-silicon alloy
FEG-SEM	field emission gun scanning electron microscope
FEM	finite element methodology
FIB	focused ion beam
GNDs	geometrically necessary dislocations
GUI	graphical user interface
hcp	hexagonal close-packed crystal structure
Mo	molybdenum
MPIE	Max-Planck-Institut für Eisenforschung GmbH

Nb	niobium
OIM	Orientation Imaging Microscopy
ROIs	regions of interest within an EBSD pattern
SACP	selected area channeling pattern
SEM	secondary electron microscopy
SiC	silicon carbide
SSDs	statistically stored dislocations
Ta	tantalum
TEM	transmission electron microscopy
VTK	visualization toolkit file
α	electron diffraction angle larger than the Bragg angle
α_{ij}	Nye tensor
$\mathbf{b}$	Burgers vector
β-brass	body-centered cubic structure of brass
$\mathbf{C}$	elastic tensor
$\mathbf{C}_{44}$	elastic modulus
η	describes electron backscattered yield
$\mathbf{F}$	deformation gradient
$\mathbf{F}_e$	elastic deformation gradient
$\mathbf{F}_p$	plastic deformation gradient
$\mathbf{g}$	vector that describes the electron imaging/channeling condition
$\mathbf{g}_1$, $\mathbf{g}_2$	unit vectors along the slip directions
$\dot{\gamma}$	shear rate

$\dot{\gamma}_0$	reference shear rate
$h_{\alpha\beta}$	hardening matrix
κ	angle between slip directions
$\mathbf{L}_1$, $\mathbf{L}_2$	unit vectors along the intersection lines slip planes make with the grain boundary
λ	angle between slip direction and direction of uniaxial stress
$\mathbf{L}_p$	sum of shear rates on all possible slip systems
M	predictive parameter of slip transfer using θ and κ
$\frac{1}{m}$	rate sensitivity of slip
m	Schmid factor
$\mathbf{m}$	slip direction of a dislocation
m'	predictive parameter of slip transfer using κ and Ψ
$\mathbf{n}$	slip plane
ω	electron diffraction angle smaller than the Bragg angle
ϕ	angle between slip plane normal and direction of uniaxial stress
$q_{\alpha\beta}$	latent hardening matrix
$\mathbf{S}$	stress
Ψ	angle between slip plane normals
σ	macroscopic stress
σ_{ys}	yield stress
τ	resolve shear stress
τ_c	critical resolved shear stress
τ_s	saturation value of the shear stress
θ_B	Bragg angle

θ	angle between $\mathbf{L}_1$ and $\mathbf{L}_2$
$\mathbf{u}$	dislocation line direction

1 Introduction

Due to the body-centered cubic (bcc) structure of tantalum (Ta), the deformation mechanisms are complicated, causing it not the follow the widely accepted Schmid's law [1–3]. In order to fully utilize the properties of Ta in its various applications [4, 5], an understanding of its deformation mechanisms is necessary; particularly, the transfer of strain across grain boundaries. The purpose of this work is to quantify and characterize the deformation that occurs within individual grains and at grain boundaries from nanoindentation induced deformation in bcc Ta.

By and large, metals are comprised of many grains, in which each grain has its own crystal orientation. These crystals deform from dislocation motion on crystallographic planes and the deformation of each crystal is dependent upon the stress state placed on it. To understand how polycrystals deform and develop damage that leads to fracture, it is necessary to characterize the dislocations involved in the underlying plastic deformation. This dislocation content is made up of both the statistically stored dislocations (SSDs), consisting of the portion of the overall dislocation density that effectively cancels itself out, i.e. due to dislocation dipoles, and the geometrically necessary dislocations (GNDs) that are associated with the crystal elastic strain gradients that develop through plastic deformation.

In order to accommodate large scale deformation, interactions occur between the dislocations and grain boundaries. Ultimately, these interactions will lead to strain transfer across the grain boundary or create a potential sight for damage nucleation, which can lead to fracture. There are four general mechanisms [6] that represent the interactions between dislocations and grain boundaries. They include: (1) transmission of dislocations across the grain boundary; (2) absorption of dislocations into the grain boundary; (3) absorption, followed

by emission into the neighboring grain; and (4) reflection off the grain boundary back into the parent grain. Generally speaking, each of these will cause the energy of the grain boundary to increase by some degree depending on the specifics of the interaction, i.e. the residual Burgers vector stored in the boundary following the interaction.

In order to quantify and characterize the deformation that occurs within individual grains and at grain boundaries from indentation induced deformation in bcc Ta, three primary experiments were carried out. The first involved single crystal microindentation, single crystal nanoindentation, and bi-crystal nanoindentation in order to view the effects that crystal orientation and grain boundaries have on the topographical lobes formed from indentation. The single crystal and bi-crystal nanoindentation experiments were coupled with crystal plasticity finite element modeling (CPFEM) simulations of the nanoindentation process. The second set of experiments characterized and quantified the dislocations formed from nanoindentation in single crystals and near grain boundaries. The characterization and quantification was carried out using electron channeling contrast imaging (ECCI) and cross-correlation electron backscattered diffraction (CC-EBSD). The efficacy of these two techniques were compared and the advantages and disadvantages of both outlined. The third experiment involved characterizing the sub-surface deformation of single crystal Ta deformed from wedge indentation.

1.1 Generalized slip

Crystals commonly deform by dislocations moving on the crystallographic planes that have the highest planar atomic density with the atomic displacements, caused by dislocations, in the directions that have the highest linear atomic density. These planes are referred to as the slip planes and the direction of atomic displacements are known as the Burgers vectors. The

combinations of individual slip planes and the individual Burgers vectors that lie in those planes make up the slip systems of the various crystal systems [7].

Knowing the orientation of a given crystal, along with its possible slip systems, slip trace analysis can be performed on a deformed sample. Slip trace analysis is a method by which the active slip systems can be identified from slip lines that appear on the surface following deformation. This was first done with optical microscopy [8], but it can also be performed using electron microscopy [9–11]. Slip trace analysis has been well demonstrated in the crystal structures of hexagonal close-packed (hcp) and face-centered cubic (fcc) and the slip systems that were found to be active in these crystal structures predominately follow Schmid's law [1, 12].

1.1.1 Predictive Parameters of Slip

Schmid's law can be used to predict when a given crystal will begin to deform and on which slip systems deformation will occur in single crystals. Schmid's law states that a macroscopic stress is resolved onto the specific slip systems and when the stress is uniaxial it can be represented by:

$$\tau = \sigma * m \qquad (1.1)$$

$$m = \cos\phi \cos\lambda \qquad (1.2)$$

where τ is the resolved shear stress, σ is the macroscopic stress, and m is referred to as the Schmid factor. ϕ and λ are the angles the plane normal and slip direction make with the direction of uniaxial stress, respectfully. According to Schmid's law, plastic flow will occur on a given slip system when the resolved stress reaches a critical value, known as the critical resolved shear stress (CRSS). It is important to realize that the CRSS is dependent on the material and

varies for the different slip systems within that material. In part, the CRSS values are different for the various slip planes due to the Peierls stress.

Analogous to the Schmid factor predicting slip in single crystals, predictive parameters of slip transfer at grain boundaries have been developed. Lee et al. [13] suggested that three conditions are needed to determine the active slip systems in slip transfer; the geometric condition, the resolved shear stress condition, and the residual grain-boundary dislocation condition. The geometric condition represents the angle between incoming and outgoing slip planes at the grain boundary, which should be minimized. The resolved shear stress condition says that the resolved shear stress acting on the outgoing plane by the pile up of dislocations needs to be maximized. Finally, the residual grain-boundary dislocation condition says that the difference between incoming and outgoing Burgers vectors needs to be minimized [13].

One slip transfer parameter proposed by Luster and Morris [14] is referred to as *m'*:

$$m' = \cos\Psi \cdot \cos\kappa \qquad (1.3)$$

where Ψ is the angle between the closest slip planes in neighboring grains and κ is the angle between the closest slip directions that lie within the slip planes. Deviating from one of the conditions proposed by Lee et al., *m'* does not account for the resolved shear stress condition [15, 16], meaning the closest slip planes between in the neighboring grains that are used to calculate *m'* are not necessarily the activated slip planes. One way around this is to use the Schmid factor to predict which slip system is active in each grain given a particular stress [17, 18]. Another factor that is not accounted for in *m'* is the orientation of the grain boundary plane [16].

The orientation of the grain boundary plane is taken into account by Shen et al. [19] using the parameter *M*:

$$M = (\mathbf{L}_1 \cdot \mathbf{L}_2)(\mathbf{g}_1 \cdot \mathbf{g}_2) \qquad (1.4)$$

where $\mathbf{L}_1$ and $\mathbf{L}_2$ are unit vectors along the intersection lines of the slip planes with the grain boundary plane and $\mathbf{g}_1$ and $\mathbf{g}_2$ are unit vectors along the slip directions. The parameters *M* and *m'* are illustrated in Figure 1.1 [20]. The angle between the intersection lines of the slip planes with the grain boundary plane is θ, the angle between the slip directions is κ, and the angle between the slip plane normals is Ψ. Experimentally, if the orientations of the grains is known, κ and Ψ are readily calculated, but unless the subsurface orientation of the boundary is known, θ cannot be calculated. Changing the rotation of the grain boundary plane with respect to the sample surface plane normal and/or changing the inclination of grain boundary plane will change the angle of θ. The rotation alignment of the grain boundary plane with respect to the crystal orientation of the two grains can easily be determined by imaging the sample surface to view the grain boundary. On the other hand, the inclination of the grain boundary plane cannot be as easily determined. One method involves using a focused ion beam (FIB) to make a cut across the grain boundary to view the inclination. This may not be desirable as it is destructive.

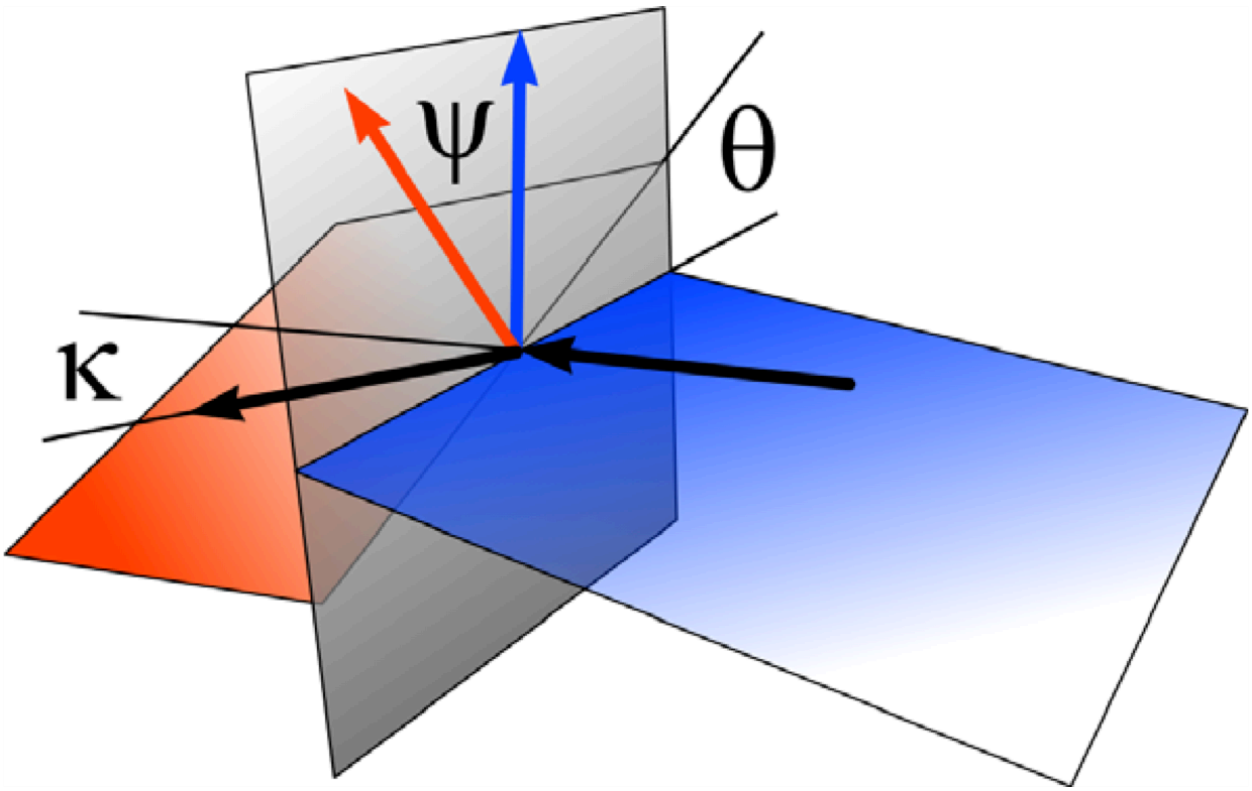

Figure 1.1: Illustration of both m' and M where the m' equation uses the angles Ψ and κ and M uses the angles θ and κ [20].

1.2 Deformation Mechanisms of bcc Metals

The accepted slip systems for bcc metals are composed of the ½<111> Burgers vectors with the {110} and {112} slip planes [21–23]. Some researchers also consider the {123} slip planes [23, 24]. The activity of the various slip planes is predominately determined by the temperature at which deformation occurs. As the temperature increases, so does the activity of different slip planes, beginning with the {110} being the most active at low temperatures followed by the {112} and then the {123} becoming more active at higher temperatures [23]. This allows for a total of 48 slip systems; 12 from {110} planes, 12 from {112}, and 24 from {123} plane.

Due to the nature of the screw dislocation, the fact that the Burgers vector and line direction are the same, they do not define a slip plane and are therefore non-planar. More specifically, in bcc metals, looking down the ½<111> dislocation line direction of a screw dislocation, there are three {110}, three {112}, and six {123} planes intersecting the dislocation core. Screw dislocations can readily cross-slip amongst these various planes, resulting in what is known as wavy slip [7, 23, 25, 26]. Wavy slip makes slip trace analysis in bcc metals difficult because the slip lines do not always line up with a predicted slip trace. On the other hand, if the wavy slip lines do line up with a predicted slip trace, it is possible that the slip system for that predicted trace was never activated, but the summation of other cross-slipping planes makes it appear that way.

As a result of this variable slip plane, unlike the crystal structures of fcc and hcp, bcc materials do not necessarily follow Schmid's law. The observation of non-Schmid behavior of bcc metals dates back to the time Schmid's law was developed. By way of tension and compression tests on single-crystals of iron and β-brass, Taylor [27] found that deformation slip

in one direction, is not the same as deformation slip in the opposite direction, known as asymmetry of slip [12, 27, 28].

Schmid's law only accounts for the calculated resolved shear stress on specific slip planes in directions of slip (known as Schmid's Stress), while other projections of the stress tensor are said to have no effect [12]. This does not seem to affect the ability to predict slip in fcc and hcp materials; but for bcc metals the other projections of the stress tensor do matter because of the screw dislocation core structure [3, 27, 28]. The effect of non-Schmid projections of the stress tensor has been demonstrated in atomistic studies of screw dislocations [3, 12, 29–31].

From atomistic studies [3, 12, 29–31], it was found that the relaxed screw dislocation core in Mo spreads onto the {110} planes, as shown in Figure 1.2. The dislocation core was relaxed using bond order potential [29]. Dislocations move in the direction their cores spread and depending on the stress applied to the dislocation, the core will favor spreading on some planes over others [29]. This is demonstrated from an atomistic simulation where a shear stress was applied perpendicular to the Burgers vector in both a positive and negative sense, shown in Figure 1.3a and Figure 1.3b, respectfully [12, 29]. The coordinate system used in this simulation had the *z*-axis aligned with the <111> direction and the *y*-axis perpendicular to the (-101) plane, where the stress tensor used is given by [29]:

$$\sum_{\tau} = \begin{bmatrix} -\tau & 0 & 0 \\ 0 & \tau & 0 \\ 0 & 0 & 0 \end{bmatrix} \quad (1.5)$$

The magnitude of τ is 0.05 the elastic modulus, C_{44}, which means the core spreading is purely elastic and reverts back when the stress is removed. When the shear stress is applied in the positive sense, the core spreads more on (-101), but when the shear stress is applied in the negative sense, the core spreads onto the (0-11) and (-110) planes. The screw dislocation core

spreading onto intersecting planes is the main reason for a high Peierls stress needed to activate crystal glide [12, 29]. In contrast, edge segments are not found to spread onto other planes, thus maintaining a planar configuration. Therefore, screw dislocations have lower mobility than edge dislocations causing the deformation of bcc materials to be governed, or limited, by the motion of screw dislocations [23].

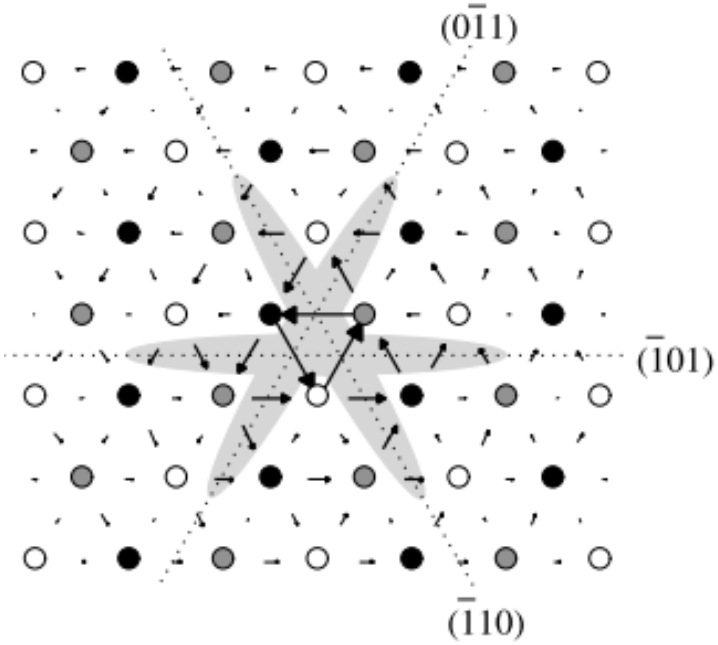

Figure 1.2: The relaxed ½<111> screw dislocation core of molybdenum. The different shades of circles represent consecutive (111) planes and the arrows representing the magnitude of out of plane atom displacements [29].

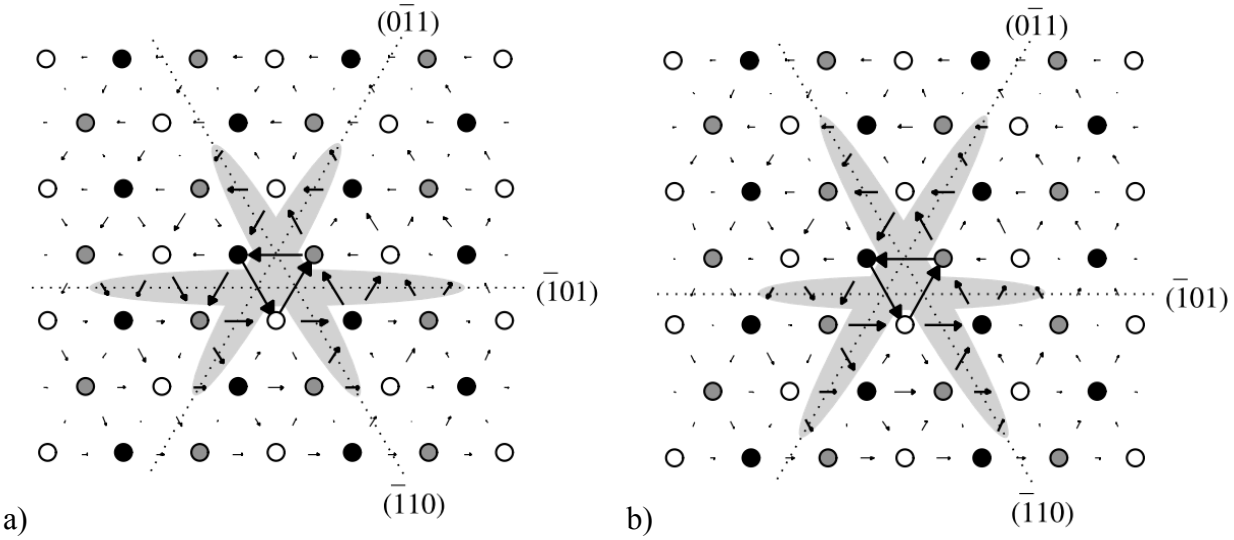

Figure 1.3: a) Structure of a screw dislocation core after an applied shear that is perpendicular to the Burgers vector in the positive sense and the b) negative sense [12].

2 Background of Analytical Techniques

This chapter gives a literature review of the analytical techniques used for this work. This includes nanoindentation, crystal plasticity finite element modeling of nanoindentations, electron backscattered diffraction (EBSD), cross-correlation EBSD (CC-EBSD), electron channeling contrast imaging (ECCI), and the collection of selected area channeling patterns (SACPs).

2.1 Nanoindentation

Nanoindentation is a technique that allows for probing a material's properties from specific locations, such as near or away from grain boundaries, to mimic single-crystal or bi-crystal experiments. Using nanoindentation, variables such as the state of stress and indentation methodology can be modified in order to obtain desired measurements. This is done by simply changing the indenter tip type and adjusting the mode the nanoindenter operates in. The versatility of nanoindentation makes it a great technique for understanding dislocation slip.

Numerous studies of single-crystal nanoindentation have been performed to understand slip in metals [32–36]. Biener et al. [33] did nanoindentation in single-crystal bcc Ta to understand dislocation nucleation. They found dislocation nucleation to occur as a pop-in event, also known as a displacement jump in a load-displacement curve, as shown in Figure 2.1. The displacement jump occurs after a buildup in the elastic strain energy, which has an initial curve that follows Hertzian contact theory [37], and is then released to begin plastic deformation. This pop-in event (from hereafter will be referred to as an initial pop-in, as there can be a secondary pop-in) occurs in most materials, yet varies in the displacement jump depth, and marks the point of incipient plasticity, or where plasticity begins [16, 33]. In Ta, this initial pop-in event occurs

at varying loads, but the loads at which they occur can be shifted by changing the loading rates [38].

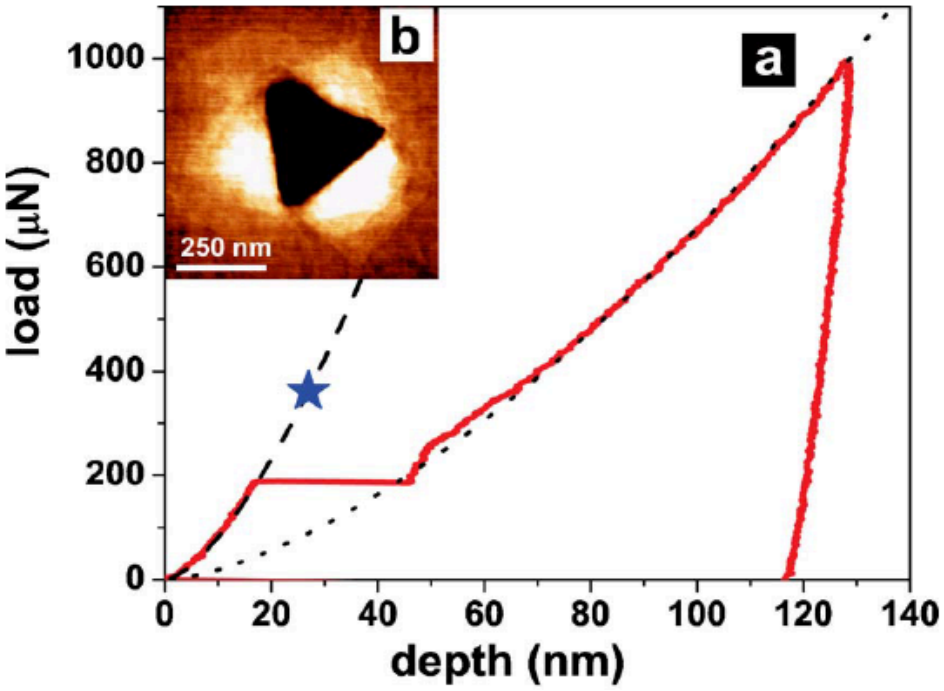

Figure 2.1: This load-displacement curve shows a displacement jump that marks the beginning of plasticity [33].

Wu et al. [36] studied the effect of tip radius on the stress at which an initial pop-in occurs in chromium (Cr). They found that as the tip radius decreases, the stress at which initial pop-ins occur increases. Figure 2.2 shows the experimental data compared to a homogenous dislocation nucleation model, shown as green line in Figure 2.2a, and to a model combining homogenous dislocation nucleation and the activation of pre-existing dislocations, shown as a red line in Figure 2.2b. For a large tip radius, there is a significant deviation from the homogenous dislocation model at low loads, indicating the activation of pre-existing dislocations. As to why this occurs with large tip radii, Wu et al. points out that as the stressed volume of material increases, the chances of activating pre-existing dislocations increases [36].

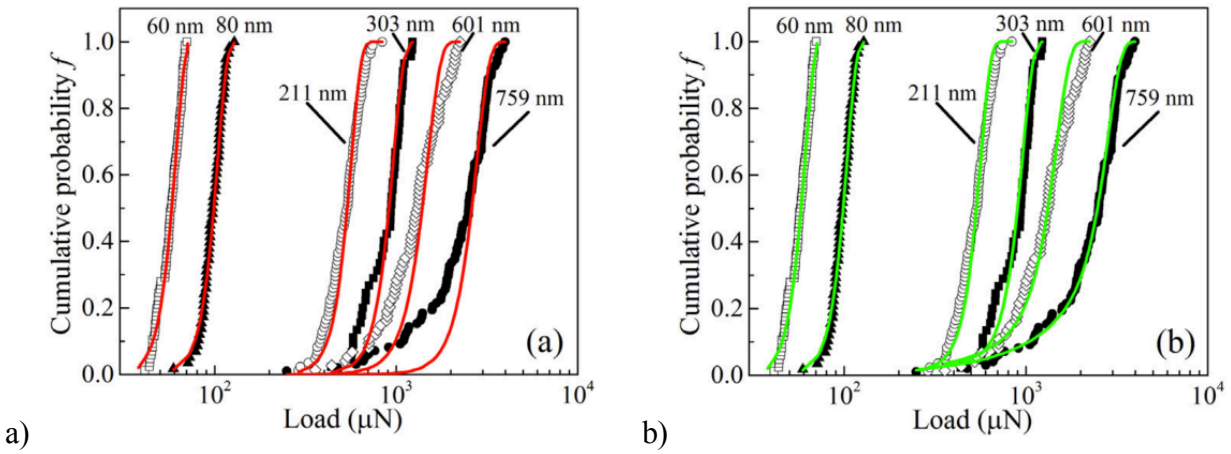

a) b)

Figure 2.2: Experimental data for the loads at which the initial pop-ins occur compared to a) an homogenous dislocation nucleation model and b) a combined model of homogenous dislocation nucleation and the activation of pre-existing dislocations.

Bi-crystal nanoindentation studies have been performed to understand slip transfer across grain boundaries [15, 16, 39–42]. These studies have cited a secondary pop-in phenomenon, as shown in Figure 2.3 [15, 16]. In addition to the previously discussed initial pop-in, a second pop-in can be observed that is associated with grain boundary slip transfer. While the first pop-in happens in almost all materials and marks the beginning of plasticity, the second pop-in only occurs for indents near grain boundaries. The proposed reason for this pop-in is a buildup of dislocations at the grain boundary, which causes the hardness (or the slope of the load-displacement curve) to be greater than in the bulk portion of the crystal. When the energy from the buildup in the dislocation pile-ups reaches a critical level, it causes dislocations to nucleate in the neighboring grain, resulting in strain relaxation and a pop-in event. After the pop-in, the hardness at the grain boundary is then comparable to the hardness of the bulk of the crystal [15, 16, 39–41]. An example of load-displacement curve of a secondary pop-in is shown for Fe-Si in Figure 2.3b [16].

a)

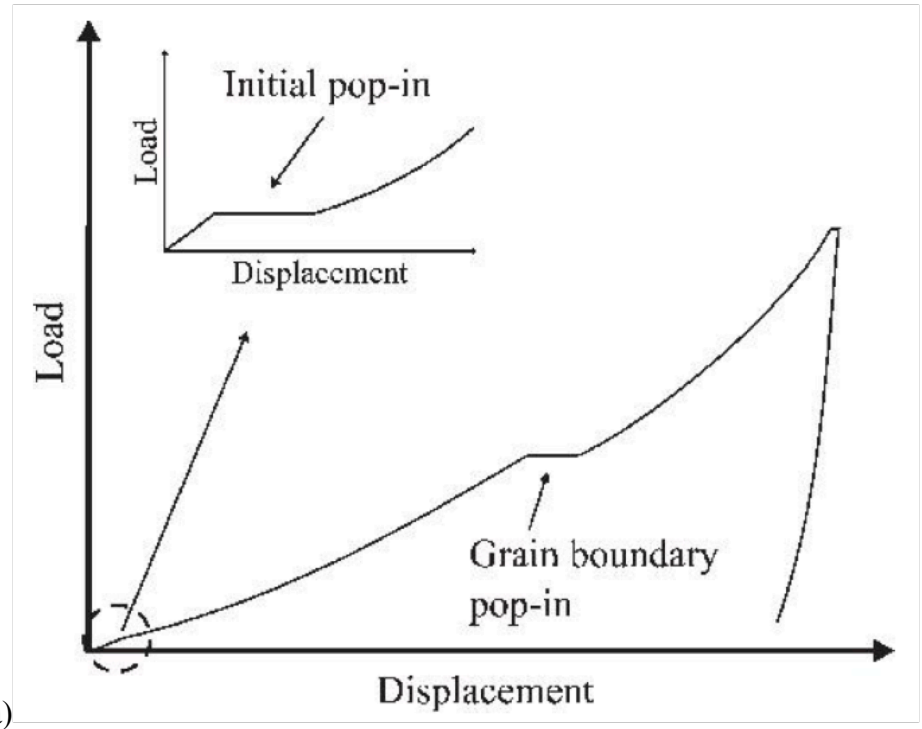

b)

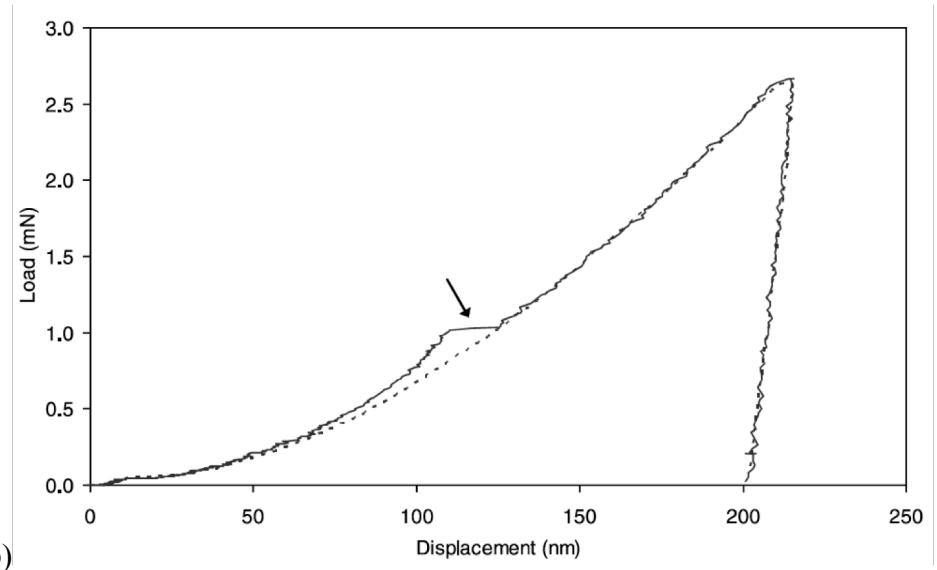

Figure 2.3: a) Illustration of a generic curve of pop-ins [15]. b) Curves showing a bulk sample indent in Fe-Si and an indent near a grain boundary that exhibits a secondary, or grain boundary, pop-in [16].

Secondary pop-ins do not always occur when an indent is made near a grain boundary. Studies [16, 40] have tried to use parameters such as *m'* and *M* to try to predict when or a reason why secondary pop-ins occur at some grain boundaries and not others. Wang and Ngan [40] showed there is a correlation between secondary pop-ins and the *m'* parameter in niobium. This is summarized in Table 2.1 [40]. It must be noted, however, that Wang and Ngan only used the *m'* parameter with relation to the closest slip planes and closest slip directions and made no approximation for what the activated slip planes and directions are.

On the other hand, Soer et al. [16] found *M* to be a better parameter than *m'* for predicting secondary pop-ins. For comparison, they used a molybdenum (Mo) bi-crystal that had a coincident site lattice (CSL) <111> tilt boundary. Using *m'* in relation to the closest planes and directions would give an *m'* value of 1 because of the perfectly aligned slip systems between the two grains [16]. For the values of *M*, Soer et al. assumed uniaxial compression in relation to faces of the Berkovich indenter tip and used the Schmid factor to approximate which slip system would have the maximum resolved shear stress. Their comparison for *m'* to *M* is summarized in Table 2.2 [16].

Table 2.1: Comparison of the occurrence of a pop-in event and *m'* in niobium [40].

Grain Boundary Number	CSL Σ	Ψ	κ	*m'*	Grain Boundary Pop-in
1		0.9970	0.9948	0.9918	Yes
2		0.9953	0.9913	0.9866	Yes
3		0.9946	0.9617	0.9665	Yes
4	41c	0.9953	0.9404	0.9360	Yes
5	41b	0.9976	0.8879	0.8858	No
6	9	0.9972	0.8858	0.8833	No
7	29b	0.9972	0.8339	0.8316	No
8		0.9966	0.8143	0.8115	No

Table 2.2: Comparison of *m'* and *M* [16].

Material	*m'*	*M*	Grain Boundary Yielding Observed
Mo	1.0 (Σ3)	0.78 (Σ3)	No
	0.99 (Σ11)	0.25 (Σ11)	No
Fe-Si	0.93	0.82	Yes, depending on indenter orientation
Nb	0.90 – 0.99	-	Yes, regardless of indenter orientation

There is a problem with the comparison made by Soer et al. between *m'* and *M* because they do not compare the parameters at all, but rather only changed what inputs go into the equations. They considered all slip systems for calculating *m'* and only the activated slip systems for calculating *M*. It is possible that *m'* could be as good as *M* at predicting pop-ins if the possible slip systems were determined for the *m'* parameter using the Schmid factor approximation as well. Therefore, it would be more thorough to use the same slip plane selection criteria when comparing *m'* and *M*.

Wang and Ngan [40] found a correlation between the load and the distance from the grain boundary the indent was made. This correlation is shown in Figure 2.4. Wang and Ngan further quantify this correlation with *c/d* ratios to describe pop-in occurrences. The variable *c* is the radius of the elasto-plastic boundary and *d* is the distance from the grain boundary the indent was made. The variable *c* is estimated with Eq. (1.14), which was developed by Zielinski et al. [34] from Johnson's model [43, 44]. P represents the load at which the pop-in occurred and σ_{ys} is the yield stress of the material.

$$c = \sqrt{\frac{3P}{2\pi\sigma_{ys}}} \quad (2.1)$$

The results from Wang and Ngan [40] show that pop-ins occur between c/d ratios of 1.5 and 5 but mostly around 2. They also found that the c/d ratio is the same for a given grain boundary segment.

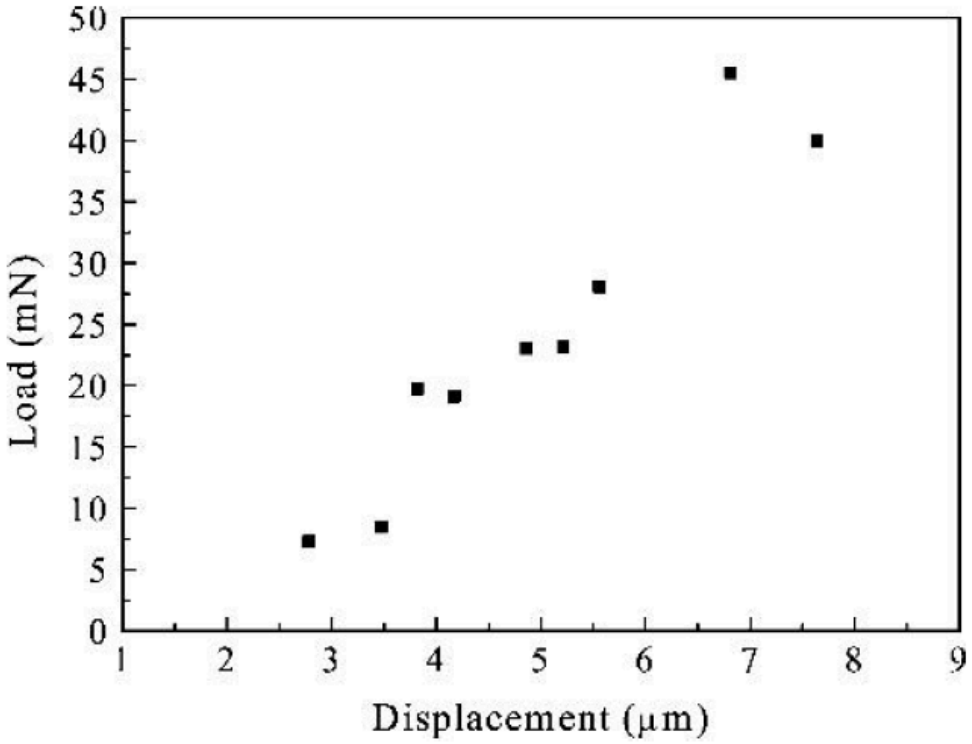

Figure 2.4: Load at which the pop-ins occurred versus distance from the indent to the grain boundary [40].

2.2 Crystal Plasticity Finite Element Method (CPFEM)

The finite element methodology (FEM) is a tool used to solve the non-linear differential equations of physical systems such as stress, strain, temperature gradients, fluid flow, etc. This can be done for a body that can have an overall complicated geometry by applying a mesh composed of many smaller bodies, called elements, which have a simple geometry (i.e. a square, rectangle, or triangle). Because FEM is only a solver, a material model must be constructed in order to use FEM for specific applications [45, 46].

The crystal plasticity finite element method (CPFEM) is a specific model used to simulate plastic deformation using FE methodology [46]. The CPFE method is built on the computational techniques of continuum mechanics and the knowledge gained from experimental results. Peirce et al. were the first to introduce the CPFE method in 1982 [47]. Since then, the developed constitutive models have been applied to a plethora of mechanical problems and used to simulate experimental conditions. This includes, but is not limited to, nanoindentation, tensile tests, grain boundary deformation, and texture evolution [32, 48, 49].

The kinematic equations for finite strain CPFEM are:

$$\mathbf{F} = \mathbf{F}_e\mathbf{F}_p \tag{2.2}$$

$$\mathbf{S} = \frac{1}{2}\,\mathbf{C}\left(\mathbf{F}_e{}^{T}\mathbf{F}_e - \mathrm{I}\right) \tag{2.3}$$

$$\dot{\mathbf{F}_p} = \mathbf{L}_p\mathbf{F}_p \tag{2.4}$$

$$\mathbf{L}_p = \sum \dot{\gamma^{\alpha}}\,\mathbf{m}^{\alpha}\otimes\mathbf{n}^{\alpha} \tag{2.5}$$

where $\mathbf{F}$ is the deformation gradient that is composed of both an elastic, $\mathbf{F}_e$, and plastic, $\mathbf{F}_p$, components. The stress, $\mathbf{S}$, is a function of the 4th order elastic tensor, $\mathbf{C}$, and $\mathbf{F}_e$. The plastic deformation evolves as a function of the sum of the shear rates on all possible slip systems, $\mathbf{L}_p$,

which is determined by the shear rate, $\dot{\gamma}$, the slip direction, **m**, and the slip plane, **n**, of slip systems

$\alpha = 1,\ldots, N$.

There are many constitutive models that can be used depending on the specifics of what is being modeled, but this work will primarily focus on the phenomenological constitutive model, first introduced by Peirce et al. [47]:

$$\tau^{\alpha} = \mathbf{S} \cdot (\mathbf{m}^{\alpha} \otimes \mathbf{n}^{\alpha}) \qquad (2.6)$$

$$\dot{\gamma^{\alpha}} = \dot{\gamma_0} \left| \frac{\tau^{\alpha}}{\tau_c^{\alpha}} \right|^{\frac{1}{m}} \operatorname{sgn}(\tau^{\alpha}) \qquad (2.7)$$

$$\dot{\tau_c^{\alpha}} = h_{\alpha\beta} \left| \dot{\gamma^{\beta}} \right| \qquad (2.8)$$

$$h_{\alpha\beta} = q_{\alpha\beta} \left[h_0 \left(1 - \frac{\tau_c^{\beta}}{\tau_s} \right) \right]^{a} \qquad (2.9)$$

In these equations, τ is the resolved shear stress with τ_c being the critical resolved shear stress and τ_s is its saturation value. $\dot{\gamma_0}$ and m are material parameters of the reference shear rate and rate sensitivity of slip, respectively. The hardening matrix, $h_{\alpha\beta}$, gives the effect any slip system β has on the hardening behavior of slip system α. $q_{\alpha\beta}$ represents latent hardening with h_0, a, and τ_s being the structure evolution parameters [46, 47].

With the different constitutive models, there needs to be a material implementation code in order to simulate crystallographic deformation. Researchers at Max-Planck-Institut für Eisenforschung GmbH (MPIE) have developed a few of these framework codes. One in particular is the Düsseldorf Advanced Material Simulation Kit (DAMASK) [50]. This code is able to account for non-Schmid effects following the constitutive equation proposed by Koester et al. [51].

The equation for non-Schmid effects proposed by Koester et al. [51] is an extended version of the flow rule developed by Gröger et al. [29, 30, 52] from atomistic studies. The flow rule takes into account the non-glide projections of the stress tensor [51]:

$$\begin{aligned}\tau^{\alpha} = {} & \boldsymbol{\sigma}:\mathbf{m}^{\boldsymbol{\alpha}}\otimes\mathbf{n}^{\alpha} + a_1\boldsymbol{\sigma}:\mathbf{m}^{\boldsymbol{\alpha}}\otimes\mathbf{n}^{\alpha} + a_2\boldsymbol{\sigma}:(\mathbf{n}^{\alpha}\times\mathbf{m}^{\boldsymbol{\alpha}})\otimes\mathbf{n}^{\alpha} \\ & + a_3\boldsymbol{\sigma}:(\mathbf{n}_{\mathbf{1}}^{\boldsymbol{\alpha}}\times\mathbf{m}^{\boldsymbol{\alpha}})\otimes\mathbf{n}_{\mathbf{1}}^{\boldsymbol{\alpha}} + a_4\boldsymbol{\sigma}:\mathbf{n}^{\alpha}\otimes\mathbf{n}^{\alpha} \\ & + a_5\boldsymbol{\sigma}:(\mathbf{n}^{\alpha}\times\mathbf{m}^{\boldsymbol{\alpha}})\otimes(\mathbf{n}^{\alpha}\times\mathbf{m}^{\boldsymbol{\alpha}}) \\ & + a_6\boldsymbol{\sigma}:\mathbf{m}^{\boldsymbol{\alpha}}\otimes\mathbf{m}^{\boldsymbol{\alpha}}\end{aligned} \qquad (2.10)$$

In this equation, α represents the possible slip systems and $\boldsymbol{\sigma}$ is the stress tenor. $\mathbf{n}_{\mathbf{1}}^{\boldsymbol{\alpha}}$ includes an angle of -60° with reference to $\mathbf{n}_{\alpha}$. a_1 through a_6 represent specific material constants that can be fitted using atomistic studies. The first term of the equation is Schmid's law, the second term accounts for the slip asymmetry, and the third and fourth terms account for the shear stresses that are perpendicular to the slip directions. The fifth term takes into account the load in the Σ_{11} direction and the sixth term takes into account the load in the Σ_{22} direction. The last term was added to make the equation independent of hydrostatic stresses [51].

2.2.1 CPFEM of Nanoindentation

Zambaldi et al. [32] carried out single-crystal nanoindentations in hexagonal α-titanium and measured the subsequent topography by AFM mapping. They also coupled these experimental indents with CPFEM and performed a non-linear optimization to determine the crystal plasticity structure evolution parameters. In general, each optimization process compares resulting CPFEM topographies to experimental topographies, generates a new set of structure evolution parameters based off the comparison of results, and re-runs the process until the parameters are optimized to give the best CPFEM to experimental match. This process was carried out for a group of indentations with different crystal orientations. Figure 2.5 shows two

portions of the hexagonal stereographic projection with indent topographies placed on the projections to represent the different orientations indented. Figure 2.5a shows experimental indents and Figure 2.5b shows simulated indents following the optimization of the structure evolution parameters. The projections show a good match between the experimental and simulated indents and both projections illustrate that topography evolution is a function of grain orientation [32].

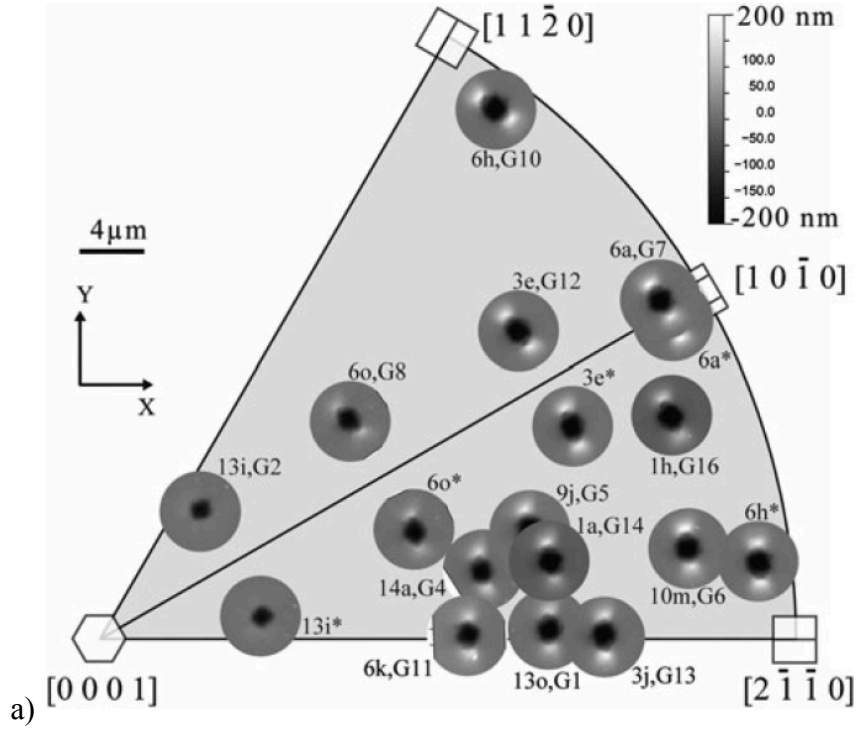

a)

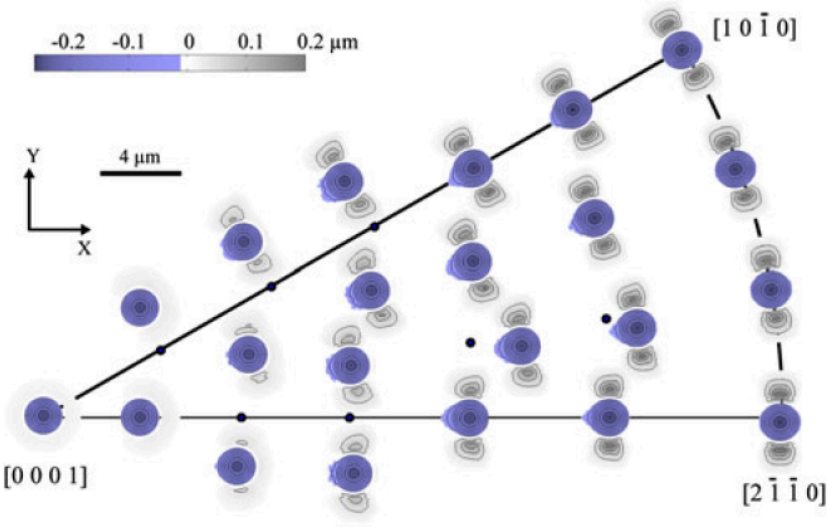

b)

Figure 2.5: Illustration of a) experimental and b) simulated topography evolution as a function of grain orientation [32].

2.2.2 CPFEM Construction for Nanoindentation

Single crystal and bi-crystal simulations of nanoindents can be easily set up using the Matlab [53] toolbox STABiX [54, 55]. This toolbox uses graphical user interfaces (GUIs) to allow for the easy inclusion of experimental conditions, such as crystal type (fcc, bcc, or hcp), slip systems, crystal orientation, indentation tip type and size, and indentation depth. For bi-crystal indents, the GUIs also allow for the inclusion grain boundary inclination and the distance from the indenter tip to the grain boundary. Users can tailor the size/number of elements used to build the finite element mesh depending on their specific needs. Once the needed experimental conditions are incorporated using GUIs and the mesh size decided, a Python [56] file is exported in order to build the mesh in Marc [57] or Abaqus [58], depending to the finite element solver that is used.

STABiX is not only used for setting up nanoindentation simulations, but also helps to characterize grain boundaries. One of the GUIs allows for EBSD data to be imported and then calculates the *m'* based off the alignment of the slip system plane normals and Burgers vectors. The GUI shows all grain boundaries colored based off their m' value to assess the grain boundaries relative susceptibility to deformation. Not only can this be done for *m'*, but also for other parameters such as misorientation across the grain boundary.

2.3 Electron Backscattered Diffraction

When a focused beam of electrons hit the surface of a material, there are a number of scattering events that can occur in all directions [59, 60]. Some electrons are backscattered within the sample and as they exit the sample they are diffracted by the lattice planes at the Bragg angle. As this occurs in all directions, the diffracting lattice planes form Kossel-cones. One set of lattice planes produces two cones. By placing a phosphor screen near the sample, the

Kossel-cones appear as lines , known as Kikuchi lines, that are generally parallel to each other. They are only generally parallel as the lines are actually hyperbolas that are parallel in the center on the phosphor but bend away from each other at the edges of the phosphor screen. This is due to the fact that the outer edge of the phosphor is further from the source of diffraction than the middle.

An example of this is shown for one set of lattice planes in Figure 2.6 [60]. As more than one set of crystallographic planes will form Kossel-cones at once, multiple sets of Kikuchi lines will appear on the phosphor screen, forming a complete electron backscattered diffraction pattern (EBSP), also known as an EBSD pattern [59–61]. To maximize the yield of electrons that make it to the phosphor screen/EBSD detector, samples are generally tilted to ~70° [59, 60, 62].

From these EBSD patterns, the orientation of the crystal can be determined. Currently, the process of determining the orientation of crystal in automated using the Hough transform [59, 60, 63]. The Hough transform essentially detects the Kikuchi bands of the EBSD pattern and indexes the pattern to related crystal orientation. Early use of the Hough transform for band detection started around 1992 and required ~2 s of computer time to index one pattern [59]. The current rates of pattern indexing are well over 1000 points per second [64, 65]. The rate of indexing is primarily affected by EBSD camera sensitivity and the computer processing time for indexing [66]. While the primary use of EBSD is measuring crystal orientation, the technique can used to measure many more things than that. A few examples include: grain size, texture, lattice misorientation, grain boundary disorientation, and even combined with energy dispersive spectroscopy (EDS) for phase identification.

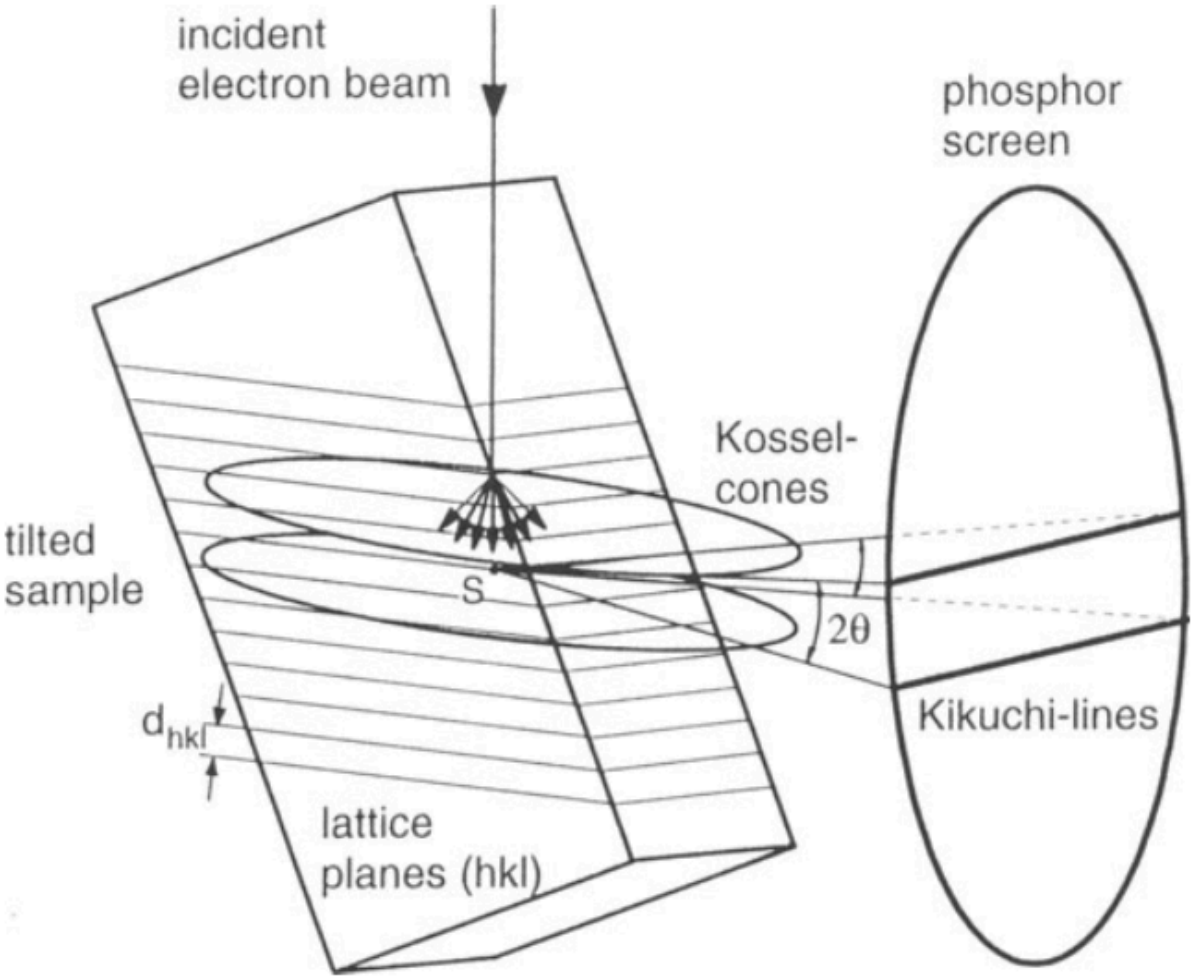

Figure 2.6: A pictorial example of Kossel-cones formed from backscattered electrons being diffracted at the Bragg angle by lattice planes as they exit the crystal. These Kossel-cones project as lines on the phosphor screen [60].

Users of EBSD need to be concerned with spatial and angular resolution. Spatial resolution of EBSD is related to the interaction volume of the beam. Due to how EBSD is set up, the electron beam hits the surface as an ellipse with the long portion in the direction of the sample tilt. Beyond this, the interaction volume of the beam is a function of the material, accelerating voltage, the beam current, and the type of filament used [67]. Spatial resolution can be between 30 nm and 60 nm [60, 67, 68].

Angular resolution is the ability at which EBSD can determine the relative differences in the orientations of neighboring data points [67]. The angular resolution can be impacted by a number of factors, including, speed at which EBSD is carried out, the binning of EBSD patterns, and the accuracy of the pattern center calibration for EBSD [60, 63, 66, 67]. The angular resolutions of EBSD is in the range of 0.5° and 2.0° [60, 63, 67]. This diminishes the ability of EBSD accurately determine elastic strains and GNDs.

2.4 Characterization and Mapping of Dislocations

Traditionally, dislocation structures have been characterized using transmission electron microscopy (TEM) [69, 70]; however, TEM is plagued by a number of limitations associated with the requisite thin foils. These can include difficult sample preparation, the potential for this sample preparation to affect the apparent dislocation distributions, and limited observation volumes can lead to poor statistical representation of the bulk.

Two significantly different techniques, electron channeling contrast imaging (ECCI) [71–76] and cross-correlation electron backscattered diffraction (CC-EBSD) [77–80], are alternative scanning electron microscopy (SEM) based approaches for characterizing dislocation structures. Both of these techniques involve the examination of the near surface region of bulk samples and require careful preparation of this surface region to be examined; nevertheless, this

approach eliminates many of the limitations imposed by TEM thin foils. Surface preparation may be carried out either before or after the imposed deformation.

2.4.1 Selected Area Channeling Patterns (Obtaining Imaging Conditions for ECCI)

In many respects, ECCI is carried out in the same manner as diffraction contrast TEM; that is, imaging is achieved by setting up specific diffraction/channeling conditions. Instead of using electron diffraction patterns to establish "2-beam" conditions as with TEM, ECCI relies on either EBSD patterns, electron channeling patterns (ECPs), or selected area channeling patterns (SACPs) to establish electron channeling conditions [68, 72, 76].

EBSD is advantageous to use for setting up ECCI imaging conditions because it can quickly obtain crystal orientations with a high spatial resolution of ~30 nm (spatial resolution is dependent on the specific beam conditions) [60, 68, 81]. On the other hand, the accuracy of EBSD is limited to 0.5-2.0° [63, 67, 81]. Due to this, it can be difficult to know the exact imaging condition, i.e. the **g** vector, used to image dislocations. Therefore, ECCI studies that are set up using EBSD patterns are more qualitative and less quantitative in terms of characterizing dislocations.

ECPs are better than EBSD patterns in that they give a clear understanding of the specific imaging conditions. ECPs can give an absolute accuracy in crystal orientation of less than 1° [72]. An ECP is formed when a single crystal (or large grain from a polycrystal) is viewed at low magnification. If the magnification is low enough, the beam will have a large enough scan angle to view the diffraction contrast of backscattered electrons resulting from the crystal planes being at the Bragg angle relative to the sweeping beam. This contrast makes up the channeling pattern [72]. The utilization of ECPs are limited by that fact it has a spatial resolution of ~1 mm

[68] and therefore they cannot be achieved for polycrystalline samples with small to moderate grain sizes.

SACPs overcome the limitations of ECPs because rather than the beam sweeping over the crystal, the beam is rocked on a "single point" on the crystal surface to achieve the same effect. Single point is written in quotes due to the fact it is a point with an associated area. The user manual for the Tescan Mira 3 field emission gun scanning electron microscope (FEG-SEM) used in this work suggests grains should have a minimum grain size of 100-150 μm to achieve SACPs. An example of a SACP obtained using the Tescan Mira 3 FEG-SEM is shown in Figure 2.7, with the square marking in the center of the SACP, which is the optic axis of the electron beam. The maximum angular range of this SACP is approximately 20°. It is seen that long the outer edge of the SACP the main channeling pattern is not continuous. This is because the outside portion of the channeling pattern is formed from the channeling effects of neighboring grains. As the grain size from which an SACP is obtained gets smaller, the observed channeling of neighboring grains is increased and channeling pattern of the grain of interest gets smaller. This demonstrates that spatial resolution goes down as the angular range goes up [68].

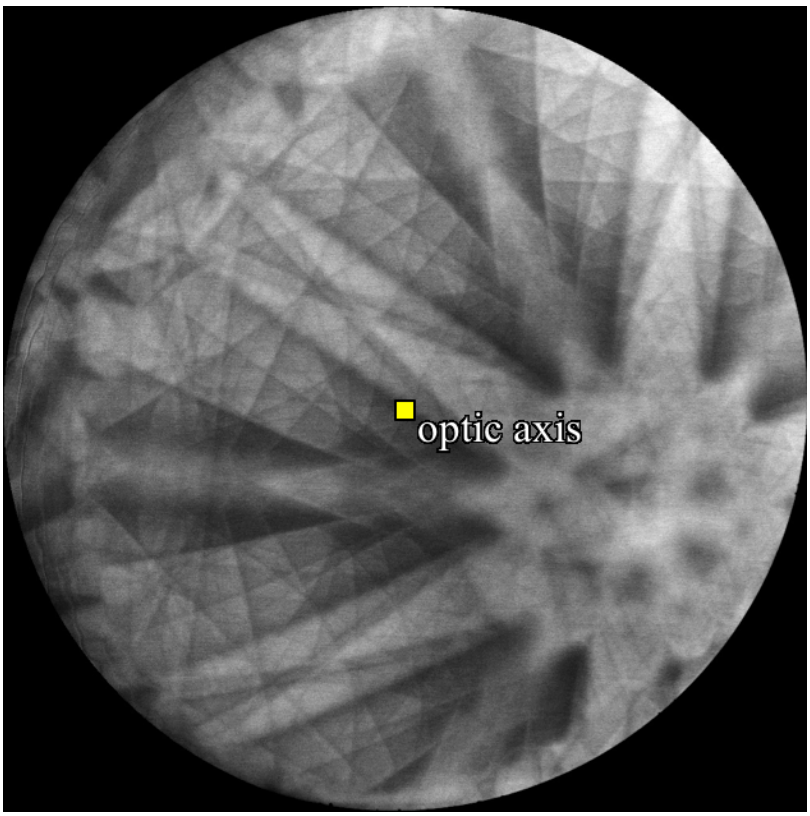

Figure 2.7: SACP obtained using a Tescan Mira 3 FEG-SEM.

In this work, SACPs were successfully obtained from grain sizes around 40 μm in diameter. There were, however, significant effects from neighboring grains along the outer edge of the channeling pattern image, leading to a limited view of the channeling pattern of interest. This limited view becomes worse with higher tilts as the projection of the grain becomes smaller. Due to the limited spatial resolution of the Tescan Mira 3 FEG-SEM, dislocations cannot be characterized in small grains.

Guyon et al. [68] were able to obtain SACPs with a spatial resolution of 500 nm and a rocking beam angle of 4.2° using a Crossbeam FEG-SEM Zeiss Auriga equipped with a Gemini column. This was done by calibrating the beam shifts in order to accurately adjust the rocking beam position. This allows for SACPs to be obtained from samples with small grain sizes.

2.4.2 Electron Channeling Contrast Imaging

In order to view dislocations using ECCI, it is necessary to understand how the channeling conditions relate to electron interactions within the crystal. Depending on the angle at which an electron beam hits a crystal, there can be either high backscattered electron yield, large η, or a small backscattered electron yield, small η [72]. A pictorial example of this is shown in Figure 2.8a. Artificial SACPs for high backscattered electron yield and low backscattered electron yield are shown in Figure 2.8b and Figure 2.8c, respectfully. The black dot in the SACPs shows the optic/beam axis that corresponds to the two SACPs for the different amounts of backscattered electron yield.

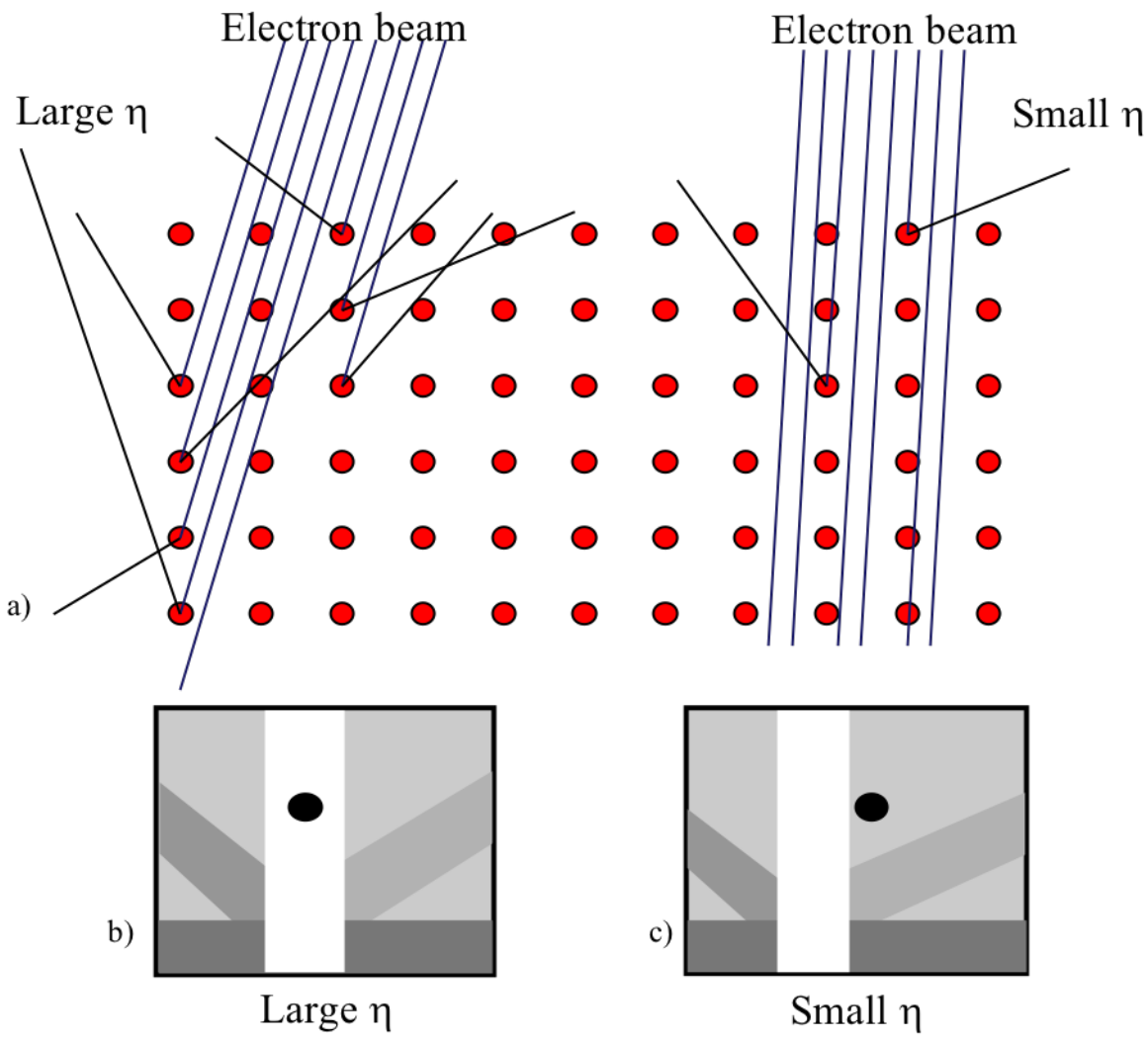

Figure 2.8: a)Pictorial representation of the backscattered electron yield with respect to the angle at which electrons hit a crystal. b) An imitation SACP corresponding to a condition of high backscattered electron yield, large η. c) An imitation SACP corresponding to a condition of low backscattered electron yield, small η. The black dots in b) and c) represent the optic axis of the electron beam (amended from Crimp [74] and Joy et al. [72]).

A crystal sample is rotated/tilted so that the optic axis in on the edge of a channeling band, shown in Figure 2.9c. At this point the electron beam is hitting the bulk of the crystal at the Bragg angle, θ_B, for the crystal planes associated with that channeling band. As the rastering electron beam passes over a dislocation, shown in Figure 2.9a, one side of the dislocation distorts the lattice so the electron beam is interacting with the crystal at angle α, which is larger than the Bragg angle. This locally distorts the channeling condition so the optic axis is now off the channeling band, shown in Figure 2.9d. The other side of the dislocation will distort the lattice in the opposite way so that the electron beam is interacting with the crystal at angle ω, which is smaller than the Bragg angle. This locally distorts the channeling condition so the optic axis is now on the channeling band, shown in Figure 2.9b. These distortions cause one side of the dislocation to be dark and the other side to be bright. Tilting/rotating the sample so the that the opposite **g** vector is used (the other side of the same channeling band) will cause the bright and dark sides of the dislocation to switch.

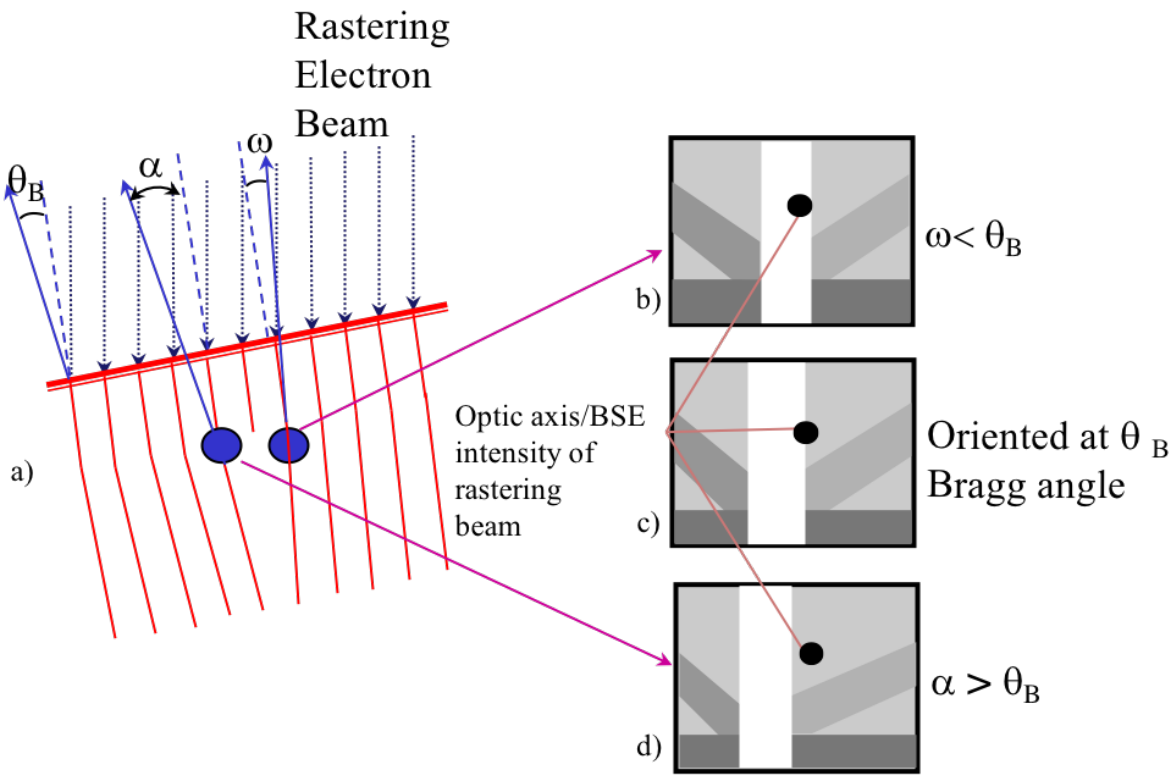

Figure 2.9: a) Pictorial representation of the rastering electron beam (dotted blue lines) moving over a dislocation. A pictorial representation of the channeling condition for the bulk of the crystal lattice is shown in c) where the optic axis of the electron beam is hitting the crystal planes at the Bragg angle. The lattice distortions from the dislocation change the local channeling condition so that the optic axis hits the crystal planes at angle ω (smaller than the Bragg angle) on one side and at angle α (larger than the Bragg angle) on the other side. The channeling conditions for these lattice distortions are shown in b) and d) (figure courtesy Dr. Martin A. Crimp).

Knowledge of the channeling conditions allows dislocations to be characterized in terms of their Burgers vectors, **b**, and line directions, **u**, using the well established $\mathbf{g} \bullet \mathbf{b} = 0$ and $\mathbf{g} \bullet \mathbf{b} \times \mathbf{u} = 0$ invisibility criterion, where **g** describes the channeling condition [71–73, 82]. In this respect, characterization of dislocations using ECCI is just like characterizing dislocations using TEM. The dislocation line widths resolved by ECCI are similar to that offered by diffraction contrast bright field imaging TEM, in the range of 10 to 12 nm [76]; however, TEM has the advantage of weak beam microscopy, which decreases the dislocation line width, allowing TEM to image areas with high dislocation densities [83, 84]. Conversely, ECCI has the advantage of necessitating only one free surface, so that image force [7] effects will not be as severe as in TEM thin foils. Also due to the one free surface with ECCI, a sense of the dislocation line inclination can be easily determined while determining this with TEM is more difficult.

2.4.3 Cross-Correlation Electron Backscattered Diffraction

One of the biggest limitations of EBSD is its angular resolution, which has a range of 0.5°-2.0° [60, 63, 67]. Cross-correlation electron backscattered diffraction (CC-EBSD), also referred to as high resolution or high angular resolution EBSD [77, 78, 85, 86], is able to obtain an angular resolution of 2×10^{-4} rad, which corresponds to 0.01° [77].

The cross-correlation method selects regions of interest (ROIs) within a given EBSD pattern and uses computer software to cross-correlate the ROIs across all EBSD patterns in order to detect the subtle shifts in the EBSD patterns. From this, the entire elastic strain tensor can be determined [77, 78]. The acquisition of EBSD patterns for CC-EBSD analysis is the same as traditional EBSD, however, longer exposure times are used to ensure adequate pattern quality and the patterns are saved for cross-correlation analysis to be performed offline. Due to the

longer exposure times and the offline analysis, CC-EBSD is significantly slower than traditional EBSD.

CC-EBSD can be used to map the GND content deduced from the Nye tensor [87]:

$$\alpha_{ij} = \sum_m \rho^{(m)} \boldsymbol{b}_i^{(m)} \boldsymbol{v}_j^{(m)} \qquad (2.11)$$

where *m* indicates the specific dislocation system (in this case, dislocation system is defined as combinations of the Burgers vectors and line directions for pure edge and screw dislocations), $\boldsymbol{b}$ is the Burgers vector, and $\boldsymbol{v}$ is the dislocation line direction [80]. These components of the Nye tensor come from elastic distortion gradients, determined from subtle shifts in the EBSD patterns between neighboring pixels in an EBSD map [77, 80]. CC-EBSD does not obtain all the components of the Nye the tensor, but Ruggles et al. [80] showed that it can be approximated in order to extract GND densities. Furthermore, Ruggles et al. [88] later showed that the GND density can be resolved onto the specific dislocation systems.

2.4.4 Previous Comparisons Between ECCI and CC-EBSD GND Mapping

To fully exploit the ECCI and CC-EBSD approaches, it is important to establish the limitations and relative capabilities of these techniques. A number of papers have shown how ECCI and CC-EBSD can be used in compliment of each other for a better analysis of dislocation structures [79, 89, 90]. Vilalta-Clemente et al. [90] used CC-EBSD to characterize relatively low density threading dislocations in as-grown InAlN epitaxial thin films, determining the individual densities for pure edge, pure screw, and mixed threading dislocations using supplemental information from ECCI; however, CC-EBSD and ECCI were carried out in different areas of the same sample. This work also indicated that the sign of individual dislocations could be assessed by CC-EBSD.

One of the objectives of the present study is to directly compare dislocation structures characterized by ECCI and CC-EBSD in the same area. These observations have been carried out by examining the dislocation fields developed around nanoindentations in bcc Ta. Of particular interest is the comparison between the information available from CC-EBSD and ECCI and the establishment of CC-EBSD as a viable technique for the rapid determination of GND densities, including its ability to characterize the specific slip systems involved in deformation.

3 Experimental Methods

3.1 Sample Preparation

Commercially pure polycrystalline Ta was provided by Sandia National Lab. From the bulk specimen, samples were cut to the size of approximately 5 mm x 4 mm x 32 mm using electric discharge machining (EDM). Samples were mounted in a 1 inch KonductoMet mount using a Prontopress-2 mounting press. Samples were prepared by grinding through 320, 500, 800, 1200, 2000, and 4000 grit silicon carbide (SiC). A final polish was achieved using a 4 to 1 mixture of Struers OP-S and aqueous 30% H_2O_2 on a Struers MD-Chem polishing cloth. Samples were examined optically and then using an scanning electron microscope (SEM) to confirm there was no residual deformation from the grinding and polishing. EBSD mapping of the polished samples was carried out using a Tescan Mira 3 field emission gun scanning electron microscope (FEG-SEM) and an EDAX Hikari EBSD camera with a 480 x 480 pixel resolution and Orientation Imaging Microscopy software (OIM^{TM}). This was carried out using an accelerating voltage of 20 kV, an instrument spot size of 49.0 nm, and specimen current of 1.9 nA. EBSD mapping was primarily done to identify locations to place indents.

To visualize the effect crystal symmetry has on indentation topography, as well the effect of indentation size, microindentation and nanoindentation were carried out. Microindentation was completed at the Max-Planck-Institut für Eisenforschung GmbH (MPIE). Nanoindentation was done at Michigan State University using an MTS Nano Indenter. Both microindentation and nanoindentation were carried out with a spherical conical indenter tip that had a tip radius of 1μm. Initial microindentation and nanoindentation arrays were made on the samples followed by EBSD mapping again. Due to the fact that the grain boundaries of the sample cannot be seen in the optical microscope used by the indenter, EBSD mapping was carried out in order to locate

the grain boundaries with respect to the initial indentation arrays. This allowed for more indentations to be selectively placed in specific grains and/or at specific grain boundaries.

3.2 Single Crystal Microindentation

An initial 10 x 20 microindentation array was made with a spacing of 200 μm between each indent. Indentation was carried out to a maximum load of 200 mN with a 20 s loading period followed by a 20 s unloading period. Following EBSD of the initial array, more indents were placed in the middle of large grains (about 150 μm) so the indents effectively induced single crystal deformation. In order to observe all deformation morphologies that can occur with the same load and strain rate, grains of various orientations were indented. The indent topographies were mapped using confocal microscopy at the Max-Planck-Institut für Eisenforschung GmbH (MPIE) to understand indent topography as a function of grain orientation. The topography results were processed using the Gwyddion [91] software. In order to accurately compare topographies to each other, measurements must be observed with each indent having a level plane with the same initial height. This was done by fitting a plane using three points that are away from the topography that was created from indentation and setting the height of that plane to zero.

3.3 Single Crystal Nanoindentation

An initial 10 x 20 nanoindentation array was made with a spacing of 40 μm between each indent. Each indent was carried out to a maximum load of 4 mN with a 10 s load, 10 s hold, and 10 s unloading cycle. Indents were selectively placed in the middle of grains with orientations near [001], [101], and [111]. The resulting topographies were mapped using Scanning Probe Microscope-Dimension 3100 SPM in tapping AFM mode. The AFM measured topographies were processed using Gwyddion as stated above.

3.3.1 CPFEM of Single Crystal Nanoindenation

Simulation of the corresponding [001], [101], and [111] indents were carried out using CPFEM. The framework for these simulations was built using the previously mentioned STABIX [54, 55]. The experimental variables included in the simulations were grain orientation, indenter tip radius, and indentation depth, along with the material properties of Ta, outlined below. Grain orientation was obtained from EBSD analysis and the indentation depth was obtained load/displacement data.

Only slip on {110} and {112} planes was taken into account in the simulations. The elastic constants used were: C_{11} = 261 GPa, C_{12} = 157 GPa, and C_{44} = 82 GPa [92]. The initial slip resistance, τ_0, and saturated slip resistance, τ_s, used for both {110} and {112} slip systems was 20 MPa and 400 MPa, respectively. The values used for the material hardening parameters, h_0 and a, were 75 MPa and 1, respectively. The reference shear rate, $\dot{\gamma}_0$, was set to 10^{-3} s^{-1} and the material parameter, m, was set to 1/20. The $q_{\alpha\beta}$ is 1 if the Burgers vector of slip system β is coplanar with slip system α and 1.4 if it is not.

The finite element solver used for the simulations was Marc. The results were exported as a Visualization Toolkit (VTK) file and analyzed using ParaView [93].

The simulated topographies were compared to the AFM mapped topographies. All simulations in this work were run without the implementation of the non-Schmid effects. It was attempted to use the non-Schmid components of DAMASK but the simulations would not converge after the first few increments.

3.4 Bi-crystal/Grain Boundary Nanoindentation

Based off of the same initial array used for the single crystal nanoindents, indents were selectively made near several grain boundaries. This was done in part as an effort to observe the

secondary pop-in that only occurs at grain boundaries, as shown in the previously mentioned literature [15, 16, 39–41].

Of the grain boundaries that were targeted for nanoindentation, three grain boundaries were selected for analysis. These three were chosen because they had a nanoindent placed on either side of the grain boundary, resulting in six grain boundary nanoindents. Bi-crystal nanoindentation topographies were mapped using AFM to see where indentation topography transfers across the individual grain boundaries.

Single crystal indents were also made in the middle of grains on either side of the three grain boundaries and their topographies mapped using AFM. Single crystal topographies were compared to grain boundary topographies in order to visualize the effect grain boundaries have on indentation topography.

3.4.1 CPFEM of Grain Boundary Nanoindentation

CPFEM simulations were done for all six grain boundary nanoindents. The experimental conditions were incorporated into the simulations using STABIX. Along with the experimental conditions included in the single crystal simulations, the experimental conditions of indentation distance from the grain boundary, grain boundary inclination, and the grain orientation for the neighboring grain were included in the simulations. The indentation distances from the grain boundaries were measured from BSE images. Grain boundary inclinations were determined from cross-section cuts made on grain boundaries using a Carl Zeiss Auriga Dual Column focused ion beam scanning electron microscope (FIB-SEM) and measured from BSE images. As an example of the inclusion of these experimental conditions in the simulation, a snapshot of mesh generation GUI of STABIX is shown in Figure 3.1a and an example of a FIB cross-section

on a grain boundary is shown in Figure 3.1b. CPFEM simulated grain boundary topographies were compared to experimental grain boundary topographies.

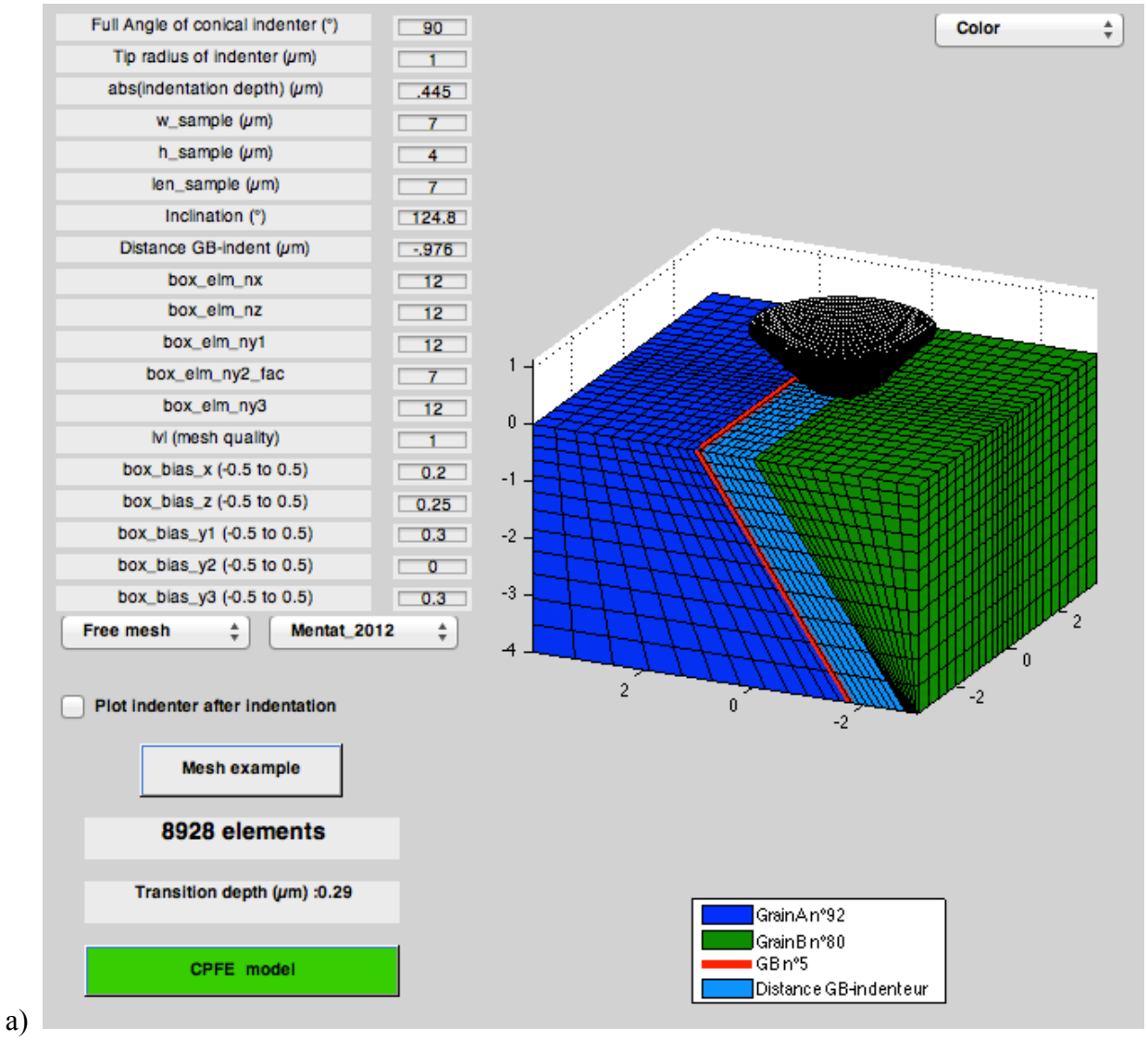

a)

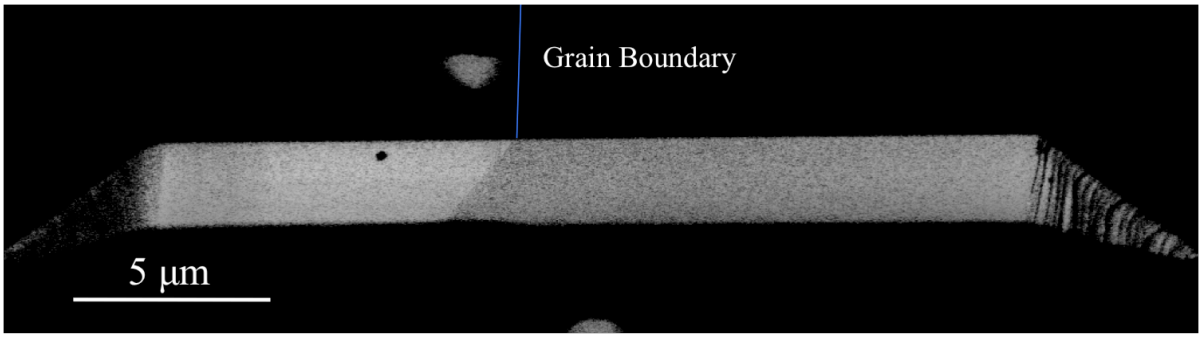

b)

Figure 3.1: a) A snapshot of the mesh generation GUI in STABIX and b) and example of a FIB cross-section on a grain boundary.

3.4.2 AFM Topography Subtractions

Comparisons between indent topographies were made using a method of topography subtraction described by Su et al. [42]. The height of each grid point in one AFM map is subtracted from a corresponding grid point in another AFM map. The first comparison was experimental grain boundary indents vs. experimental single crystal indents, in order to view how the presence of a grain boundary affects topography. An example of this subtraction is shown in Figure 3.2. The grain boundary indent is subtracted by the single crystal indents from both parent grain (grain that the grain boundary indent was made in) and the receiving grain (grain that receives deformation after it crosses the grain boundary). Only the portions of each single crystal indent that line up with the grain boundary indent were used in the subtraction. The unused portions of the single crystal indents are covered by a dark overlay in Figure 3.2. The center indent region of each subtraction was masked with a topography height of zero in order to focus the attention on the relevant topography around the indent.

Single crystal indents from both grains were included rather than only the single crystal indent of the parent grain because the deformation across the grain boundary will follow the orientation of neighboring grain, not the parent grain. Of course, the neighboring grain will be under a different state of stress than that portion of the neighboring grain's single crystal indent, therefore, the resulting topography of the neighboring grain in the subtraction should be viewed with that in mind.

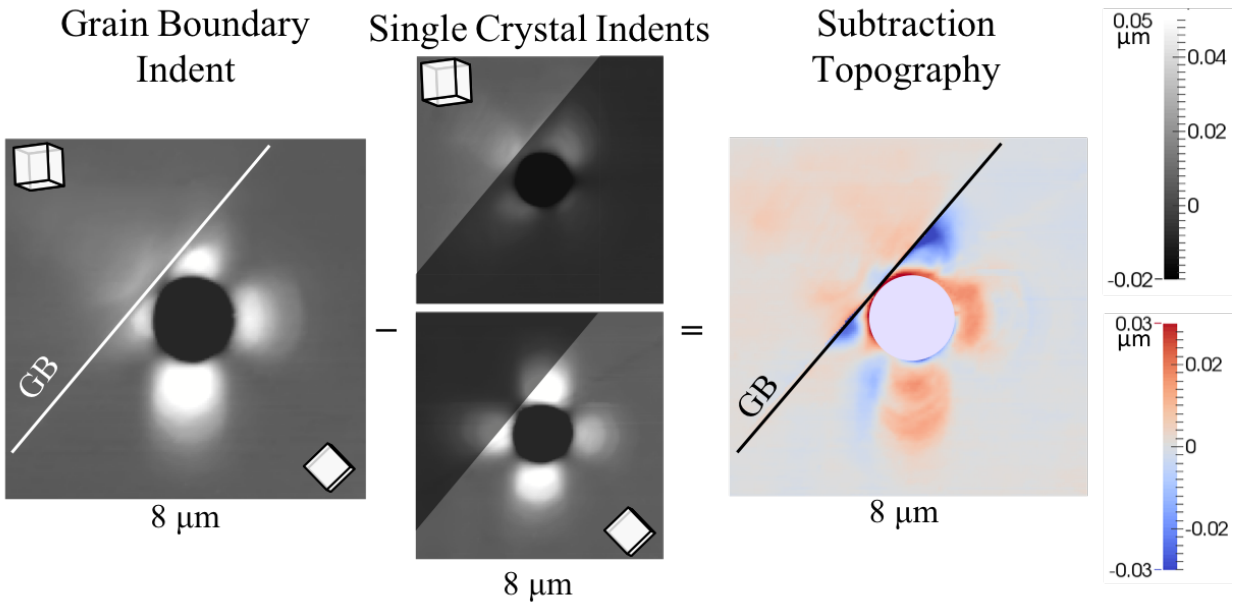

Figure 3.2: Example of topography subtraction of AFM measurements for a grain boundary indent and the corresponding single crystal indents.

The interpretation of the subtraction result is taken from the red and blue topography in the subtraction topography result in the right of Figure 3.2. Red topography in the subtraction result indicates higher topography, or more deformation, in the grain boundary indent and blue topography indicates higher topography, or more deformation, in the single crystal indents.

The second subtraction comparison was between the CPFEM grain boundary indent simulations and experimental grain boundary indents. This is more straight forward than the single crystal indents as it is a single indent subtracted by a single indent. But since the CPFEM mesh is not the same exact size/shape as the experimental AFM map, a place holder topography height of zero was place around the CPFEM mesh so that the maps would line up for subtraction method.

3.5 ECCI vs. CC-EBSD

A 25 × 22 array of nanoindents with 10 μm spacing was placed in a Ta sample, resulting in a large number of indentations that were well-isolated from grain boundaries and a few indents located close to grain boundaries. Analysis was carried out over four areas, two single crystal indents, one grain boundary indent, and a group of four indents that consisted of three indents near the grain boundary and one single crystal indent.

ECCI, CC-EBSD, and AFM were performed on both a single crystal and a grain boundary nanoindent. The ability for ECCI and CC-EBSD to map dislocation distributions and densities were compared. For a single crystal indent, dislocations were characterized using both ECCI and CC-EBSD, however, dislocations at the grain boundary could not be characterized using CC-EBSD because the algorithm that splits the GND density onto specific slip systems did not converge to an answer (this was attributed to low quality of the EBSD patterns). Also, a

coarser EBSD scan was carried out over the set of four indents to demonstrate the efficiency of CC-EBSD to assess dislocation pile-ups at grain boundaries.

3.5.1 ECCI of Nanoindents

ECCI was carried out using the previously mentioned Tescan Mira 3 at 30 kV using a working distance of approximately 9 mm, an instrument spot setting of 6.1 nm, and a specimen current of 2.2 pA. Specific channeling conditions were established using SACPs facilitated by the beam rocking function. The individual bands within the SACPs were indexed using grain orientation data obtained from EBSD. $\mathbf{g} \bullet \mathbf{b} = 0$ analyses were carried out to determine the dislocation types (edge or screw) and Burgers vectors. Where necessary, tilt analysis was carried out to determine dislocation line directions.

3.5.2 CC-EBSD of Nanoindents

EBSD patterns for cross-correlation analysis were collected around the same indentation regions that were examined with ECCI, using step sizes of 100 nm, 50 nm, and 25 nm. Patterns for cross-correlation were captured using the same Tescan SEM and previously mentioned EDAX Hikari EBSD system. To acquire EBSD patterns with high contrast and low noise, necessary for cross-correlation analysis, an instrument spot size of 20.0 nm and specimen current of 1.9 nA was used with an exposure time of 0.1 s. The patterns were not binned, but the 480 x 480 pixel resolution used is comparable to 2 x 2 binning for cameras that have 1000 x 1000 pixel resolution.

Neighboring patterns were cross-correlated in two directions using the OpenXY software [94] to obtain the relative elastic distortion between the crystal lattices at the relevant scan points [95]. The GND density is calculated from these elastic distortions. Since the calculated GND density is sensitive to the chosen scan step size, the software allows selection of a step size that is

a multiple of the original scan step size; i.e. the cross-correlation calculation for the distortion gradient can be calculated between nearest neighbor points, next-nearest neighbor points, etc; resulting in a range of effective step sizes. Ruggles et al. [95] discussed the necessity to find a range of effective step sizes where the associated GND densities become relatively constant in order to accurately determine the "true" GND density; for Ta, they found this range to be between 100 nm and 200 nm.

To determine the necessary effective step size for calculating GND densities for this work, an EBSD scan was collected with a 25 nm step size and GND densities were calculated using effective step sizes between 25 nm and 40 nm, shown in Figure 3.3 as box plot distributions of measured densities for each effective step size. At an effective step size of 175 nm, Figure 3.3 shows that GND densities enter a region where they become relatively constant, in agreement with the results by Ruggles et al. [95].

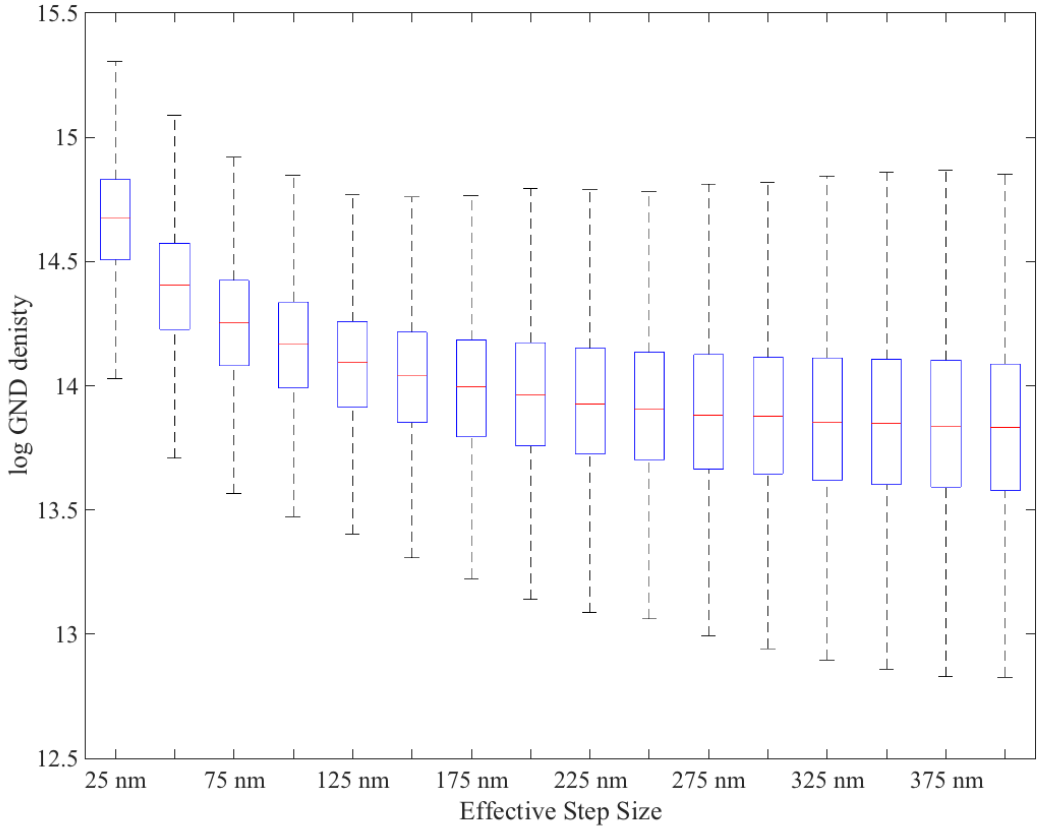

Figure 3.3: Box plots showing GND density distributions for effective step sizes between 25 nm and 400 nm.

3.6 Analysis of Wedge Indent Cross-Section

ECCI and EBSD analyses were carried out on a single crystal Ta sample that was deformed at room temperature under wedge indentation. The sample was deformed and prepared for analysis by researchers under the direction of Dr. Jeff Kysar at Columbia University. The indenter had an angle of 90° and the indentation depth was ~200 μm. The wedge indenter was specifically aligned with the crystal orientation so that the loading axis of the indenter was aligned with the [-110] direction and the wedge was parallel with the [110] direction. This was done in order to produce plane strain in the (110) plane [96]. Following indentation, the sample was cut in half perpendicular to the wedge indent and then the new sample surface was polished for analysis (i.e. plane strain occurs in the sample surface plane). Similar sample preparation methods were carried out for a wedge indent in fcc nickel, as outlined by Kysar et al. [97].

CC-EBSD was previously performed on the prepared Ta sample at a step size of 2.5 μm over an area of 1 x 1 mm. Ruggles et al. [80] estimated the GND density from CC-EBSD analysis, shown in Figure 3.4. The ECCI and EBSD analyses in this work focused on a small area about 90 μm below the corner of the indent. This area is boxed in of Figure 3.4.

The ECCI analysis was carried out on the same previously mention Tescan Mira 3 and at 30 kV using a working distance of approximately 9 mm, an instrument spot setting of 6.1 nm, and a specimen current of 2.2 pA. EBSD was also carried out using the Tescan Mira 3 and the same EDAX camera system as previously discussed. The beam conditions were different from CC-EBSD in that the accelerating voltage was 20 kV with an instrument spot size of 49 nm and a specimen current of 1.1 nA. EBSD data was acquired using a step size of 60 nm over an area of 23 μm x 50 μm. EBSD points that had a confidence index less than 0.15 were discarded.

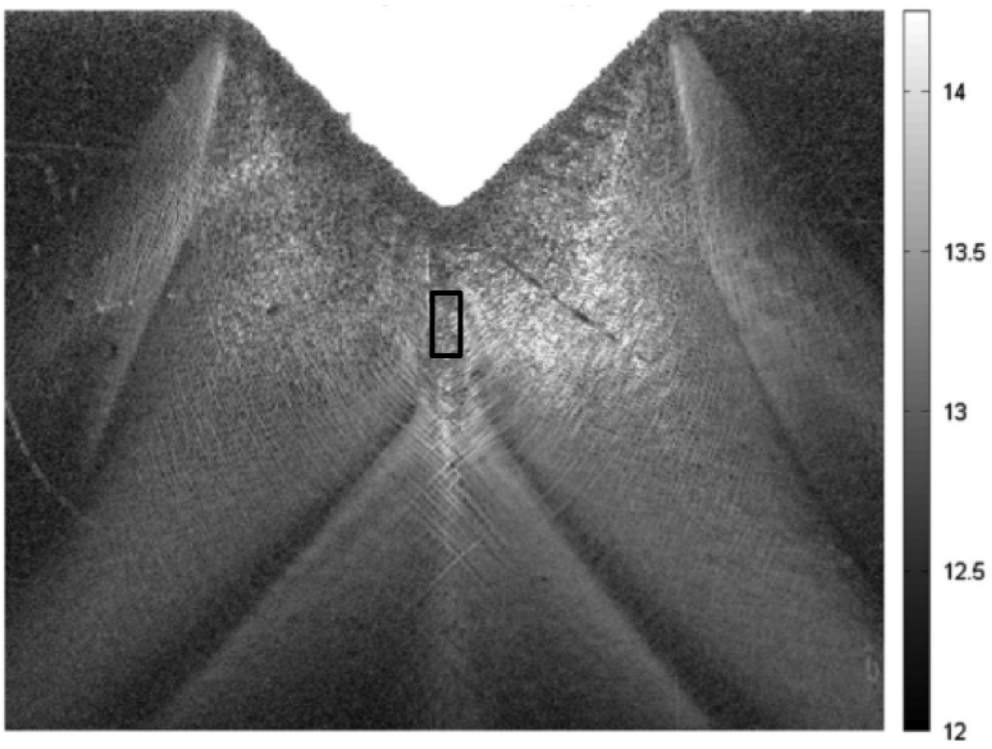

Figure 3.4: CC-EBSD derived GND map of a wedge indent that was cut in half and polished. EBSD patterns were collected at a step size of 2.5 μm and the area mapped is 1 x 1 mm. The units are log m/m^3 [80]. The area analyzed in the present study is boxed.

4 Results

4.1 Single Crystal Microindentation

Single-crystal microindentation demonstrates that the indent topography for Ta changes as a function of grain orientation. Figure 4.1 illustrates this by showing the indent topographies plotted on the bcc stereographic triangles. The topography measurements exhibit a higher intensity (brighter) for positive out-of-plane topography and lower intensity (darker) for negative out-of-plane topography. Positive topography is generally observed in the topographical lobes, negative topography is observed in the middle of the indent (where the indenter was in contact with the surface), and areas away from the topographical lobes/indent center have a height of zero.

Grains oriented with their indentation axis near [001] display four-fold symmetry, grains oriented near [101] have two-fold symmetry, and grains oriented near [111] display three-fold symmetry. The topographical lobes are generally at the highest heights along the <111> directions that project from the middle of the indent. Indents in the [001] oriented grains show four lobes equally separated from one another. Indents in the [101] oriented grains show two pairs of lobes on opposite sides of the indents. Indents in the [111] oriented grains show three lobes equally arranged at 120° around the indent. As orientations gradually change from these primary orientations, the topography change is gradual as well.

The max height of each lobe for three microindents, one indent for each of the primary orientations, were measured and summarized in Table 4.1. The [100] indent has the highest lobes heights with an average of 467 nm, then [101] with 335 nm, and the [111] indent has the lowest average lobes heights with 288 nm. Since [100] had the highest average lobe height, the

[101] and [111] heights were calculated as a percentage of [100] height in order to compare later with nanoindentations.

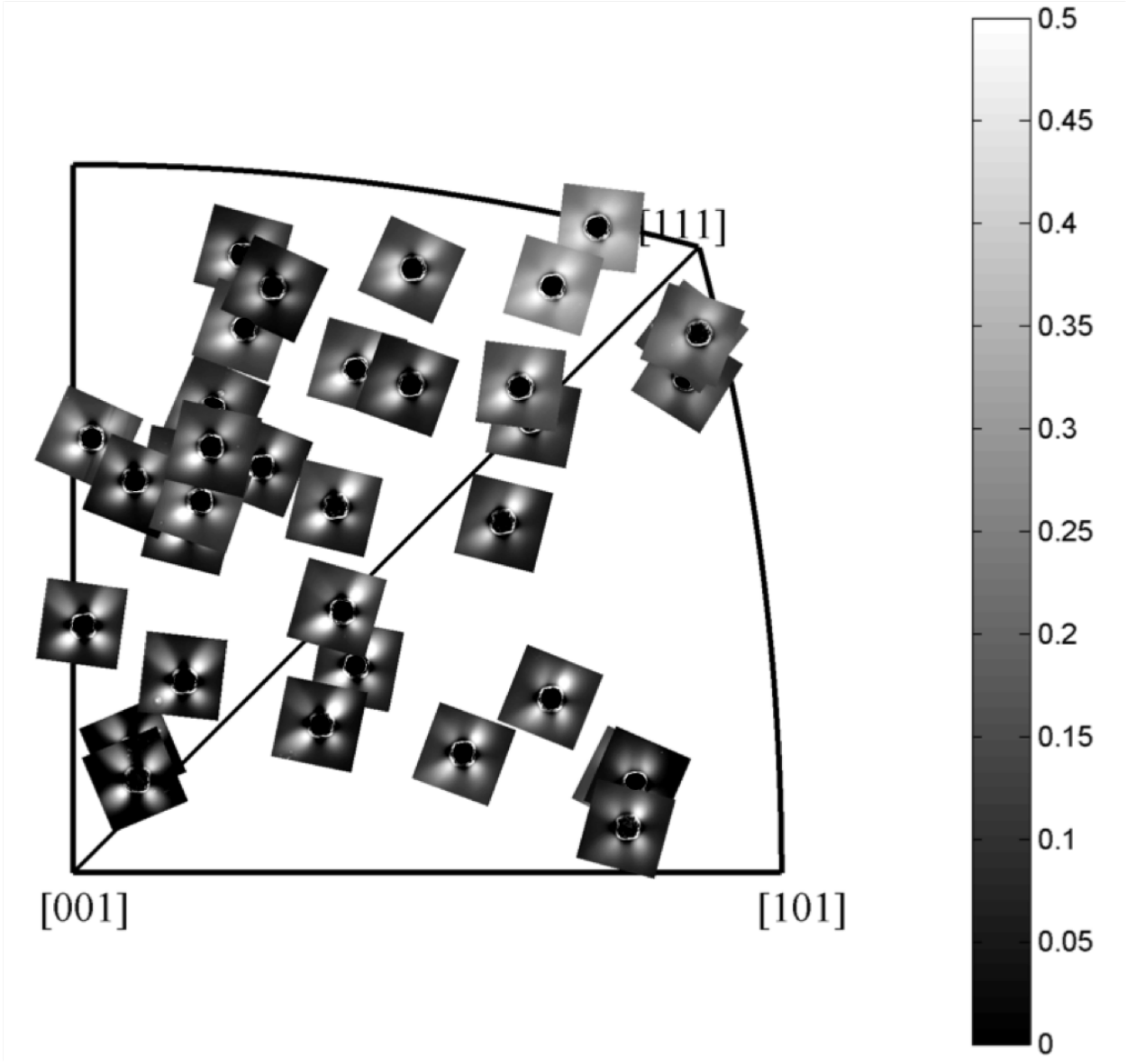

Figure 4.1: Indentations of single crystal microindents plotted on a portion of a bcc stereographic projection in order to visualize indent topography as a function of orientation.

Table 4.1: Statistics of lobe heights of three microindents, one for each of the primary orientations.

Primary Orientations	[100]	[101]	[111]
Lobe #	Max Lobe Heights (nm)		
1	455	381	300
2	550	287	305
3	408	347	260
4	456	326	-
Average	467	335	288
St. Dev	60	39	25
% of [100] Height	100%	72%	62%

4.2 Single Crystal Nanoindentation

AFM measurements of nanoindents placed in the middle of grains with [001], [101], and [111] orientations are shown in the top of Figure 4.2. Similar to the microindents shown above, these nanoindents reflect four-fold symmetry for the [001] orientation, two-fold symmetry for [101] orientation, and three-fold symmetry for [111] orientation. They also agree with the fact that the lobes are generally at the highest heights along the <111> directions that project out from each indent. For indents the [001] and [111], there is an agreement on the number of topographical lobes that are observed with microindentation and nanoindentation. But for the indents in [101] oriented grains, there is only two broad lobes on either side of the nanoindent, while there are four lobes on the microindent. This is evidence of a size effect in the indentation process.

The max lobe heights of the nanoindents are summarized in Table 4.2. The [100] orientation had the highest average height 56.8 nm, then the [101] with 26.6 nm, and [111] had the lowest with 24.9 nm. The average heights of the [101] and [111], however, are statistically equivalent due to the fact that each of the standard deviations encompass the average of the other.

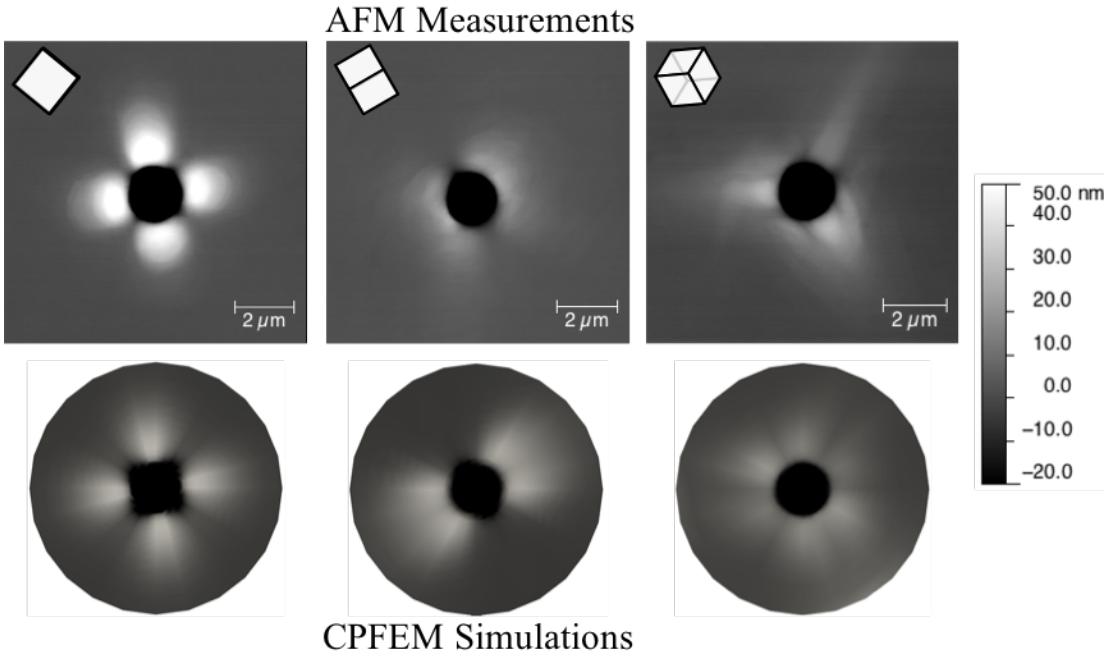

Figure 4.2: Top) Experimental topographies for the nanoindents made in grains of orientations close to [001], [101], and [111], shown left to right respectively. Bottom) Corresponding CPFEM simulations for three orientations.

Table 4.2: Statistics of lobe heights of three experimental single crystal nanoindents, one for each of the primary orientations.

Primary Orientations	[100]	[101]	[111]
Lobe #	Max Lobe Heights (nm)		
1	62.4	24.7	31.3
2	54.9	28.5	30.1
3	51.7	-	13.4
4	58.2	-	-
Average	56.8	26.6	24.9
St. Dev	4.6	2.7	10.0
% of [100] Height	100%	47%	44%

4.2.1 CPFEM of Single Crystal Nanoindentation

To test whether the CPFE model of Ta correctly predicts the topography of single crystal nanoindentation, corresponding CPFEM simulations of the three experimental nanoindents are shown in the bottom row of Figure 4.2. The [001] and [101] nanoindents appear to have reasonable agreement, particularly in terms of symmetry, but disagree in the details. The [111] has the largest disagreement between the experiment and the simulation. The agreement/disagreement between the experimental and simulated nanoindents are described below.

The [001] simulation appears to have the closest match to the experimental AFM measurement and it also shows the same four-fold symmetry. Nevertheless, there is disagreement between the [001] experiment and simulation in regards to the topographical lobe height and spread of the lobes from the middle of the nanoindent. The lobe height is higher in the experimental measurement and the lobes in the simulation extend further out from the middle of the indent. For both the experimental and simulated nanoindents, there are four corners along the edge of the indent rim between the four lobes. These corners are more exaggerated in the simulated indent.

The [101] experimental and simulated indents also show agreement in terms of the 2-fold symmetry of the lobes. The experimental indent appears to have the same lobe height as the simulation near the edge of the indent but, going further out from the middle of the indent, the lobe height drops off more quickly than in the simulated indent. Along the indent rim of the simulated indent there are two distinct corners between the two lobes on the top-left and bottom-right of the indent, similar to the corners found in the [001] indent. The experimental indent only shows one distinct corner on the top-left, but there is still separation between the lobes on the

bottom-right. Also, the lobes of the experimental indent appear to surround more of the indent center, while the simulated indent has a larger gap with no topography between the lobes, at the top-left and bottom right of the indent center.

While the experimental [111] nanoindent has 3-fold symmetry, the simulated nanoindent is closer to 6-fold symmetry. In the places where the experimental nanoindent shows the highest topography, the simulated nanoindent shows zero topography. Also, the three lobes in the experimental nanoindent come to a point further out from the indent while the simulated indents appears to have six lobes that fan out moving further from the indent.

4.3 Bi-crystal/Grain Boundary Nanoindentation

To characterize the manner in which grain boundaries influence strain transfer, over 200 nanoindents were placed near grain boundaries. Even with this many nanoindents, the secondary pop-ins, or grain boundary pop-ins, that are discussed in the literature were not observed in Ta. This indicates that there is no conclusive evidence that secondary pop-ins occur in Ta.

Three grains boundaries were selected for more in-depth analysis of deformation transfer with each grain boundary having a nanoindent on either side of the grain boundary, shown in Figure 4.3. In the left column are BSE images of the three grain boundaries analyzed with each grain boundary indent identified by a number at the lower right of the indent and the *m'* value for the grain boundary at the top of the image. The *m'* value is based on the closest aligned slip systems since the activated slip systems are unknown. The middle-left column shows the AFM measurements of each of the grain boundary indents. The middle-right column shows the AFM measurements of the single crystal indents that correspond to the grains that each grain boundary indent was made in. The right column shows the results of the subtraction procedure outlined in section 3.4.2.

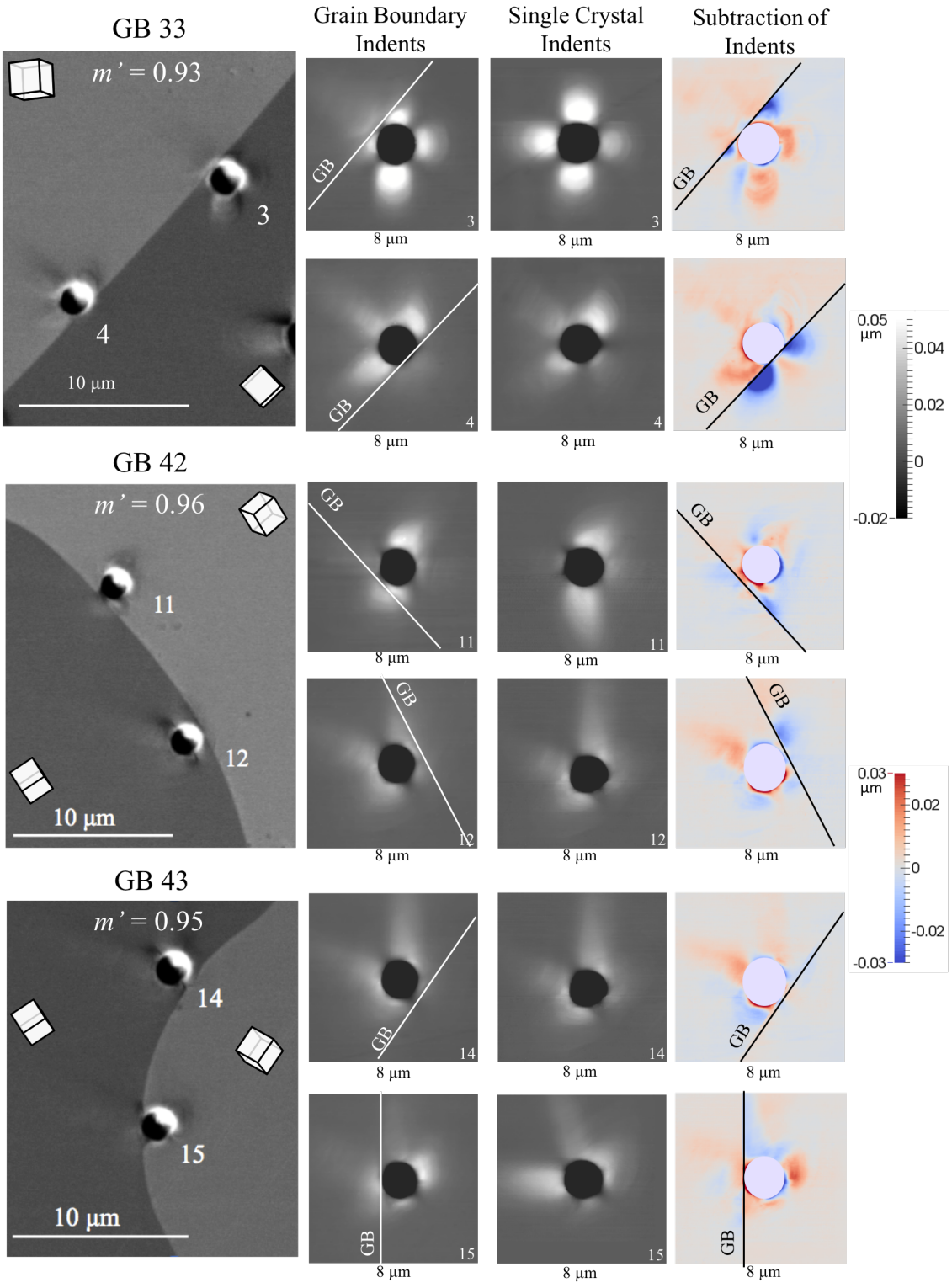

Figure 4.3: Left) BSE image of indents along three grain boundaries. Middle-left) AFM measurements of the grain boundary nanoindents. Middle-right) Single crystal nanoindents that correspond to each of the grain boundary nanoindents. Right) Subtraction of the grain boundary AFM measurement with corresponding single crystal indents.

From the AFM grain boundary measurements in the middle-left column in Figure 4.3, strain transfer is considered to have occurred if topography appears across the grain boundary from the indent and not to occur if there is no topography across the boundary. All three grain boundaries show that strain transfer is more significant from one indent and less prevalent, or non-existent, from the indent on the opposite side of the grain boundary. This suggests that grain boundary strain transfer is dependent on the direction the shear approaches the boundary. This also shows that even though all grain boundaries have reasonably high *m'*, strain transfer should not be predicted solely on slip system alignment.

For grain boundary 33, the AFM grain boundary maps show significant strain transfer for indent number 3, but little strain transfer for indent number 4. Regardless of amount of strain transfer between the two grain boundary indents, the subtraction results for both show significant strain transfer resistance. This is exhibited by red (positive) topography in the parent grains of the subtraction result.

On grain boundary 42, the AFM grain boundary measurements shows significant strain transfer for indent 11 and very little to no strain transfer for indent 12. The subtraction result for indent 11 shows a slightly positive topography at the top right of the indent indicating a small amount of resistance to strain transfer. Indent 12 also shows a small amount of resistance to strain transfer due to positive topography at the top left of the indent.

For grain boundary 43, the AFM grain boundary measurements show no strain transfer for indent 14 and significant strain transfer for indent 15. The subtraction result of indent 14 suggests very little resistance to strain transfer due to the slightly positive topography above the indent. On the other hand, the subtraction result for indent 15 suggests strong resistance to strain transfer due to the positive topography, indicated by the bright red, to the right of the indent.

4.3.1 CPFEM of Grain Boundary Nanoindentation

A comparison of the AFM measured topographies to CPFEM topographies are shown in Figure 4.4. The AFM measurements are shown in the left column, CPFEM results are shown in the middle column, and the subtraction results (CPFEM minus AFM) are shown in the right column. The simulation for grain boundary indent 11 at grain boundary 42 did not converge to a solution, so this indent is ignored for the comparison between AFM and CPFEM.

CPFEM simulations of grain boundary indents agree with AFM measurements in that they also indicate that grain boundaries can have an effect on indent topography/strain. Upon closer comparison to the AFM measurements, however, the effect that grain boundaries have on topography is only reasonably similar to experimental indents 3 and 4 for grain boundary 33, in that the experimental and simulated indents at grain boundary 33 have the best topographical alignment on both sides of the grain boundary. Comparison of CPFEM results and AFM measurements for other indents show a clear difference in topography.

The CPFEM results indicate topography transfer across the grain boundary for every grain boundary indent, disagreeing with the AFM results of indents 12 and 14. As for indents 4 and 15, CPFEM results agree with the AFM measurements that topography transfer occurs, but the CPFEM significantly over-estimates the amount topography transfer. This is indicated by the red topography in the subtraction result of the neighboring grain.

Indent 3 has the best match between CPFEM and AFM for the overall indent topography in the parent grain and the amount of topography transferred into the neighboring grain. For all other indents the CPFEM overestimates the topography of the parent grain and the topography transferred into the neighboring grain.

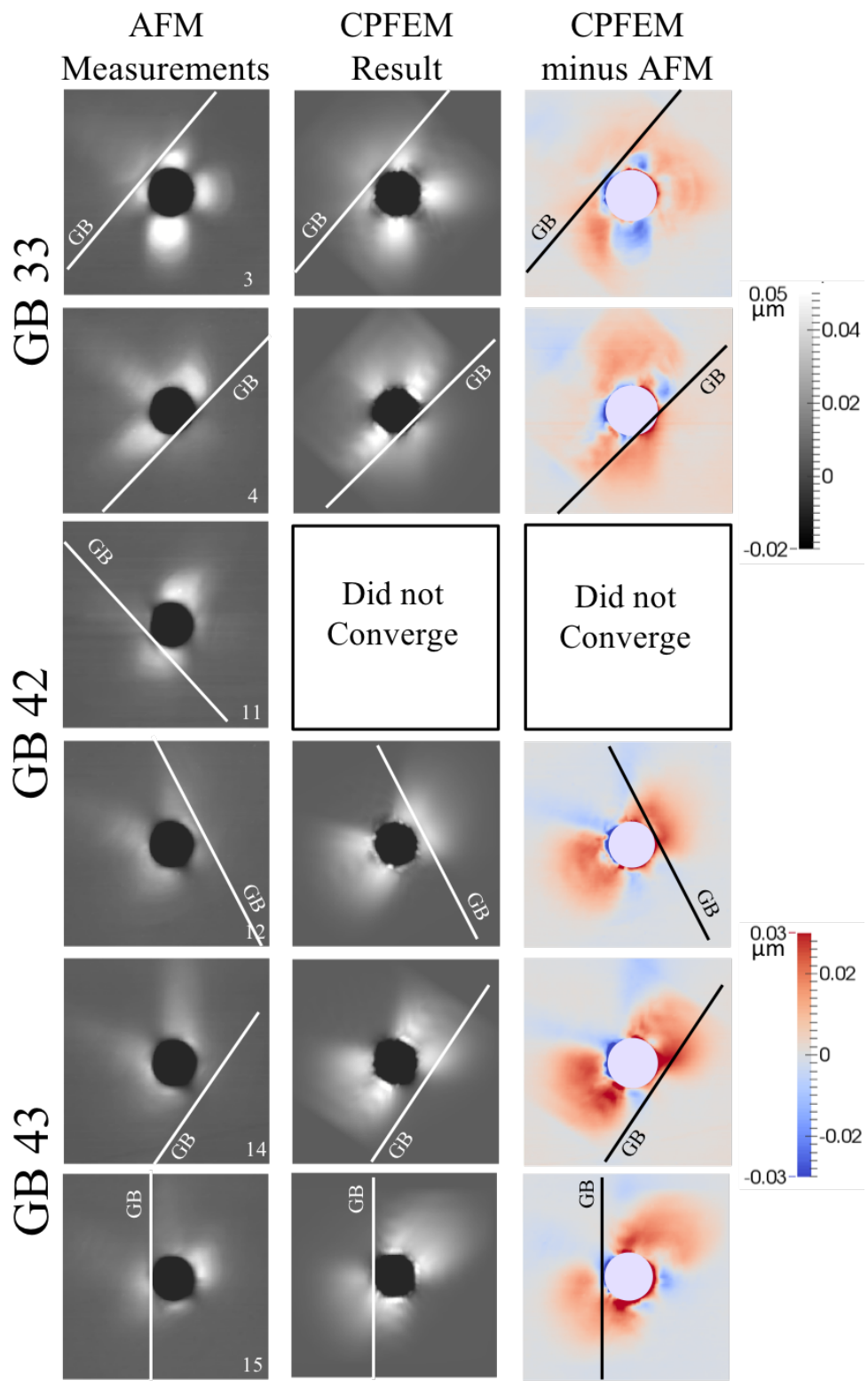

Figure 4.4: Left) AFM measured topographies of experimental nanoindents near grain boundaries. Middle) CPFEM topographies of the same grain boundary experimental indents. Right) Subtraction result of CPFEM minus AFM topographies.

4.4 ECCI vs. CC-EBSD for Single Crystal Indentation

4.4.1 Dislocation Distributions

The dislocation distribution around a single crystal indent in a grain oriented near [011] was analyzed. Figure 4.5a, which was produced by taking multiple ECC images at the **g** = (-21-1) channeling condition and stitching them together, shows the general deformation fields around the indent. The strong intensity near the edge of the indentation can be attributed to the nominally tear shaped backscattered electron interaction volume escaping from the interior surface of the indent when the electron beam is scanned close to the edge of the indent. This effect is most likely complicated by the extensive deformation and localized rotations expected near the indent. Furthermore, the bright region appears asymmetrical due to the sample being tilted. Moving away from the high intensity region, dislocation fields extend from the indent in a number of directions. Most of the dislocations in these fields appear as black/white dots, representing dislocations roughly normal to the surface (examples shown in the dashed circle in Figure 4.5a), but some appear more extended due to their lines being more parallel to the surface (example shown in dashed rectangle in Figure 4.5a). More detailed images showing individual dislocations are illustrated in subsequent figures. The corresponding CC-EBSD calculated GND map (total GND density), shown in Figure 4.5b, displays dislocation distributions comparable to those in the ECC image. The pixels that correspond to EBSD patterns that have a confidence index less than 0.15 are whited-out.

The topography of the same indent was measured with AFM and is shown in Figure 4.6. The stitched ECC image and the GND map from Figure 4.5, as well as the AFM measurement, reflect two-fold symmetry about the [011] axis.

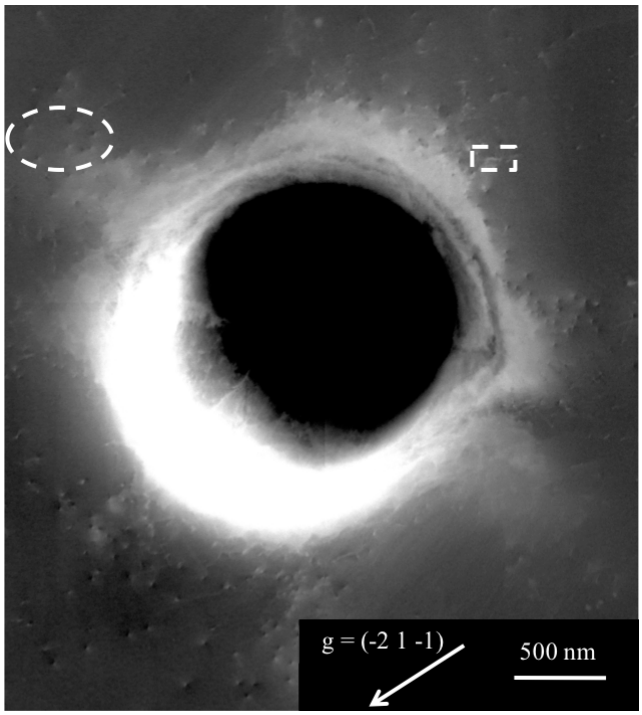

a)

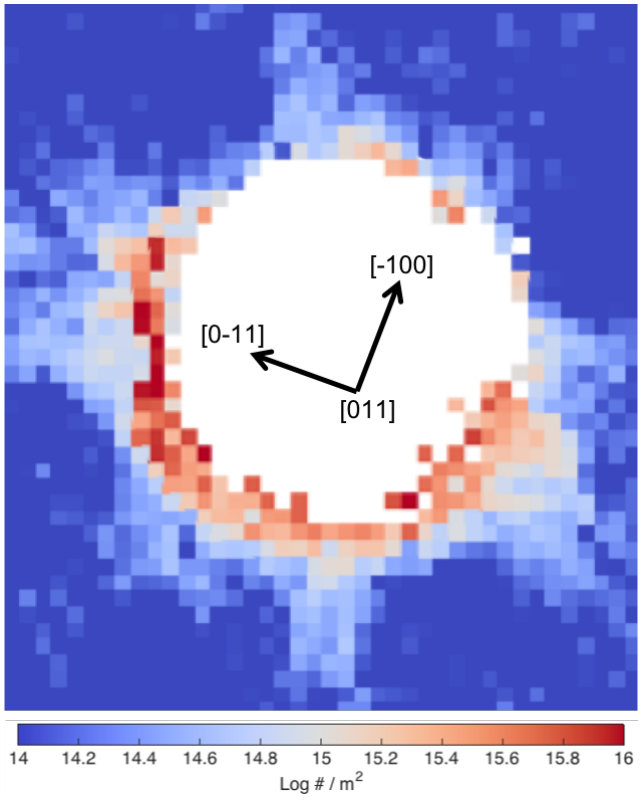

b)

Figure 4.5: a) Multiple ECC images stitched together showing dislocations generated from a single crystal nanoindentation in a grain of approximately [011] orientation. b) CC-EBSD GND map of the same area, collected with an EBSD scan step size of 100 nm and effective step size of 200 nm, showing dislocation distributions similar to that in the ECC image.

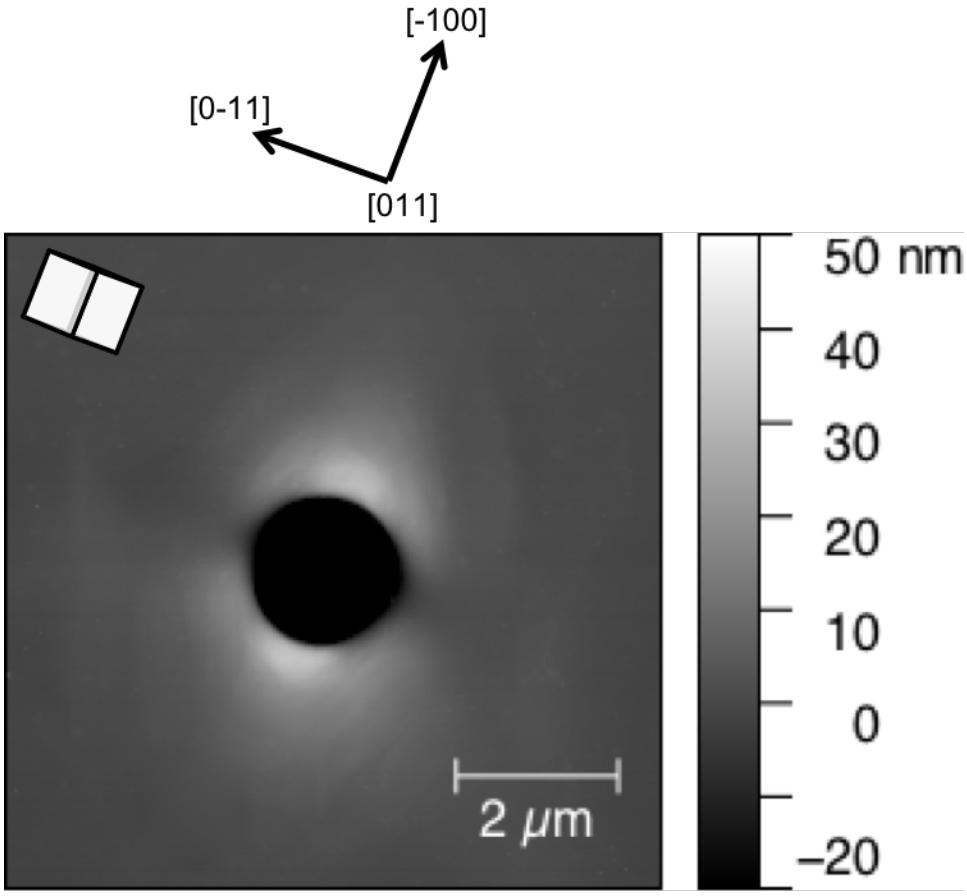

Figure 4.6: AFM measurement of the same single crystal indent that was imaged and GND mapped in Figure 4.5.

4.4.2 Dislocation Density Comparison

A more detailed comparison between the ECCI and CC-EBSD results, carried out on a neighboring indent within the same grain, is shown in Figure 4.7. Here the ECCI, Figure 4.7a, shows a broad band of dislocations extending to the upper left of the indent and a fainter band near the right hand edge of the image, which curves to the left moving up in the image. Individual dislocations can be readily discerned, with the majority of the dislocations appearing close to end-on in the image. As before, there are also smaller numbers of dislocations with line directions more parallel to the sample surface.

A comparison of this image with the corresponding GND map from CC-EBSD, Figure 4.7b, again shows good agreement with the approximate locations of the dislocations. Nevertheless, there is not an exact one-to-one correlation between ECCI and the CC-EBSD images for reasons which will be discussed below. In order to facilitate a robust comparison, the ECC image was gridded to the same step size as the EBSD scan, shown in Figure 4.7c. The number of dislocations in each grid square were counted and divided by the area of the grid square to give an effective dislocation density. This result is shown in Figure 4.7d and is plotted with the same color scale as the CC-EBSD derived GND map. Regions of the ECC image where dislocations could not be reliably imaged, i.e. the indent rim and inside the indent, are whited-out, seen in the lower right Figure 4.7d.

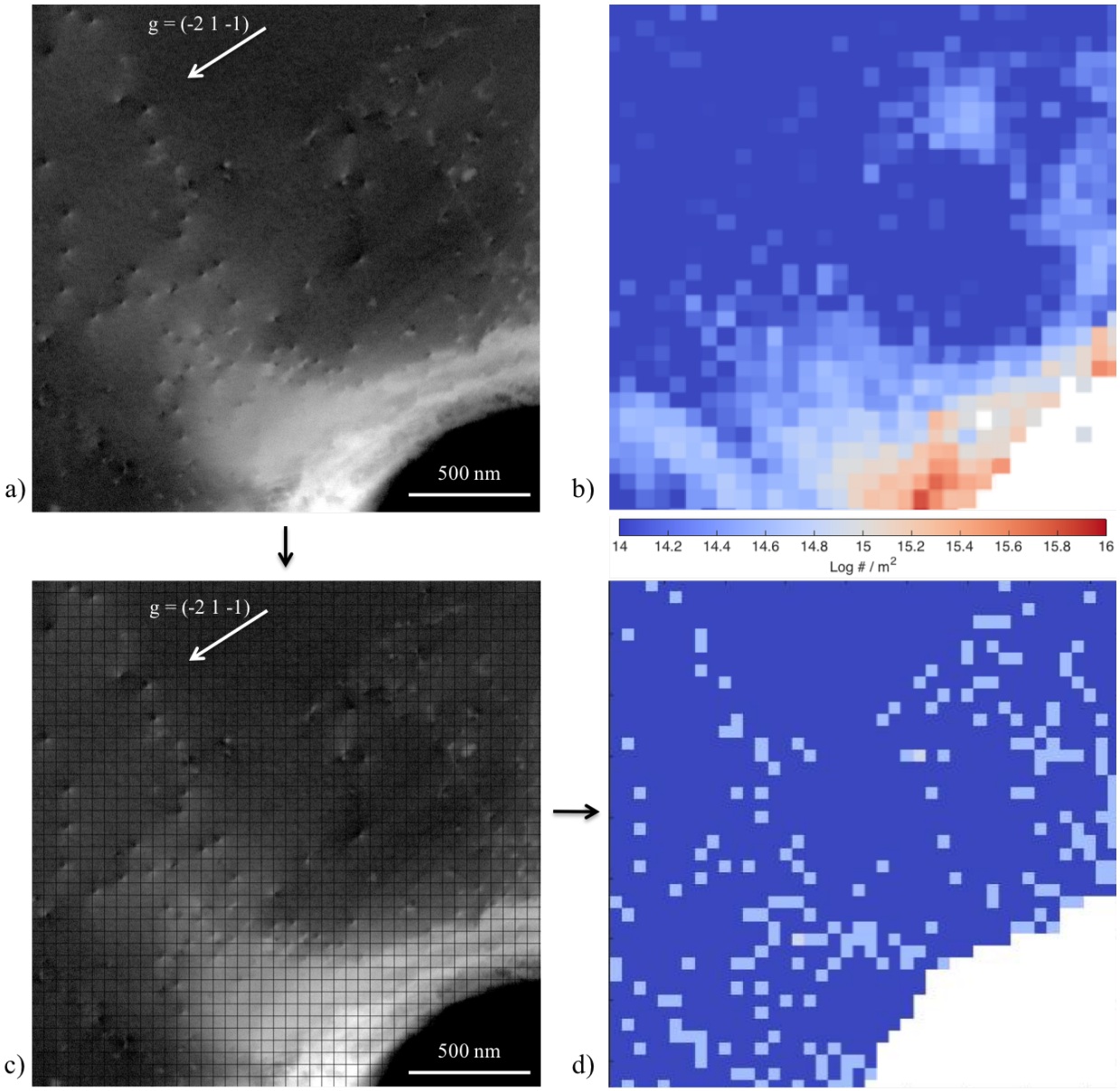

Figure 4.7: a) ECC image of dislocations from the upper-left of an indented area. b) CC-EBSD generated GND density map of the same area showing similar dislocation distributions, using a step size of 50 nm and an effective step size of 200 nm. c) ECC image gridded to the same size as the EBSD step size. d) Dislocation density map calculated by counting dislocations in each grid square of gridded the ECC image.

4.4.3 Dislocation Characterization Using ECCI

The dislocations imaged using ECCI were characterized using channeling contrast criteria supplemented with the approximate line directions [73–76]. This analysis is focused on the region outlined by white dashes in the upper left portion in Figure 4.8a. This image, collected using the **g** = (-21-1) channeling condition, shows what appears to be 64 dislocations in the circled region, (in a few cases the contrast is complicated and may represent more than one dislocation). Careful examination of these dislocations reveals that many of them have their characteristic black/white contrast in the same orientation, while others display reversed or rotated contrast. These differences in contrast can indicate different Burgers vectors and/or edge or screw type dislocations [69, 98, 99]. Overall, 39 of the dislocations reveal the same contrast orientation, with four having reversed contrast. An additional 21 display different contrast orientation or are difficult to categorize due to weak contrast.

The six different channeling conditions used for the analysis shown in Figure 4.8 were established by rotating and tilting the sample in conjunction with SACPs. The majority of the dislocations do not go out of contrast with any of the channeling conditions, but the orientation of the black/white contrast varies with each channeling condition. The fact that the dislocations do not go out of contrast suggests that these are screw dislocations that are generally perpendicular to the surface. That is, despite the fact that $\mathbf{g} \bullet \mathbf{b} = 0$ for all of the **g** vectors perpendicular to the screw line direction, the surface relaxation causes them to always be visible [70]. The white dashed arrows in Figure 4.8 shows that the direction of the black to white contrast is roughly perpendicular to **g**, consistent with the contrast expected from screw dislocations generally perpendicular to the surface [69, 98, 99].

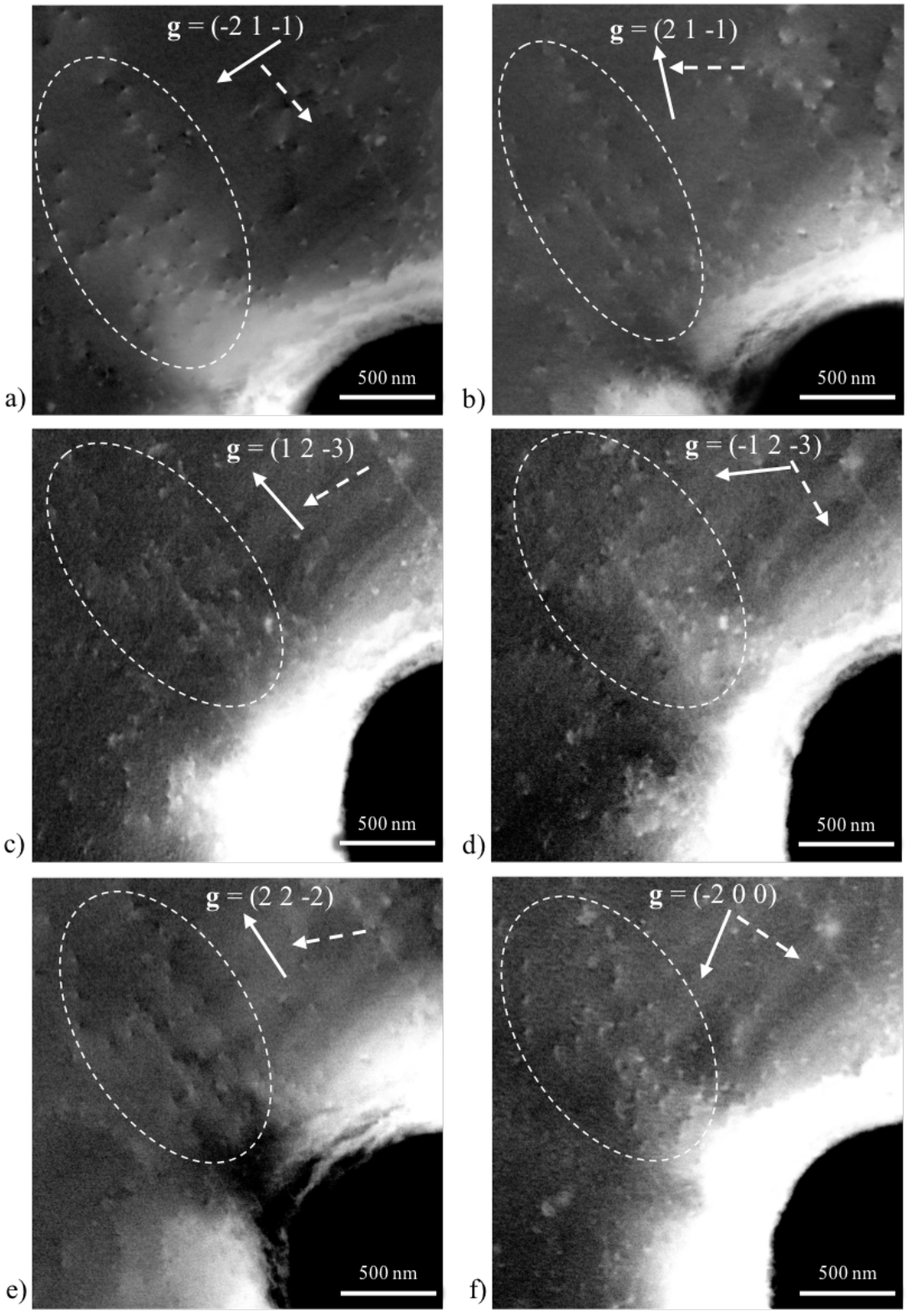

Figure 4.8: ECC images for the channeling conditions used for contrast analysis, with **g** indicated by the white arrows and the black to white contrast indicated by the white dashed arrows.

The four possible <111> screw dislocation line directions in this region are each shown as an "x" on the stereographic projection with respect to the backscatter detector, shown in Figure 4.9a. Two of these line directions, the [1-11] and [-1-11] are nearly parallel and can be eliminated as potential Burgers vectors/line directions of the dislocations that are close to perpendicular. To distinguish between the two remaining possibilities, [111] and [-111] (which are 40° and 31° from perpendicular to the beam axis, respectively), the sample was tilted 11° along **g** = (-21-1), with the resulting orientation shown in the stereographic projection in Figure 4.9b. This tilt would cause [111] screw dislocations to become more parallel to the detector (48° from the beam axis) while [-111] screw dislocations would become more perpendicular to the detector (27° from the beam axis). The ECC image corresponding to this tilt, Figure 4.9c, shows the dislocations now projecting as lines that project (fade) towards the bottom of the image, indicating the majority of the dislocations have line directions close to [111]. Combined with the sense of contrast discussed above, it is reasonable to conclude that these most common dislocations are a/2 [111] screw dislocations. It is worth noting that the other dislocations that display different black/white contrast do not project in the same direction as the a/2 [111] screws, suggesting they have different line directions and Burgers vectors.

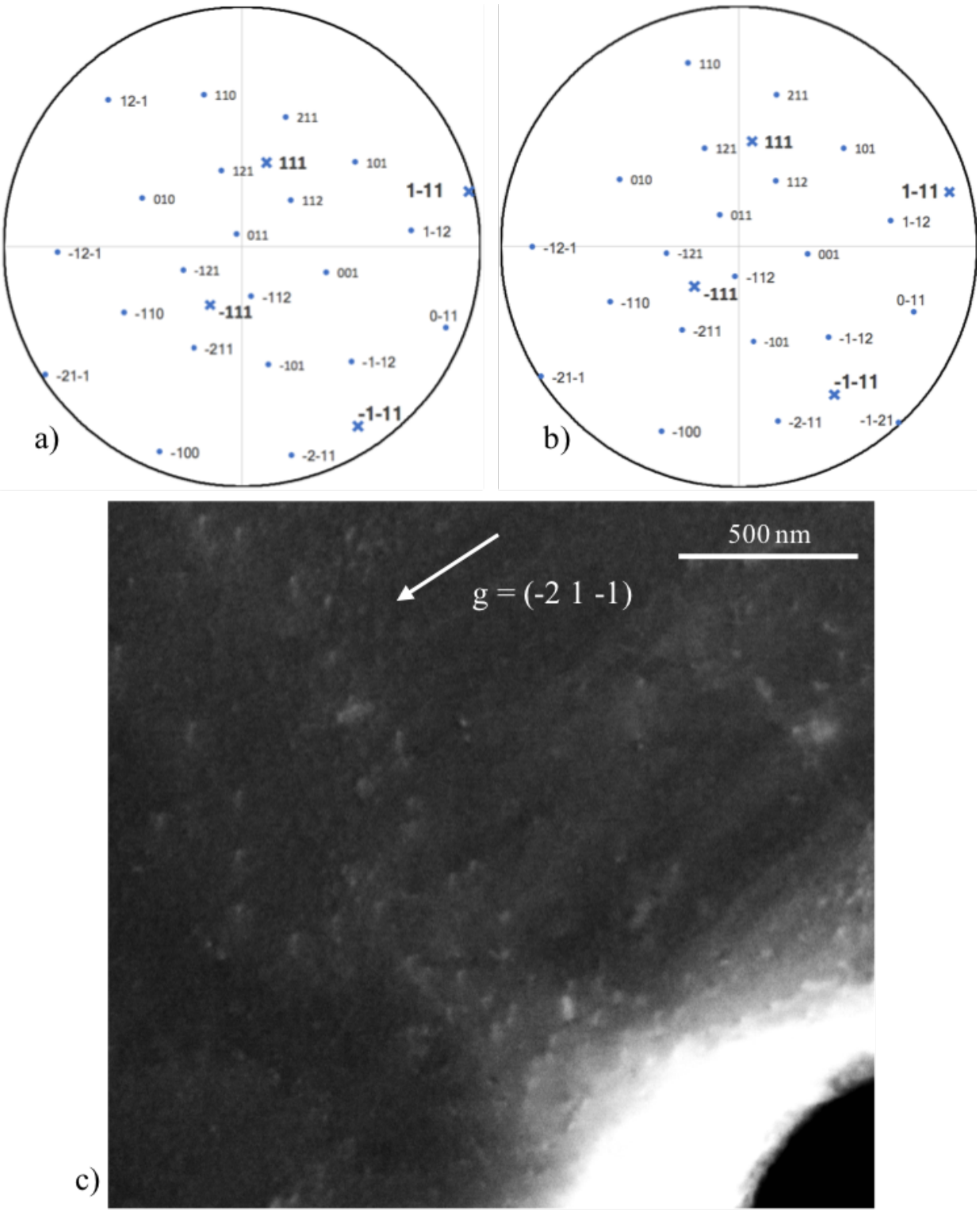

Figure 4.9: Stereographic projections a) corresponding to Figure 4.8a and b) tilted 11° along the **g** = (-21-1) with each "x" being a line direction for the four possible screw dislocations. c) ECC image with the same sample tilt as in b), showing a projection of the dislocation line directions.

4.4.4 Dislocation Characterization Using CC-EBSD

In addition to the total dislocation density shown in previous sections, the Nye tensor determined from CC-EBSD analysis may also be used to characterize the Burgers vector and edge/screw character of the local dislocation density, as well as the slip plane of the edge dislocations (the slip plane of screw dislocations is not determinable because it has no effect on the Nye tensor) via the Nye-Kröner method. The GND densities were determined using the line length minimization approach outlined by Ruggles et al. [88]. For this analysis, the smallest available effective step size of 25 nm was employed to maximize the spatial resolution of the method. The dislocation densities of each screw and edge dislocation possibility are shown in Figure 4.10. The dislocation densities were locally averaged to better show trends. In the highly deformed region near the indent, the Nye-Kröner method identifies the Burgers vector of dislocation content where ECCI was incapable of resolving dislocations. In the region further from the indent, where individual dislocations were discernible via ECCI, CC-EBSD also characterized the dislocation content as being composed of screw dislocations with a [111] Burgers vector. To highlight agreement with the two methods, the dislocation density for the [111] screw dislocation determined via CC-EBSD is shown in greater detail in Figure 4.11.

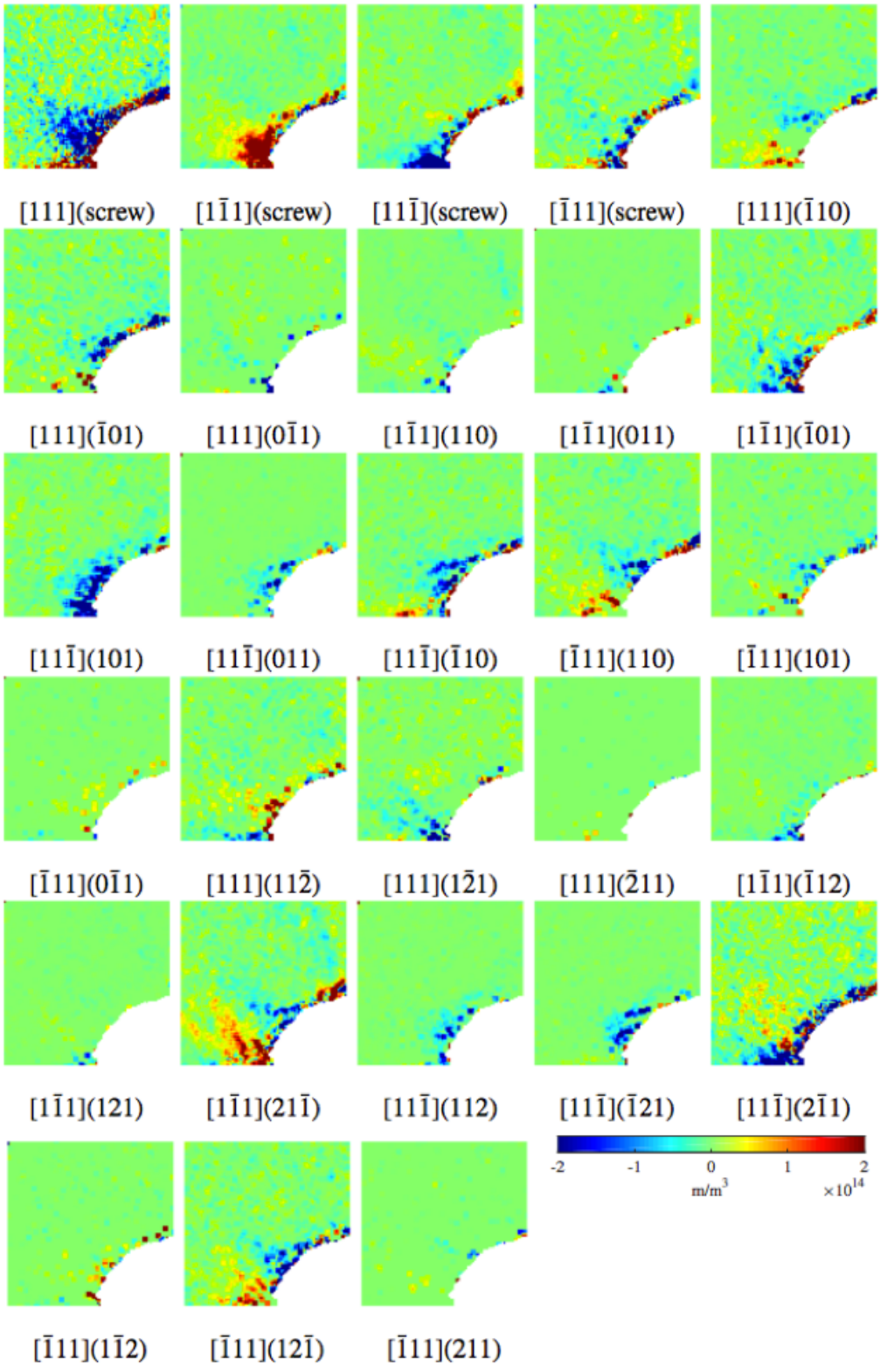

Figure 4.10: Dislocation density of each dislocation type determined using CC-EBSD.

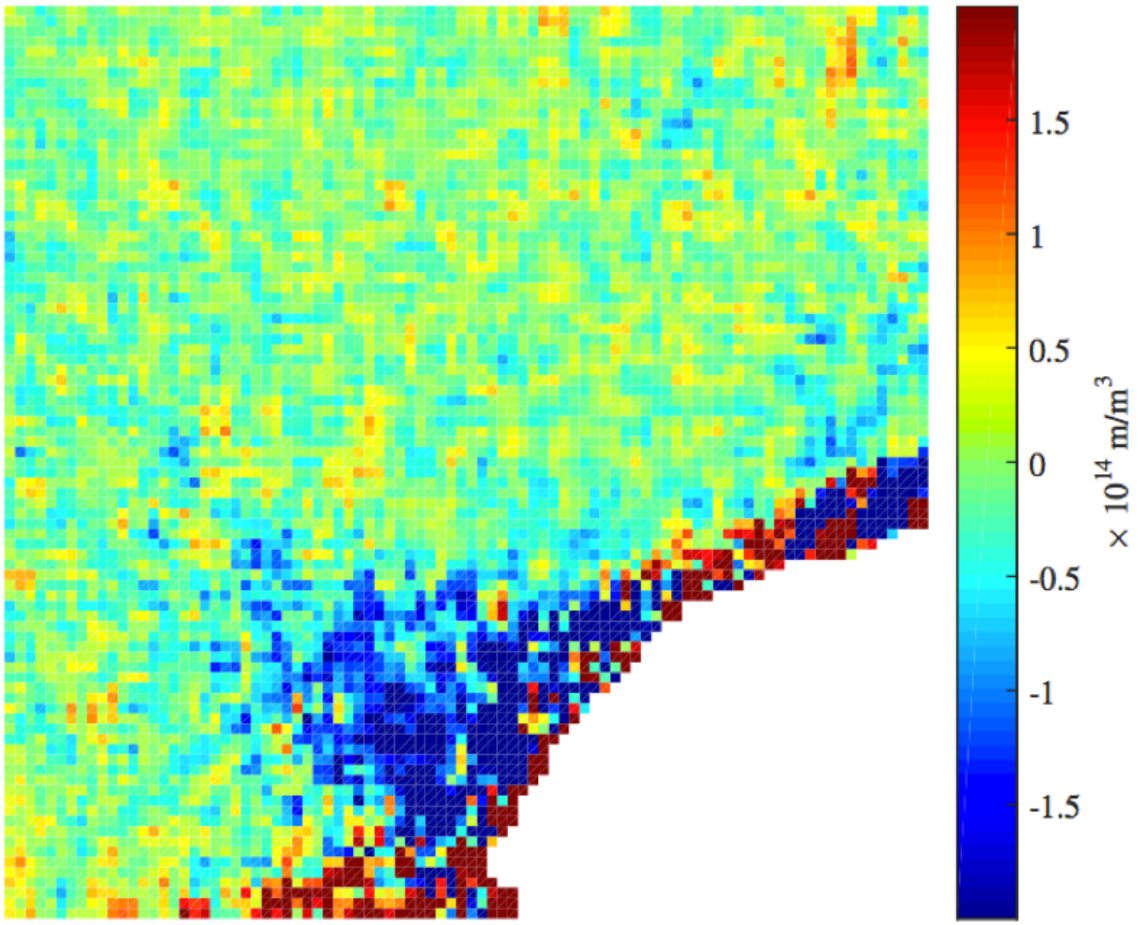

[111](screw)

Figure 4.11: Dislocation density of the screw dislocations with a Burgers vector of [111] determined by CC-EBSD.

4.5 ECCI vs. CC-EBSD for Grain Boundary Indentation

4.5.1 Dislocations Distributions

An indent located at a grain boundary triple junction was chosen for analysis of dislocations generated across a grain boundary. An overview BSE image and AFM map of the indent in is shown in Figure 4.12. The analysis was carried out at the grain boundary on the right of the indent. The AFM map, Figure 4.12b, shows topography transfer extending across the grain boundary to the right and up. The BSE image shown Figure 4.12a shows an area of bright contrast extending across the grain boundary to the right and down, away from the topography. This bright area is dislocations generated on the opposite side of the grain boundary. A higher magnification ECC image of these dislocations is show in Figure 4.13a.

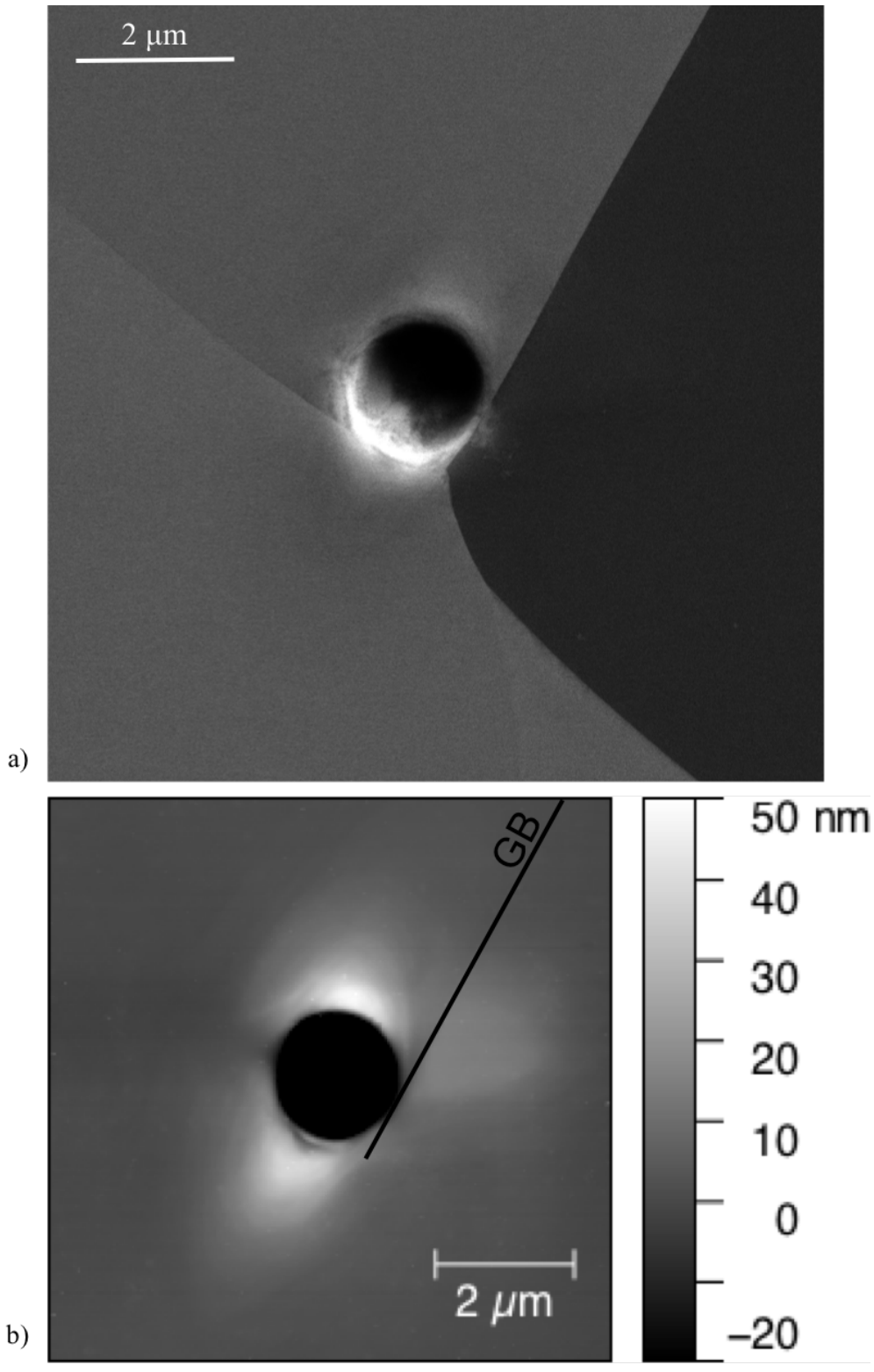

Figure 4.12: a) BSE image and b) AFM map of an indent located at a grain boundary triple junction. The analysis will be carried out at the grain boundary on the right.

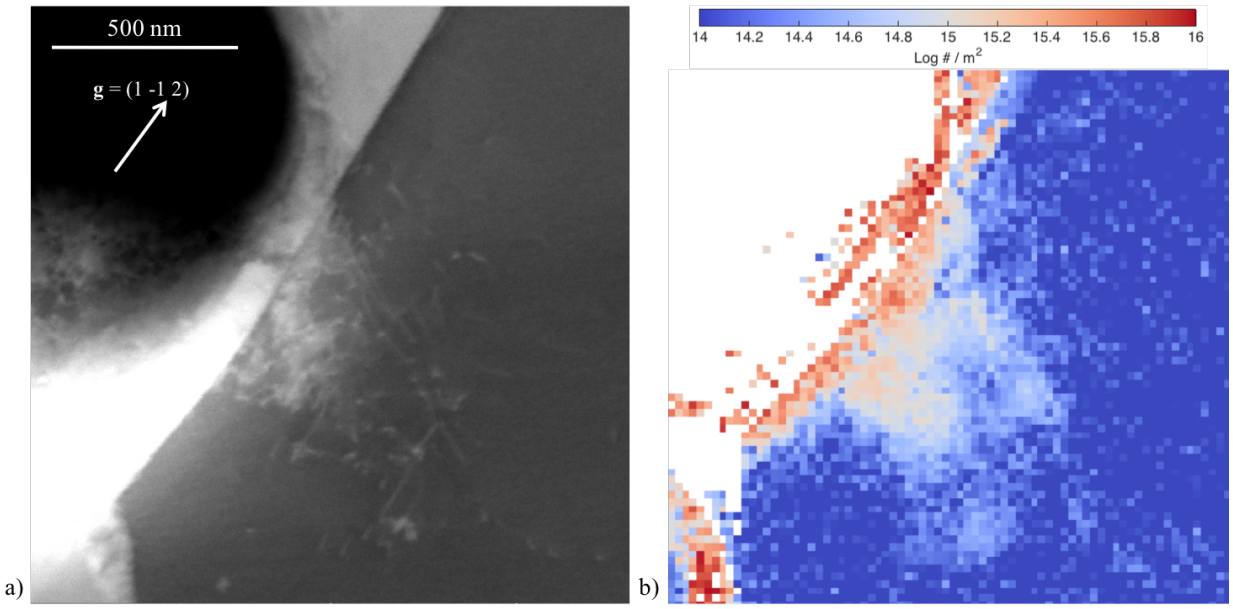

Figure 4.13: a) ECC image of the lower right of a grain boundary indent showing dislocations generated on the opposite side of the grain boundary. An CC-EBSD generated GND density map of the same area with a step size of 25 nm and an effective step size of 200 nm.

Figure 4.13a shows an ECC image of the dislocations generated across a grain boundary and Figure 4.13b shows the corresponding CC-EBSD derived GND density map. The EBSD for this map was carried out with a step size of 25 nm and an effective step size of 200 nm. In the ECC image, dislocations immediately across the grain boundary cannot be individually resolved because the concentration of dislocations is too high. Individual dislocations become discernable further away from the grain boundary. Most of the dislocations appear as lines, with a few appearing as dots, indicating most dislocations line directions are close to parallel with the sample surface.

The CC-EBSD derived GND density map in Figure 4.13b shows good agreement with the dislocation distributions of the ECC image. Just as the ECC image shows a dislocation concentration gradient moving away from the grain boundary, the GND map also shows a high density and then decreases moving away from the grain boundary. This agreement if further exhibited by looking at the areas of low dislocation density that are located amid the areas of high dislocation density in both the ECC image and GND density map.

4.5.2 Dislocation Characterization with ECCI

The dislocations generated on the opposite side of the grain boundary were characterized using $\mathbf{g} \bullet \mathbf{b} = 0$ analysis by way of the four channeling conditions shown in Figure 4.14. In this analysis, three distinct sets of dislocations were identified. Groupings of these sets are outlined in red, green, and orange. The channeling condition, $\mathbf{g} = (1\text{-}12)$, in Figure 4.14a shows all three sets of dislocation. For all other channeling conditions, one set of dislocations becomes invisible in each channeling condition.

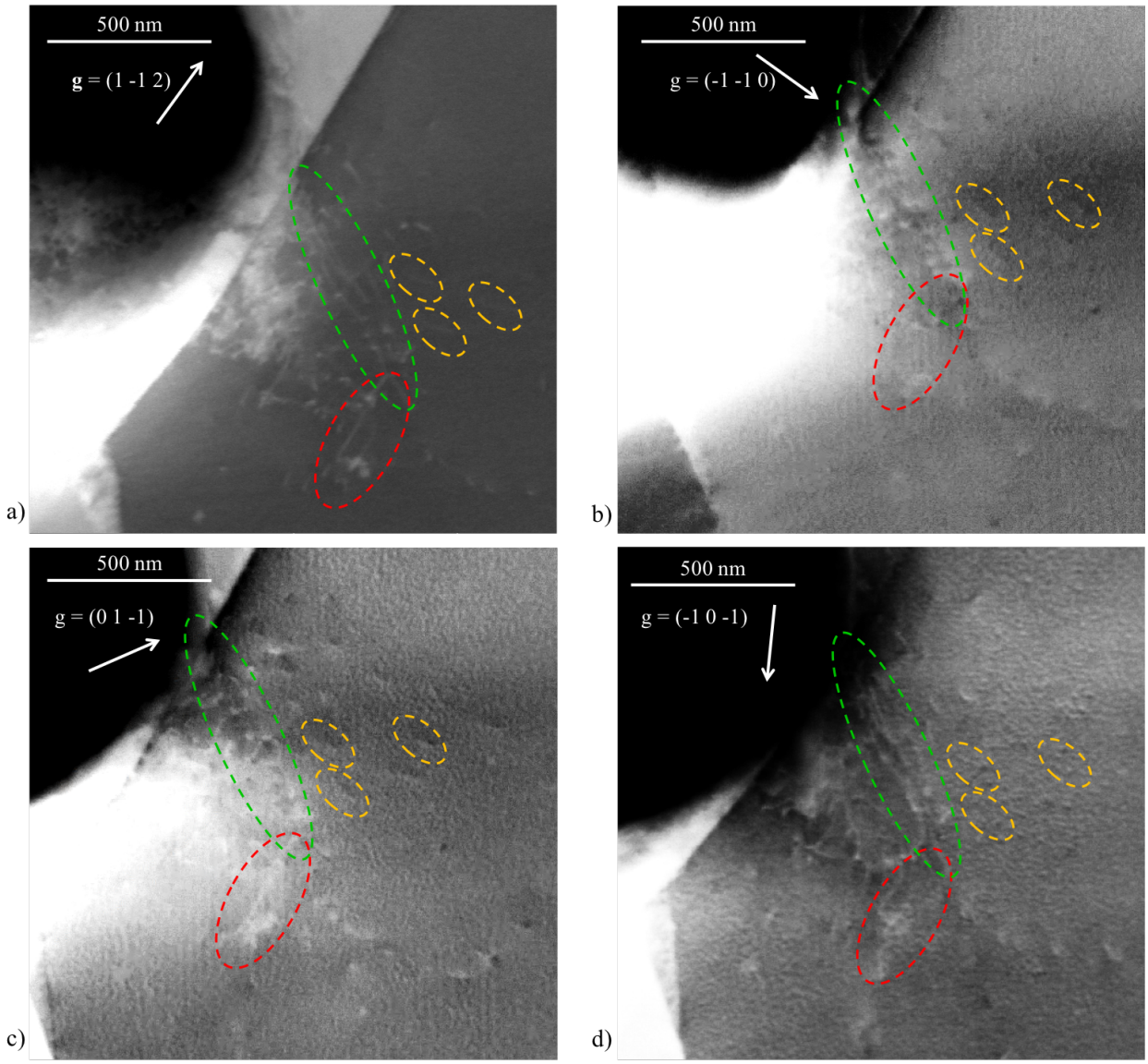

Figure 4.14: ECC images used to characterize three distinct sets of dislocations generated on the opposite side of a grain boundary. The four channeling conditions used are in shown in a) to d).

It is important to note that the plane normal is approximately [-111] and all the channeling conditions used intersect the [-111] zone axis. Therefore, edge dislocations with a [-111] Burgers vector (which would have line direction parallel to the sample surface) will always be in an invisibility condition. On the other hand, screw dislocations of the [-111] Burgers vector would always be visible due to surface relaxation due the line directions being perpendicular to the sample surface. For these reasons, the sets of dislocation outlined are not expected to have a Burgers vector of [-111]

The dislocations outlined in red become invisible at the channeling condition of **g** = (-1-10), indicating a Burgers vector of [1-11]. The dislocations outlined in green become invisible at the channeling condition of **g** = (01-1), indicating a Burgers vector of [111]. The dislocations outlined in orange become invisible at the channeling condition **g** = (-10-1), indicating a Burgers vector of [11-1]. By combining this $\mathbf{g} \bullet \mathbf{b} = 0$ analysis with an analysis of the line direction with respect to the grain orientation (shown in Figure 4.15), a sense of the dislocation types is obtained.

Figure 4.15a shows the stereographic projection of the grain orientation for the ECC image that is again shown in Figure 4.15b. The line directions of the three sets of dislocations are overlaid onto the stereographic projection with their respective colors. The line directions of each set of dislocations lies close to the Burgers vectors, indicating that these dislocations are predominately screw type.

It was attempted to characterize these dislocations using CC-EBSD but the scan quality was too low to resolve the GND density onto specific slip systems. Possible reasons for low quality will be discussed later.

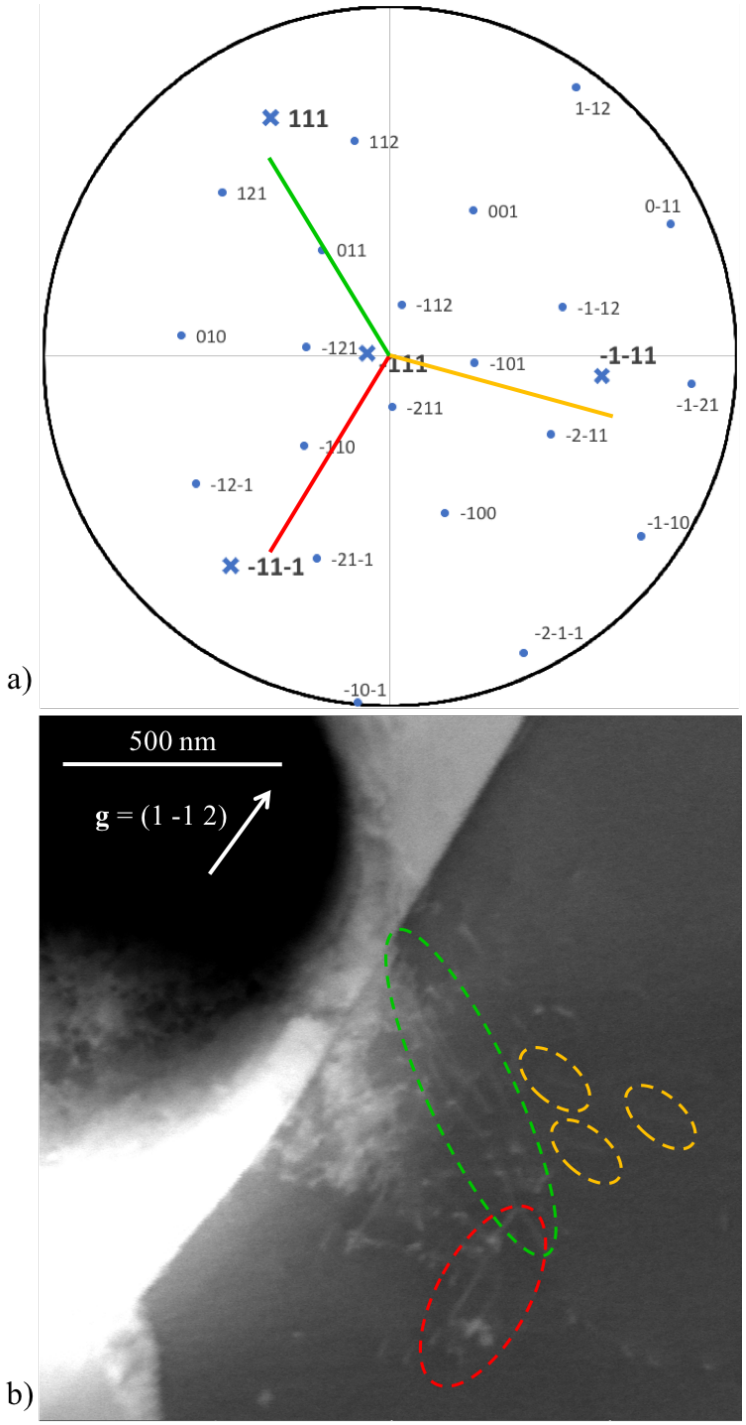

Figure 4.15: a) Stereographic projection that corresponds to the grain orientation of the ECC image in b). The line directions for the three sets of dislocations are overlaid on the stereographic projection with their respective colors.

4.5.3 Coarser CC-EBSD Over Four Nanoindents

To demonstrate the efficiency/effectiveness of CC-EBSD to map dislocation distributions, CC-EBSD was performed over a broader area. EBSD was carried out at a step size of 200 nm and the cross-correlation calculation was carried out with an effective step size of 200 nm. This is shown in Figure 4.16. Figure 4.16a is a BSE image of the four indents with a grain boundary running from the upper left of the image to the bottom right of the image. Three indents are near the grain boundary with two indents on the right and one on the left. The fourth far enough away from the grain boundary to be considered a single crystal indent. The top left indent is closer to the grain boundary than the bottom right indent. Below and to the left of the top left indent, the BSE images shows distortion of the grain boundary. The bottom right indent has the same effect on the grain boundary but not as much.

Figure 4.16b shows the corresponding CC-EBSD calculated GND map. It shows GND build up on the opposite side of the grain boundary as the top left and bottom right indents. This GND build up is in the same areas as that of the distortions at the grain boundaries of the BSE images and with the same relative amounts between the two indents. However, the GND density level is not much higher than the noise and can barely be seen at the grain boundary for the bottom right indent.

As done is the previous GND maps, pixels that correspond to an EBSD confidence index of less than 0.15 were whited-out. The grain boundary in the GND map is dotted with these white pixels.

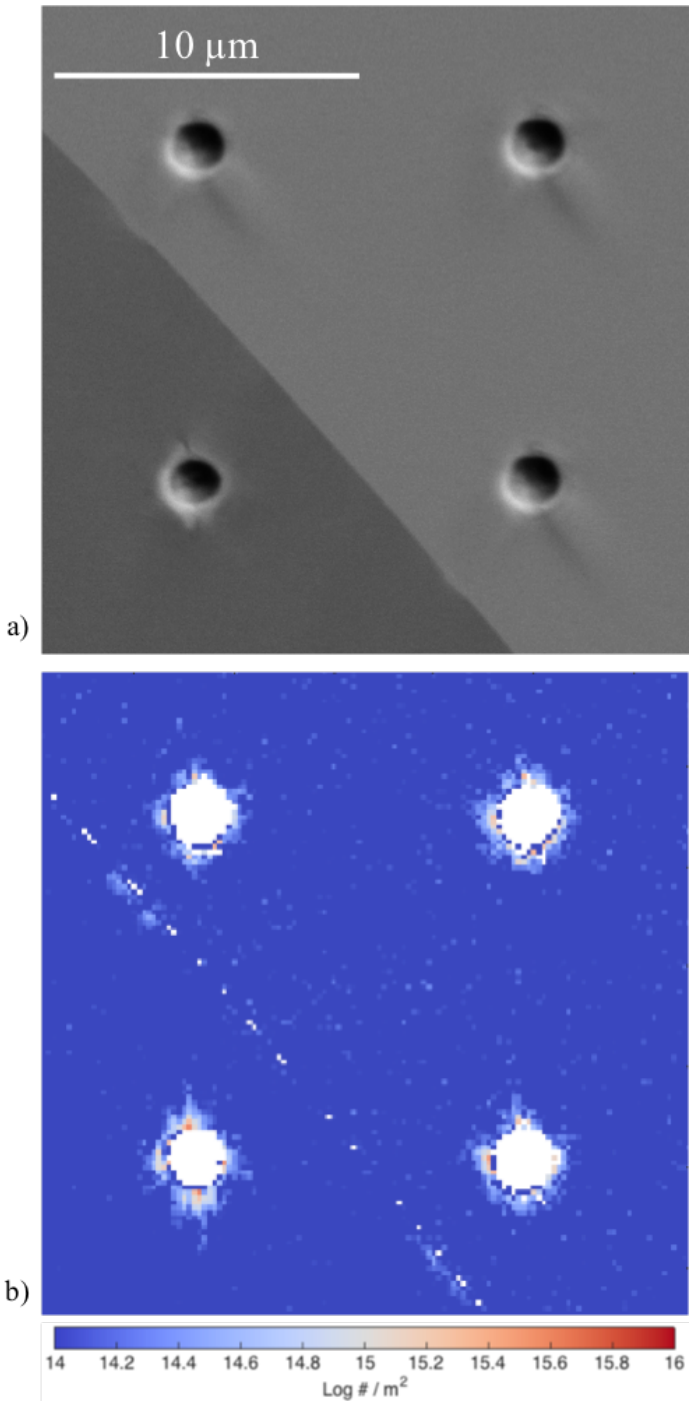

Figure 4.16: a) BSE image of four indents, three near a grain boundary and one far enough away from the grain boundary to be considered a single crystal indent. b) GND map of the same four indents.

4.6 Analysis of Wedge Indent Cross-Section

Figure 4.17a shows the CC-EBSD derived GND density map from Ruggle et al. [80] along with a BSE image, Figure 4.17b, of the area analyzed in this work. The channeling contrast in the BSE image shows thin bands that become pointed from the outside of the image towards the center in a downward direction. These bands are seen from left to right and from right to left, however, they are more faint from the right to left direction. If a line was drawn from the tip of the indent, it would go down the middle of the BSE image, where the bands from both sides intersect and the intersections form parallelogram shaped boxes/cells of dark contrast.

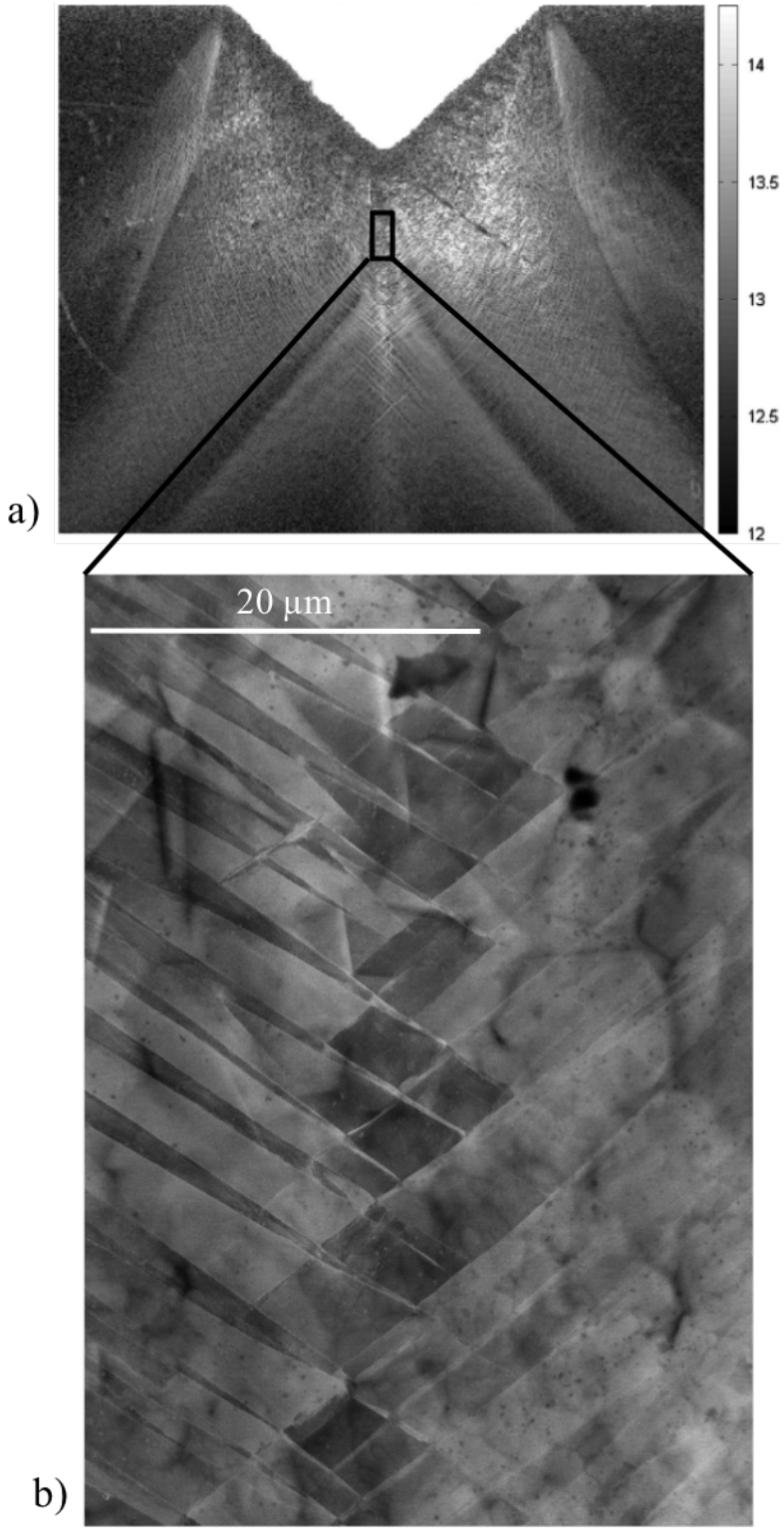

Figure 4.17: a) CC-EBSD derived GND map from Ruggles et al. [80] and b) a BSE image of the area analyzed in this work.

A magnified ECC image of one these boxes/cells reveals dislocations, shown in Figure 4.18b. Many of the dislocations seen in the middle box/cell are generally parallel to the sample surface. Contrast from dislocations can also be seen within the bands as well as the boxes/cells on the other sides of the thin bands. There is also significant contrast from a large number of dislocations on the boundaries between the boxes/cells and the bands.

The dislocations cannot be characterized using contrast analysis because the **g** vector could not be determined using SACPs. This is because the boxes/cells are too small to obtain SACPs. For other portions of this work, SACPs were only obtained for grains as small as 40 μm in diameter, but the box/cell in Figure 4.18b is only about 4 μm across.

Because screw dislocations have a lower mobility than edge dislocations in bcc Ta, it can be assumed that the majority of dislocations in the interior of the box/cell in Figure 4.18b are of the screw type. Therefore, the Burgers vectors of the dislocations that have line directions parallel to the sample surface can be determined using the stereographic projection, which was calculated from the data collected with EBSD. Figure 4.19a shows the line directions of the dislocations overlaid on the stereographic projection, revealing that these dislocations are likely [-11-1] screw dislocations.

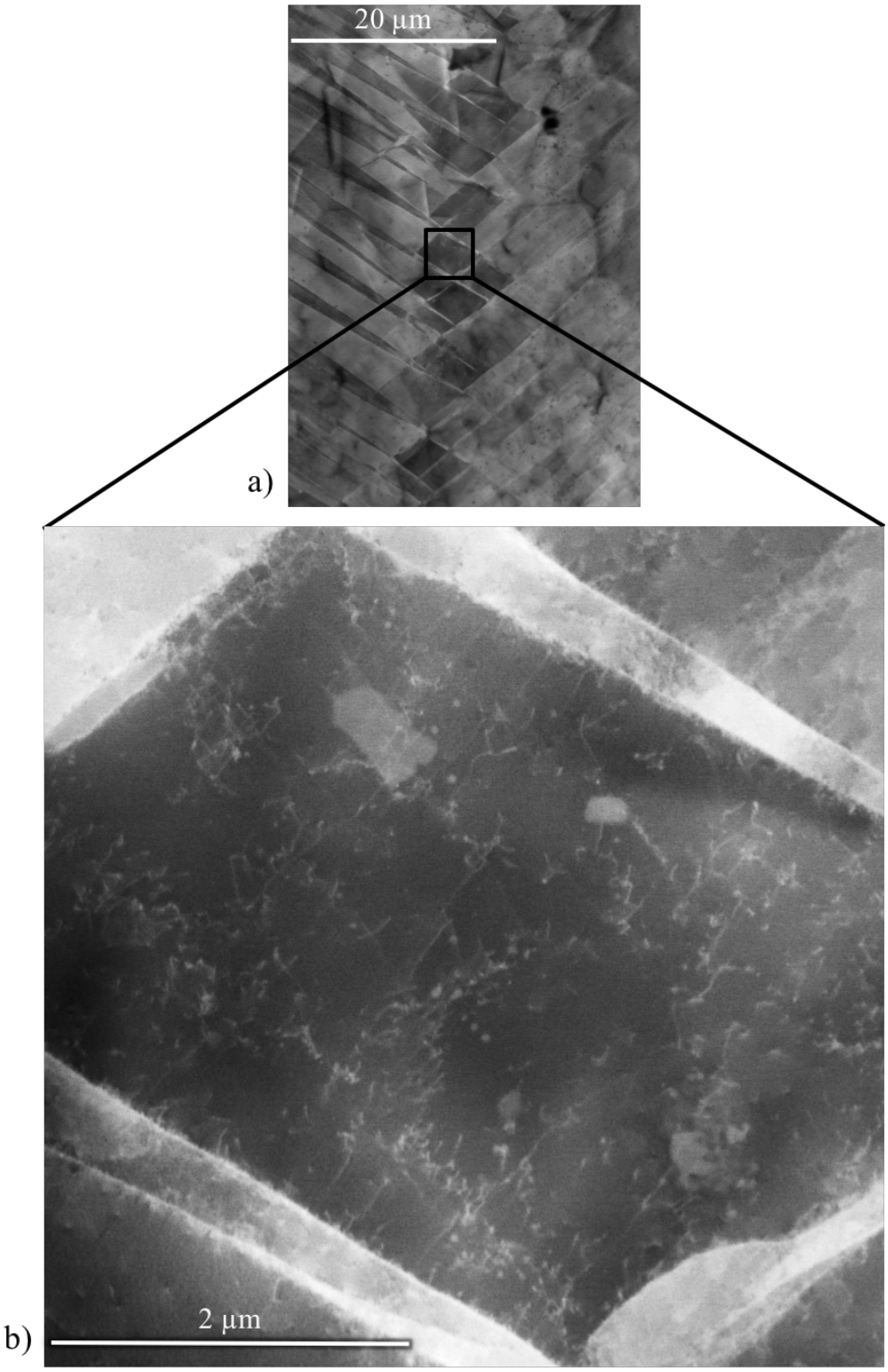

Figure 4.18: a) BSE image of the analyzed area and b) an ECC image of one of the boxes/cells formed by the intersection of the bands seen in the BSE image.

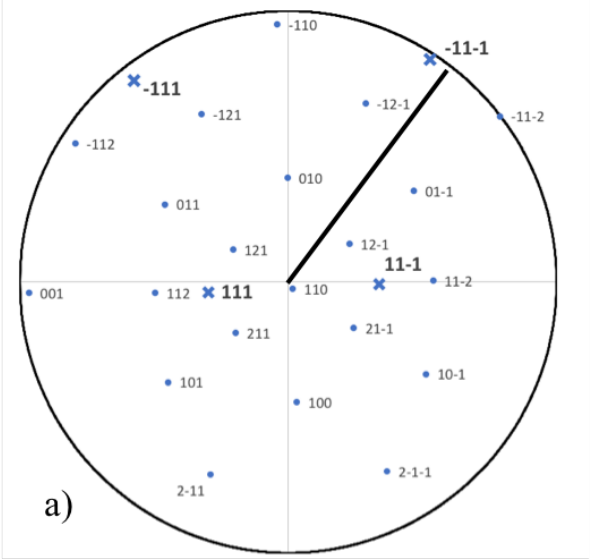

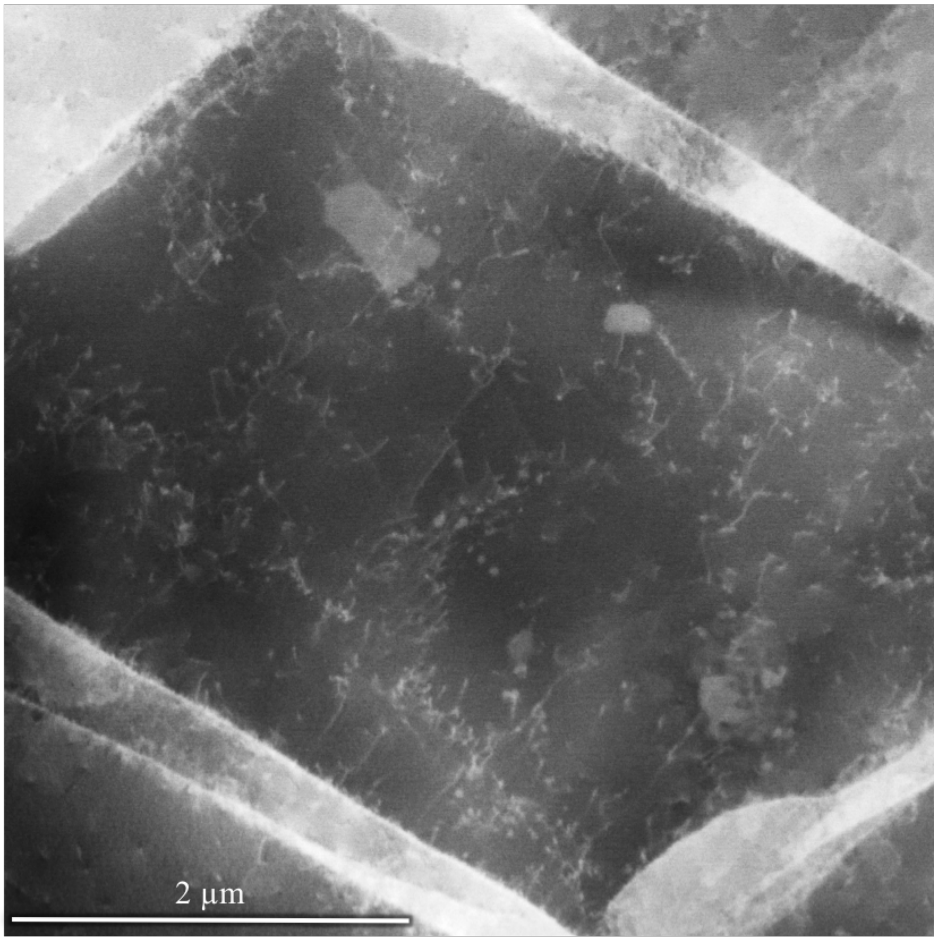

Figure 4.19: Many of the line directions in the ECC image, shown in b), have line directions that are generally parallel to the surface. Assuming that these dislocations are screw dislocations, overlaying the line directions onto the stereographic projection, shown in a), reveal that the Burgers vector for these dislocations are [-11-1]

EBSD was carried out with a 60 nm step size over the area of interest shown in Figure 4.17b and Figure 4.18a. The EBSD map is shown in Figure 4.20a with the points that had a confidence index lower than 0.15 being discarded. Due to the fact that this is plane strain in the surface plane (xy plane), all lattice rotation is around the surface normal. For this reason, the original inverse pole figure color of green (the color of the {101} plane normal for the inverse pole figure legend) will remain green for all lattice rotations. Therefore, strictly for visualization purposes, the crystal lattice for all EBSD points were rotated 90° about the x-axis in order to visualize the changing crystal orientation, shown in Figure 4.20b. In this view, the thin-pointed bands seen in the BSE image in Figure 4.17b and Figure 4.18a are pink and the original/bulk orientation is now red.

All the thick bands on both sides generally have the same orientation (the original bulk crystal orientation). The thin bands on the left rotate the crystal lattice an average of 10.2° counter clockwise (maximum being 17.7° and the minimum being 6.1°) and the thin bands on the right rotate the crystal clockwise an average of 7.2° (maximum being 11.8° and the minimum being 4.4°). This is further revealed in the pole figure maps shown in Figure 4.21. The left column of pole figures show the shifts caused by the thin bands on left side of the EBSD map cause, the middle column shows the shift caused by all thin bands, and the right column shows the shifts caused by the thin bands on the right side of the EBSD map. In all of the pole figures the shifts are seen as streaks. The differences between the shifts for the left thin bands and right thin bands is seen by the rotational shifts in the left and right columns of Figure 4.21. There are, however, minor effects of the right bands in the left band pole figures (and vice versa) because the bands cross and could not be completely separated out.

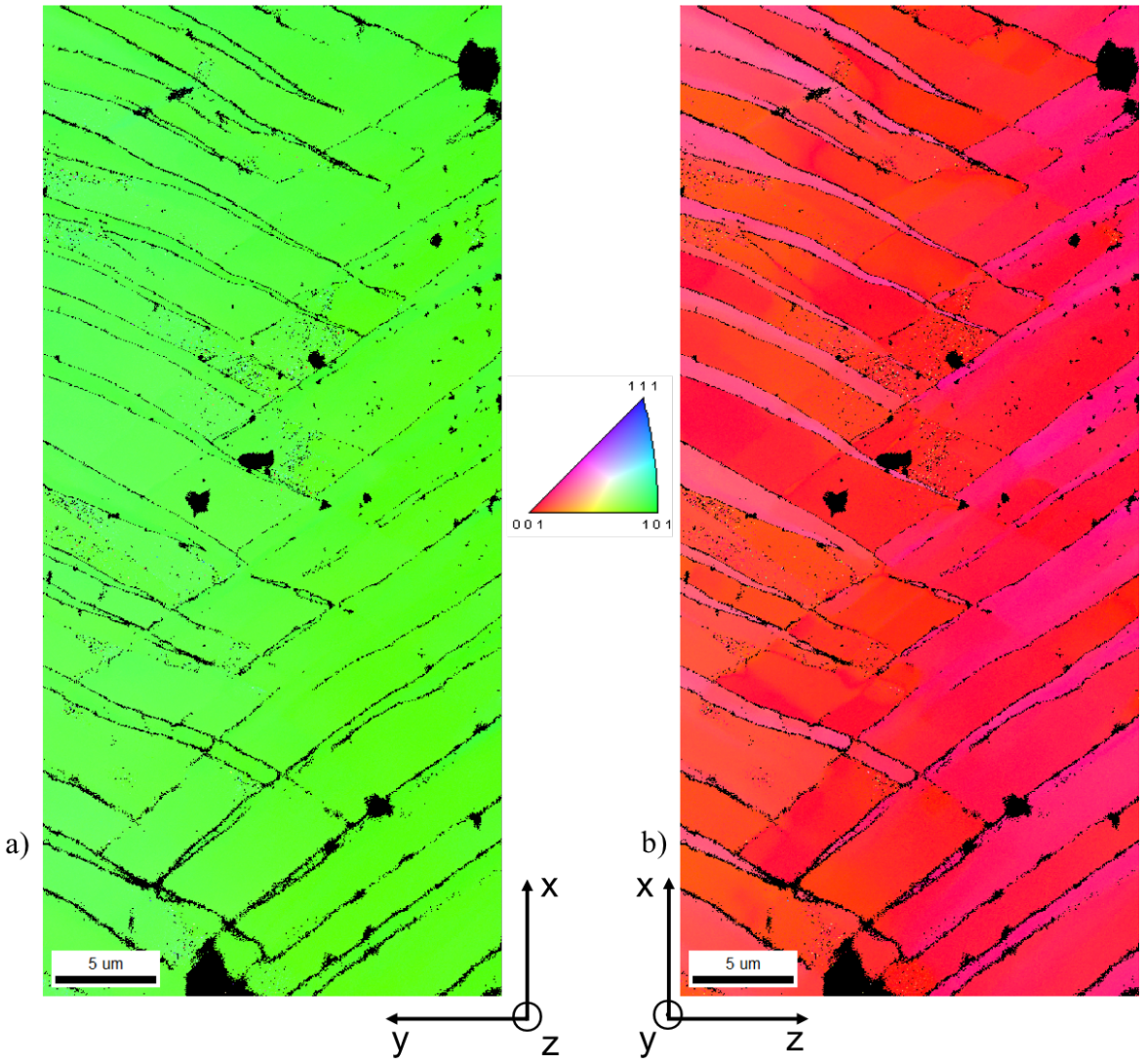

Figure 4.20: a) Inverse pole figure map for the revealing no change in lattice orientation due to the fact that all lattice rotation is around the surface normal. b) By rotating all crystal lattice points 90° around the x-axis, the orientation changes can be more readily discerned.

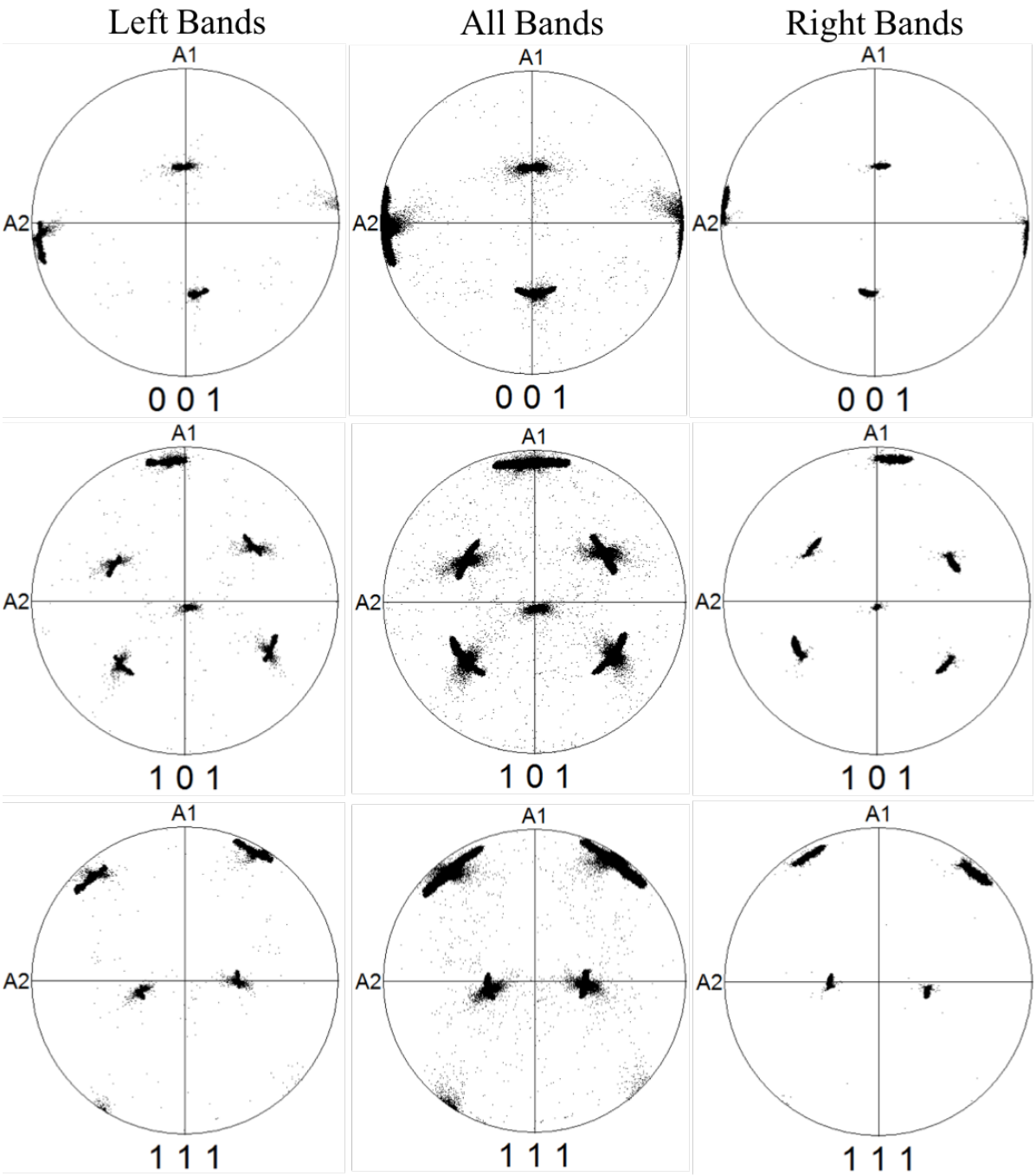

Figure 4.21: Left Column) Pole figures that represent the shift caused by the left thin bands, Middle Column) pole figures that represent shifts caused by all thin band shifts, and Right Column) are pole figures that represent the shifts caused by the right thin bands.

As the thick and thin bands are alternating, it can be seen that the orientations are alternating between the rotated and un-rotated version of the crystal lattice. This is shown in Figure 4.22. It is not a gradual rotation across the thick and thin bands, but rather immediate shifts in either side of the boundary. The thin bands on the left rotate the original orientation counter clockwise, while the thin bands on the right rotate the original orientation clockwise. The rotations on the right side are smaller and therefore less clear. The alternating rotations are consistent with the alternating contrast of the bands observed in Figure 4.17b.

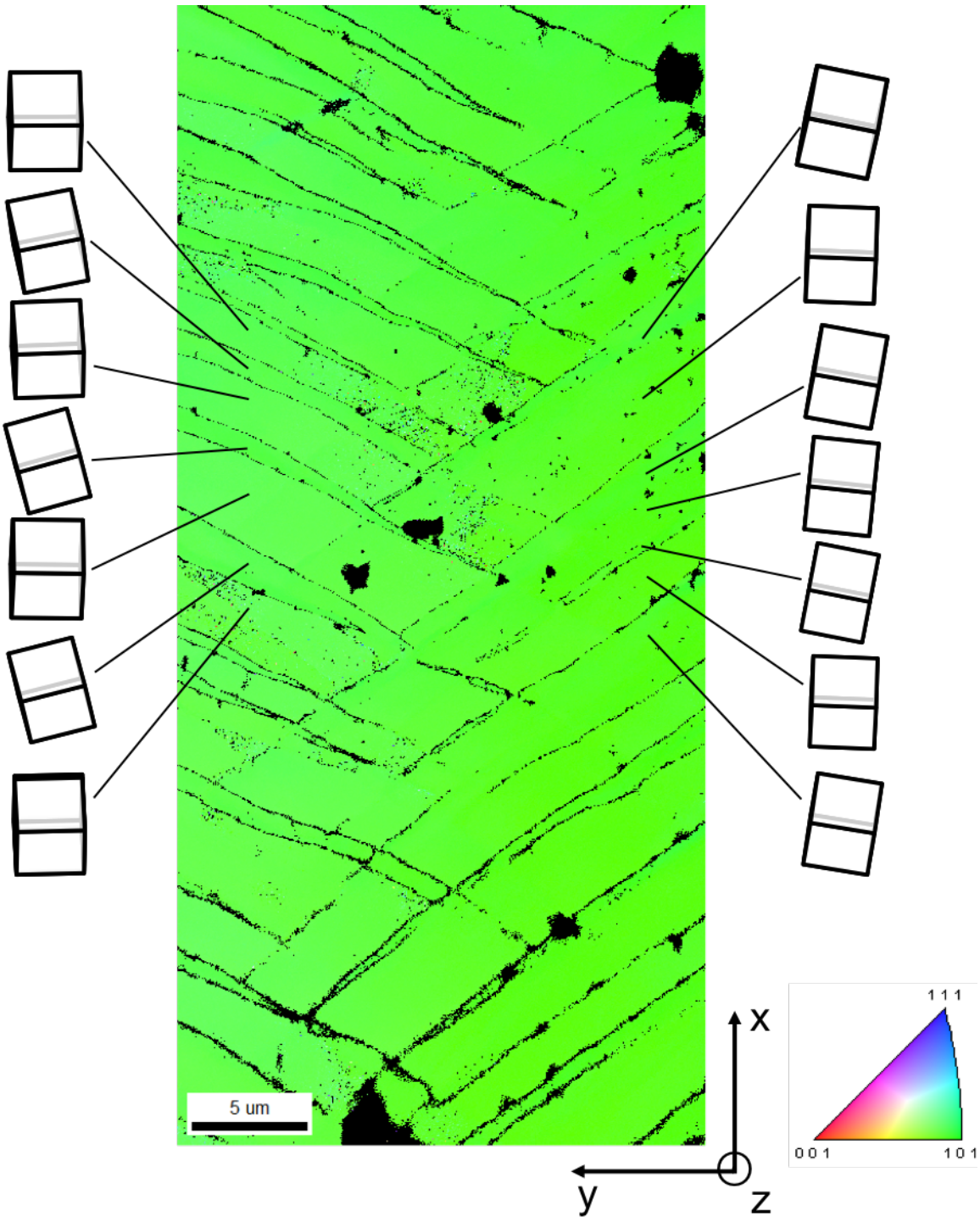

Figure 4.22: Inverse pole figure EBSD map overlaid with the unit cells for the alternating bands.

5 Discussion

5.1 Single Crystal Microindentation and Nanoindentation

Both microindentation and nanoindenation in single crystals show that indentation topography is a function of crystal orientation. There is, however, a size effect between microindentation and nanoindentation, which is seen in the indentation of crystals with a surface normal of the <101> type. While nanoindentation shows what appears to be one long topographical lobe on either side of the indent, microindenation shows two lobes on either side of the indent. By looking at the stereographic projection of a <101> type orientation, it is seen that there are three <111> directions pointing out from either side of the indent. Two of the directions, [1-11] and [-1-11], lie in the surface plane of the sample (contributing two <111> directions on either side of the indent) and two of the directions, [111] and [-111], are inclined at about 35° (contributing one <111> direction on either side of the indent), shown in Figure 5.1b. As noted earlier, the lobes generally line up with the <111> directions, therefore, one would expect to see three topographical lobes on either side of the indent. This is observed best in the AFM map shown in Figure 5.1a and the corresponding stereographic projection in Figure 5.1b. Because the three lobes are close together, they can appear as a single lobe.

Contrasting with nanoindentation, microindentation shows two lobes on either side of the indent. This is likely due to the changing stress state imposed by the indenter tip. While nanoindentation and microindentation used the same size tip radius of 1 μm, nanoindentation general stays in the spherical portion of the nanoindenter and the deformation induced by microindentation is dominated by the conical portion. This suggests the slip that is activated by the spherical portion of the indenter, which causes the middle lobe in nanoindentation, is suppressed by the stress state of the conical portion of the indenter in microindentation.

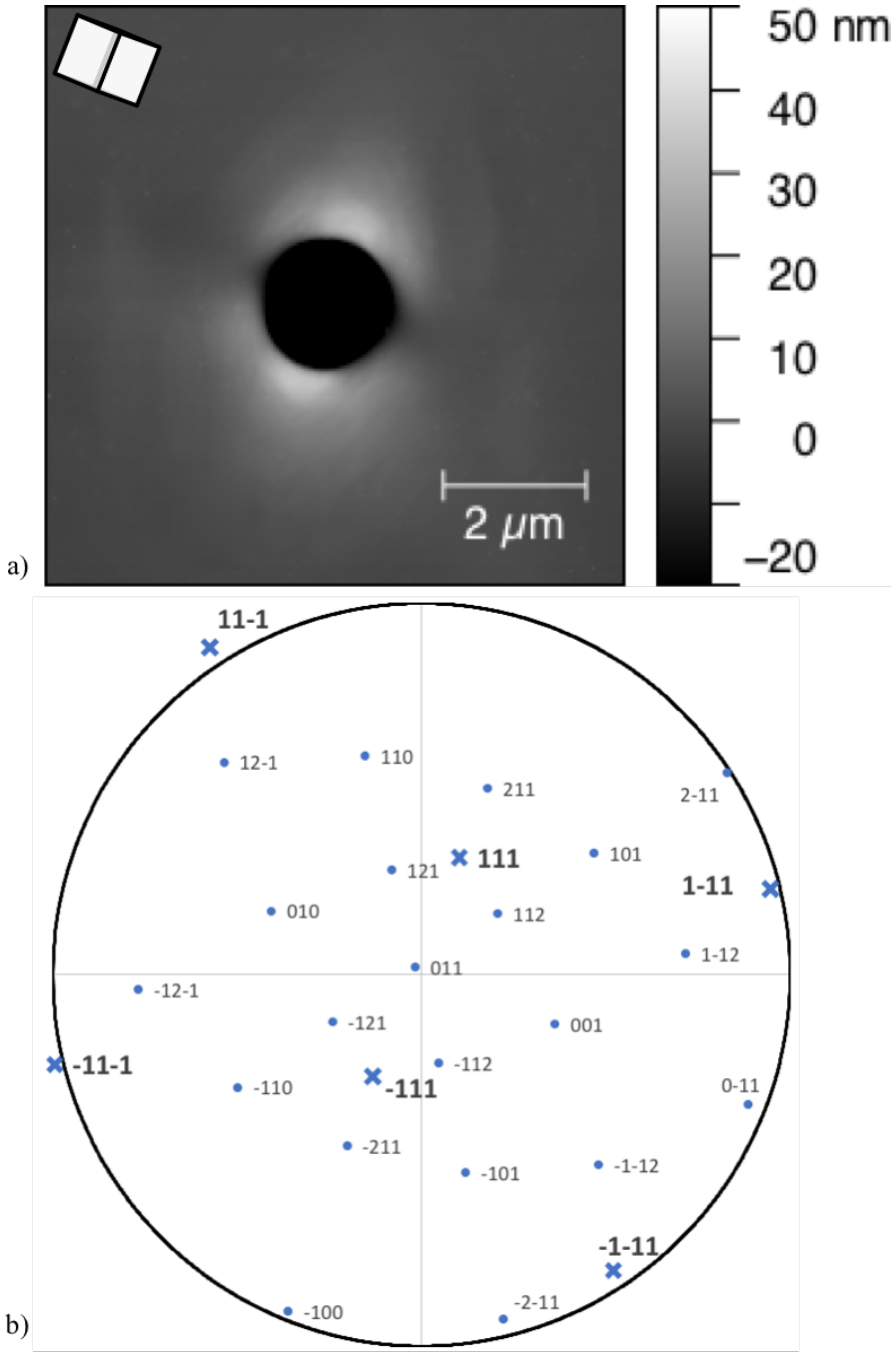

Figure 5.1: a) AFM measurement a single crystal nanoindent in a grain of [011] orientation. b) Stereographic projection of the same grain showing two Burgers vectors lying in the surface plane of the sample and two Burgers vectors pointing to either side of the indent.

For microindentation, the lobes of the <100> type indents have the highest average maximum height, followed by <101> and the <111>. For nanoindentation, the lobes of the <100> type also have the highest average maximum height but the <101> and <111> types are statistically equivalent. In other words, it seems that as indentation continues, the <101> type has a greater relative increase in the average maximum height than the <111> type. This could be due to the fact that for nanoindentation, the slip activity is pushing lobes out in six directions but once the microindentation scale is reached, all the slip activity is pushing lobes out in only four of the original six directions, increasing the relative slip activity of the lobes in comparison to the <111> type.

5.1.1 CPFEM of Single Crystal Nanoindentation

The comparison of CPFEM to experimental nanoindentation shows the best match for [001] oriented grain and the worst match for the [111] oriented grain. Even though the [001] orientation has the best match, there is a difference in lobe height and lobe spread for this orientation. Furthermore, there is a complete difference in symmetry for the [111] orientation. These two major differences suggest that the structure evolution parameters need to be optimized for Ta and the non-Schmid effects need to be correctly implemented into the phenomenological model.

5.2 Grain Boundary Nanoindentation

AFM measurements of grain boundary nanoindents in section 4.3 show that there is significant topography transfer from one side of the grain boundary and not from the other, indicating the directionality influence of dislocation flow. For indents where there is significant transfer, i.e. indents 3, 11, and 15 from Figure 4.3, the deformation in the neighboring grain

follows the symmetry/orientation of the crystal. This is seen by the lack of significant topography of the neighboring grain in the topography subtraction result.

The directionality dependence of deformation transfer indicates that a single *m'* value for a given grain boundary is inadequate for describing whether a grain boundary is susceptible to, or at which level it is able to accommodate deformation transfer. Rather, *m'* should be dependent on the activated slip systems in the parent grain. Even further, the resistance to deformation at the grain boundary may depend on the side of the grain boundary from which deformation is approaching. In other words, a given crystal orientation may be able to transmit deformation to a neighboring grain, but is less prone to accommodate deformation coming across the grain boundary. This is be directly related to the anisotropy of the crystal in that some crystals are in a "hard", or less accommodating to deformation, orientation and some crystals are in a "soft", or more accommodating to deformation, orientation.

From Figure 4.3, resistance to topography transfer across the grain boundary is shown by positive (red) topography in the parent grain of the subtractions results (i.e. more red topography indicates more resistance). With this, it is seen that the amount of topography transfer resistance at a grain boundary is not synonymous with whether or not there is topography transfer. For example, indents 3, 15, and 11 show significant topography transfer across the grain boundary, however, while indents 3 and 15 show significant resistance, indent 11 shows little to no resistance. In a similar regard, indents 4, 12, and 14 all show no topography transfer, however, while indent 4 shows significant resistance, indents 12 and 14 show little to no resistance.

In summary, these six indents made along the three grain boundaries illustrate four combinations of topography transfer and resistance at the grain boundary. Those combinations include: (1) significant transfer and significant resistance (indents 3 and 15), (2) significant

transfer and little to no resistance (indent 11), (3) little to no transfer and significant resistance (indent 4), or (4) little to no transfer and little to no resistance (indents 12 and 14).

The combination of little to no transfer and little to no resistance likely means that due to the crystal orientation, the deformation from nanoindentation is not heavily directed towards the grain boundary. On the other hand, the combination of little to no transfer and significant resistance suggests deformation is directed at the grain boundary and possibly the dislocations are being reflected back from the grain boundary or slip systems transferring deformation towards the boundary lock up to cause an increased activation of other slip systems.

The combination of significant transfer and significant resistance suggests that dislocations are reflected back from the boundary or slip systems lock up to cause an increased activation of other slip systems but eventually the stress at the grain boundary is high enough to activate the slip systems in the neighboring grain. The combination for significant transfer and little resistance suggests that deformation directed at the grain boundary and the neighboring grain is in an orientation the can easily accommodate deformation.

5.2.1 Dislocation Pile-ups at Grain Boundaries

In general, deformation at grain boundaries is thought of as dislocations piling up at the grain boundary and after certain amount of stress develops, dislocations are generated on the other side of the grain boundary [6, 7, 15, 19, 39, 40]. Contrasting, CC-EBSD and ECCI measurements shown in Figure 4.13 show a build-up of dislocations in the neighboring grain rather than a dislocation pile-up in the originating grain. But the indent is quite close to the grain boundary not allowing for any dislocation pile-up to be viewed within the parent grain. This concern is addressed, however, with the grain boundary indents in Figure 4.16. Here the CC-EBSD shows no dislocation build-up in the parent grain but shows dislocation build-up

immediately on the other side of the grain boundary. This indicates that dislocations readily leave the parent grain but dislocation propagation into the neighboring grain is restricted.

One possibility for the lack of dislocations at the grain boundary in the parent grain is the dislocations coming from the indent are edge dislocations and because of their high mobility they exit the grain quickly going in the neighboring grain. The dislocations propagating into the neighboring grain could be screw dislocations, which have a low mobility, restricting their propagation into the neighboring grain. This could be the case for the grain boundary indent in Figure 4.13 as the dislocations were identified to be screw dislocations. The second possibility is that deformation from nanoindentation is so localized that the motion of dislocations does not reach very far beyond the grain boundary.

Regardless of the reasons for dislocation build-up on either side of the grain boundary, this work illustrates that ECCI and CC-EBSD combined with nanoindentation is a good method for investigating dislocation build-up at grain boundaries. One of the biggest advantages of nanoindentation is that the originating and neighboring grains are easily identified in relation to deformation. With experiments such as tensile tests, however, it is not always intuitive which grain is the originating and which grain is the neighboring grain to deformation. Assuming that the dislocation pile-up occurs in the originating grain can be incorrect assumption according to the results in Figure 4.13 and Figure 4.16.

5.2.2 CPFEM of Grain Boundary Nanoindentation

As mentioned earlier, the CPFEM topography results show that grain boundaries have an effect on topography, but they disagree with the experimental results in that the CPFEM suggests all grain boundaries exhibit strain transfer and CPFEM overestimates the topography height (only indent 3 and 4 are close to the experimental result). Su et al. [42] also showed that the

CPFEM overestimated topography transfer for α-Ti, but to a lesser degree than in this work. Overall, just as the single crystal CPFEM results suggest, the structure evolution parameters need to be optimized for Ta and the non-Schmid effects need to be correctly implemented into the phenomenological model in order to achieve a better analysis between experimental and CPFEM nanoindenation.

5.3 ECCI vs. CC-EBSD

5.3.1 Dislocation Density Comparison

Qualitatively, there is good agreement between areas of high dislocations density of the CC-EBSD GND results and the locations of individual dislocations measured from ECCI. Nevertheless, as shown in Figure 4.7, ECCI has superior spatial resolution, which allows for individual dislocations to be detected within a single grid square while data from CC-EBSD is more diffuse and noisy. The diffusivity and noise from CC-EBSD is due to the fact that a dislocation is treated as a continuum based on the strain field in the lattice, causing the limited resolution of CC-EBSD to be controlled by the original step size at which the EBSD data was acquired and the effective step size at which the GND map was calculated. While ECCI has advantages for identifying individual dislocations at low densities, CC-EBSD is advantageous because it is able to detect large lattice rotations and observe dislocation strain effects in high deformation regions that are too densely packed for ECCI, i.e. around the rim of the indent.

To obtain a more robust quantitative comparison of the measurements presented in Figure 4.7, dislocation densities measured via ECCI and CC-EBSD were averaged for five separate regions, shown in Figure 5.2. In regions 1, 2, and 3, ECCI and CC-EBSD both detected dislocations, in region 4 only ECCI observed distinct dislocations, and in region 5 no dislocations were observed using ECCI. For each of these five regions, an average GND density

from CC-EBSD was determined by averaging the GND density associated with each pixel in the region. Dislocation densities from ECCI were determined by counting the number of dislocation intersections with the surface.

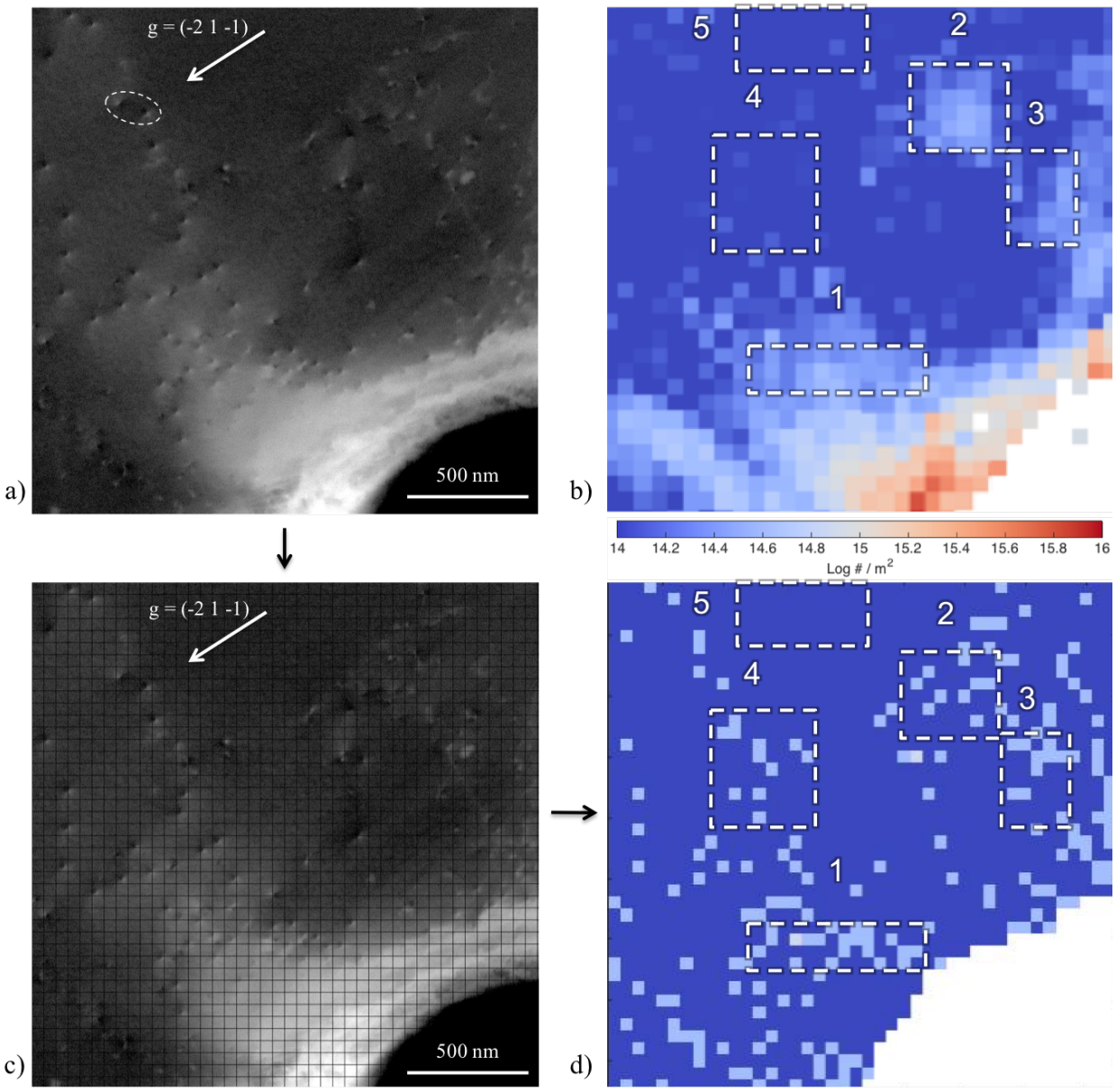

Figure 5.2: Duplicate of Figure 4.7 overlaid with 5 regions for comparison between b) CC-EBSD calculated GND density map and d) a dislocation density map that was derived from the ECC image in a) and c). The oval in a) shows an example of dipole dislocations.

Dislocations were initially assumed to have line directions perpendicular to the surface, but if dislocations are not normal to the counting area, dislocation densities are underestimated [100]. To obtain corrected densities, the dislocation density should be multiplied by $1/\cos(\theta)$, where θ is the angle between the line direction and the beam axis. Most of the dislocations in regions 1 and 4 were identified as [111] screw dislocations with a line direction 40° to the beam axis when the sample was in the channeling condition for the ECC image in Figure 5.2a and c. The dislocations in regions 2 and 3 were not identified and are not all the same dislocation type but many of these dislocations are likewise inclined. Since all line directions are possible in these two regions, an average angle of 58° has been used for calculating the dislocation density. This was calculated by averaging the angles that the 22 possible line directions (12 for {110} slip plane systems, 6 for {112} slip plane systems, and 4 for screw dislocations) make with the beam axis. For all five regions, Table 5.1 presents both the initial and line direction corrected dislocation densities.

Table 5.1: Comparison of CC-EBSD GND densities and ECCI dislocation densities for the 5 regions shown in Figure 5.2.

Region #	CC-EBSD GND Density	ECCI Density	ECCI (Line Direction Correction)	ECCI (Dipole Correction)
1	2.6×10^{14} m^{-2}	1.6×10^{14} m^{-2}	2.1×10^{14} m^{-2}	1.9×10^{14} m^{-2}
2	2.1×10^{14} m^{-2}	8.6×10^{13} m^{-2}	1.6×10^{14} m^{-2}	No dipoles
3	1.7×10^{14} m^{-2}	1.1×10^{14} m^{-2}	2.2×10^{14} m^{-2}	No dipoles
4	6.4×10^{13} m^{-2}	6.1×10^{13} m^{-2}	8.0×10^{13} m^{-2}	No dipoles
5	5.2×10^{13} m^{-2}	0	0	0

Due to the spatial resolution limitations of CC-EBSD as compared to ECCI, it is possible that dipole dislocation pairs will fall within a given CC-EBSD step, canceling the contribution to the dislocation density, i.e. on the local scale ECCI may resolve dipoles while CC-EBSD may not. A few dipole pairs are observed in the ECC images, for example in the small oval in Figure 5.2a. ECCI shows 22 dislocations in region 1 with one dislocation displaying reversed contrast (i.e. opposite Burgers vectors). From the CC-EBSD perspective this dislocation will cancel out with another closely spaced dislocation and neither will be accounted for, leaving a net 20 dislocations in the CC-EBSD determined dislocation density. This effect is accounted for in the Dipole Correction Column in Table 5.1. Dipoles were observed in region 1, but not observed in regions 2 through 5.

The total dislocation density is made up of both GNDs and SSDs. Thus, as ECCI images reveal both the GNDs and SSDs, one would expect that the ECCI measured density would be greater than or equal to that determined by CC-EBSD. However, the results presented here do not reflect this for regions 1 and 2. This may indicate that the comparison here is being carried out in regions where the CC-EBSD GND density measurements are close to their noise floor. Indeed, region 5 is an area where no dislocations were observed using ECCI, but the CC-EBSD indicated a GND density average of 5×10^{13} m^{-2}. This noise floor is near the CC-EBSD GND density noise range suggested by the work of Jiang et al. [101] in which they measured the GND density noise on single crystal Si. This noise is likely due to binning/resolution of the EBSD camera [101] , pattern quality due to EBSD scan rate [102] , and the EBSD step size/effective step size [95, 103]. Errors may also be associated with increased diffusiveness of the EBSD patterns taken from areas with a higher density of dislocations, but it would be expected that this error would be averaged out over a number of EBSD steps. Nevertheless, if the noise level

indicated by region 5 outlines an uncertainty level that is then applied to the measurements in the other regions, the CC-EBSD and ECCI measurements appear quite close.

ECCI could also result in lower measured dislocation densities simply because some dislocations may be in a zero contrast condition for the particular 2-beam channeling condition used, i.e. $\mathbf{g} \bullet \mathbf{b} = 0$ and/or $\mathbf{g} \bullet \mathbf{b} \times \mathbf{u} = 0$. In this work, however, this was not the case as this effect was accounted for by taking images at multiple channeling conditions and other dislocations do not appear. CC-EBSD will never have dislocations that are "missed" due to this effect and will be able to identify all of the dislocations that contribute to the GNDs.

Another potential limitation of ECCI is that at higher dislocation densities it becomes impossible to resolve the individual dislocations. This appears to be the case for the regions close to the indent that appear very bright. CC-EBSD does in fact identify higher dislocation density pixels in this near-indent region that appear only bright in ECCI. Overall, both CC-EBSD and ECCI have some inherent limitations to determining dislocation densities, and users should be aware of these restrictions when using these techniques.

5.3.2 Dislocation Characterization Using ECCI

All the dislocations characterized in this work were identified to be screw dislocations. Considering that edge dislocations have a higher mobility than screw dislocations, it is reasonable to conclude that at the stage of deformation where these analyses were carried out, the edge dislocations have exited the crystal leaving predominately screw dislocations, i.e. as deformation continues the concentration of screw dislocations will likely increase because as more dislocation loops are generated, the edge components will exit the crystal quickly leaving behind the screw components.

5.3.3 Dislocation Characterization Using CC-EBSD

A few caveats apply when employing the Nye-Kröner method at the limits of its spatial and dislocation density resolution (i.e. when there are countably few dislocations per area resolution). First, all dislocation content is assumed to be a linear superposition of pure edge or pure screw dislocations [88]. This means that dislocations of mixed character will be represented by superimposed fields. Additionally, at these low step sizes, noise effects are more dominant [95]. One caveat often mentioned [80, 88, 95, 97] when interpreting dislocation density fields measured via CC-EBSD is not particularly cogent at the extremes of its resolution: the Nye-Kröner method only detects geometrically necessary dislocations. Because the length scale of the scan approaches that of dislocation dipole spacing, virtually all of the dislocations in the scan area may be thought of as geometrically necessary. Despite the challenges of employing CC-EBSD dislocation characterization at a resolution suitable for comparison at the same length scale, the level of agreement for single crystal indent in section 4.4.3 is strong.

The noise effects for the grain boundary indent in section 4.5.2 were too prevalent to resolve dislocations onto specific slip systems. It is possible that this crystal orientation and/or the orientation of the dislocation type causes the noise effects to be too prevalent since the Nye tensor determination is sensitive to orientation [80]. It can be seen in Figure 4.16b that noise of the GND calculations is affected by crystal orientation. In the top right grain there is more noise than in the bottom left grain. This is indicated by higher concentration of light blue pixels scattered throughout the upper right grain than the lower left grain.

5.3.4 A Balance of CC-EBSD Noise to SEM Drift

Mentioned earlier, the three main causes of noise for CC-EBSD is binning/resolution of the EBSD camera [101] , pattern quality due to EBSD scan rate [102] , and the EBSD step size/effective step size [95, 103]. For this work, the EBSD camera had a pixel resolution for 480 x 480 and no binning was employed, therefore, noise due to camera resolution cannot be reduced. Noise related to step size could not be reduced because this work sought to have a step size small enough as to not skip dipole dislocations. That leaves pattern quality as the main source for noise reduction. Other than exceptional sample preparation, good pattern quality is primarily achieved by increasing the exposure time of the camera or increasing the beam current. However, increasing the beam current will increase the spot size which will increase the interaction volume of the beam. In this work it was desired to maintain the spatial resolution, therefore the beam current was not increased.

The exposure time used in this work to achieve EBSD patterns was 0.1 s. While not all researchers state what exposure was used to collect EBSD patterns, some report 1 s or more [102, 104]. Britton et al. [102] achieved the best pixel intensity resolution, 0.02 pixels, with an exposure time of 5 s. In comparison, the exposure time used here is extremely fast. However, due to drift inside the SEM, 0.1 s was the longest exposure time that could be used as to not have distortions in the EBSD map.

Drift inside an SEM can be caused by a number of factors. A few possibilities include mechanical stage drift from a worn-out stage, beam drift due to a poorly grounded sample or stage, beam drift from charging particles inside the column, and other problems that can be related to the electromagnetic lenses or column of the beam. Mechanical stage drift is usually enlarged by tilting to 70° for EBSD because the weight of the stage will cause to it move down

in the direction of the tilt. Beam drift is also enhanced for EBSD in the directional component that is perpendicular to the beam and rotational axis for the 70° tilt. For example, a beam shift of 1 μm shift on a flat surface would obviously be 1 μm. But due to the geometry of EBSD this would cause a shift of 1.58 μm, from an EBSD perspective.

5.3.5 Advantages/Disadvantages of ECCI

ECCI is advantageous because it allows for the direct imaging of defects. In contrast to CC-EBSD, it able to resolve individual defects and quantify low dislocation densities. By taking images at multiple channeling conditions, defects can be characterized using $\mathbf{g} \bullet \mathbf{b} = 0$ and/or $\mathbf{g} \bullet \mathbf{b} \times \mathbf{u} = 0$ analysis.

On the other hand, taking images at multiple channeling conditions to characterize the defects however, can be time consuming. Yet, even if characterization is not desired and only dislocation density is wanted, ECCI still may not reveal all dislocations in a single image, still requiring multiple images. Another disadvantage of ECCI technique is that it is difficult to quantify high dislocation densities because individual dislocations are difficult to resolve at high densities. Also, few microscopes have a rocking beam function to allow for the collection of SACPs which would make characterizing defects difficult.

5.3.6 Advantages/Disadvantages of CC-EBSD

In comparison to ECCI, CC-EBSD is much faster due to the fact that much of the data collection and analysis is automated. This can allow for scans of large areas where it would not be plausible to use ECCI because ECCI would require many high magnification images to cover the same area. CC-EBSD can also quantify areas of high dislocation density that cannot be resolved with ECCI.

However, the ability of CC-EBSD to accurately quantify the density is related to the noise, which can come from binning/resolution of the EBSD camera [101] , pattern quality due to EBSD scan rate [102] , and the EBSD step size/effective step size [95, 103]. Using pattern quality to overcome noise has to be balanced with the possibility of sample/beam drift. But the main disadvantage of CC-EBSD relates to its inability to image/characterize individual defects. For example, it is likely to miss closely spaced dislocation dipoles (ie. GNDs vs. SSDs). Also, the noise may limit its ability to quantify low dislocation densities.

A less thought of disadvantage of CC-EBSD is that saving patterns can generate a lot of data. This would require research facilities where CC-EBSD is carried out regularly to maintain large data repositories. As an example of size, some EBSD scans used in this work collected 10,000 patterns. These patterns were 480 x 480 pixels and each image was saved as 16 bit TIFF file in order to maintain good intensity resolution of each pixel, making each image 461 KB. In total, the data size for a 10,000 image scan is 4.61 GB. But using an EBSD camera with 1000 x 1000 pixels, 10,000 images would take up 20 GB. With an exposure time of 0.1 s that was used in this work, it only took 16.7 minutes to generate this much data. Extrapolating this for a research facility that does CC-EBSD scans regularly, it would only take about 14 hours of scan data to use up an entire 1 TB hard-drive!

5.4 ECCI/CC-EBSD Compared to AFM

ECCI, CC-EBSD, and AFM measurements all reflect the symmetry of the crystal that nanoindentation was performed in, but the AFM topography measurements do not identify the locations of dislocations. Dislocations may or may not appear in the topographical lobes and they also appear where there are not any topographical lobes. To that point, it is important to realize that while topography that appears on the opposite side of a grain boundary from

nanoindentation is indicative of deformation transfer, the lack of topography does not mean there is a lack of deformation transfer. This is seen in the data from Figure 4.12 and Figure 4.13. The AFM map in Figure 4.12b shows that the majority of topography that is across the grain boundary is to the right of the indent, in an area where this is not a concentration of dislocations. The concentration of dislocations, seen in Figure 4.13a, appears at the lower right of the indent across the grain boundary in an area where there is not much topography.

The fact that topography across the grain boundary does not have an exact correlation with deformation transfer brings up two points. First, AFM only detects slip that has components that are out of the sample surface plane. Any deformation that occurs parallel to the surface plane may not be seen with AFM. The topographical lobes are made from many slip steps that are formed from dislocations exiting the sample surface [33]. This leads to the second point, that topography is evidence of dislocations that have already exited the crystal and ECCI/CC-EBSD assess the dislocations that are still in the crystal. Therefore, both techniques of AFM and ECCI/CC-EBSD should be used to seek an understanding of the past and current deformation processes taking place in a material.

5.5 Analysis of Wedge Indent Cross-Section

The dislocations generated under the wedge indent cannot be characterized due to the inability to obtain quantitative channeling patterns from the small areas. Assuming most are screw dislocations, however, some are able to be characterized using the data from EBSD to form a stereographic projection.

Regardless of how many dislocations can be characterized, the amount of GNDs versus SSDs can be reasoned from the EBSD. Due to the fact that the bands keep alternating between the same two general lattice orientations, overall there is no net lattice curvature across a given

band. This means, all of the dislocations in a given band can be thought of as SSDs since GNDs would require some net lattice curvature. In other words, there will be an equal amount of positive and negative dislocations in the opposing boundaries on either side of the band

In terms of what are the thin pointed bands observed in the BSE image (Figure 4.17b and Figure 4.18a) and EBSD maps (Figure 4.20 and Figure 4.22), the analysis from this work is that they are most likely twins. Twinning in bcc metals is said to occur on {112} [7, 105–109], however, the thin bands could not be related to any {112} planes. Regardless, the thin bands resemble twins visually due to their thin needle like structure and quantitatively show significant and immediate change in orientation across a boundary of about 7.3° and 10.2°.

6 Conclusions

The resulting topographies from indentation show that topography is a function of crystal orientation. While CPFEM also shows the same symmetry for indent topography for some indents, it does not for all. For CPFEM to be fully utilized as tool of understanding nanoindentation in bcc Ta the structure evolution parameters need to be optimized and the non-Schmid effects need to be properly implemented into the phenomenological model.

This work has demonstrated that individual grain boundaries have different response to strain depending on the side of the grain boundary from which the strain is approaching. To that point, using a single *m'* value to represent the susceptibility of a grain boundary to accommodating deformation is inadequate. With the three different grain boundaries that were targeted, this worked showed four different combinations of deformation response at grain boundaries. They include: (1) significant transfer and significant resistance, (2) significant transfer and little to no resistance, (3) little to no transfer and significant resistance, or (4) little to no transfer and little to no resistance.

ECCI and CC-EBSD reveal very similar dislocation distributions associated with nanoindentation deformation. While there is not a one-to-one correlation between maps from these two techniques, the dislocation densities measured by ECCI are generally similar to those determined by CC-EBSD. The discrepancies between the two techniques may be in part due to inferior spatial resolution of CC-EBSD, allowing for CC-EBSD to miss dipole arrangements, and the potential for ECCI to miss dislocations that are either under invisibility conditions or are in areas that have too many dislocations to image. Despite these minor discrepancies, the strong correlation in distributions, densities, and characterization of dislocations determined by the two techniques suggest that CC-EBSD can be used with confidence for characterizing GND

structures with higher dislocation densities than those that can be imaged using ECCI. At the other extreme, this work suggests that CC- EBSD has the potential to resolve individual dislocations, but cannot do so at this time with high confidence in deformed metallic materials.

This work also shows that combination of nanoindentation, AFM, ECCI, and CC-EBSD is a great method for investigating deformation at grain boundaries. Nanoindentation is a good tool for probing specific areas of material, such as grain boundaries, so that the directionality of strain can be easily known. AFM shows evidence of dislocations that have already exited the crystal with an out-of-plane component, while ECCI and CC-EBSD show dislocations that are still in the crystal. Of course, nanoindentation, AFM, ECCI, and CC-EBSD all have limitations and these limitations need to be understood in order to fully utilize these methods.

This work discovered thin needle like bands that developed by way of plane strain under wedge indentation. These thin bands resemble twins both visually due to their thin needle like features and quantitatively due to their high amount of disorientation across the boundary. Drawing a line from the tip of where the indent was made divides the EBSD data set in half. The thin bands on the left side rotated the original crystal orientation counter clockwise and the thin bands on the right rotated the crystal clockwise. Due to the fact that the alternating banding leaves no residual lattice curvature, it is concluded all dislocations within a given band are SSDs.

6.1 Suggestions for Future Research

It would be advantageous to know what dislocation are involved in the development of topographical lobes that result from indentation. Is it primarily edge dislocations or screw dislocations? To do this AFM, ECCI, and CC-EBSD can be performed on nanoindents that were made with in the same large grain at varying loads. The first indentation to be analyzed would be an indentation that is stopped right after the initial pop-in, i.e. where plasticity begins.

Another worthwhile study would be doing AFM and CC-EBSD on a large number of indentations to see which grain boundaries exhibit deformation and which side of the grain boundary dislocation pile-ups are found. Many places in the literature show that dislocations are found in the parent grain and examples in this work show dislocation pile-ups in the neighboring grain.

Future work should be done to identify the dislocations generated between the thin bands formed form wedge indentation. This can be done using the previously mentioned Zeiss Auriga SEM because it has the capabilities to obtain channeling patterns form and area of ~500 nm [68]. It would also be advantageous to do CC-EBSD at a fine step size between the bands to achieve a clearer assessment of GNDs vs. SSDs inside the thick and thin bands.

REFERENCES

REFERENCES

[1] E. Schmid, W. Boas, PLASTICITY OF CRYSTALS, Springer, Berlin, 1935. https://pdfs.semanticscholar.org/d1e2/e7febcb03f66d7ab79c7bda5bdfb34966ff4.pdf (accessed January 11, 2018).

[2] O. Lohne, On the failure of Schmid's law, Phys. Status Solidi. 25 (1974) 709–716. doi:10.1002/pssa.2210250241.

[3] V. Vitek, Structure of dislocation cores in metallic materials and its impact on their plastic behaviour, Prog. Mater. Sci. 36 (1992) 1–27. doi:10.1016/0079-6425(92)90003-P.

[4] C.L. Briant, New applications for refractory metals, JOM. 52 (2000) 36–36. doi:10.1007/s11837-000-0098-9.

[5] R.W. Buckman, New Applications for Tantalum and Tantalum Alloys, JOM. (2000) 40–41. doi:10.1007/s11837-000-0100-6.

[6] Z. Shen, R.H. Wagoner, W.A.T. Clark, Dislocation and grain boundary interactions in metals, Acta Metall. 36 (1988) 3231–3242. doi:10.1016/0001-6160(88)90058-2.

[7] D. Hull, D.J. Bacon, Introduction to dislocations, Butterworth-Heinemann, 2011. https://www.sciencedirect.com/science/book/9780080966724 (accessed January 11, 2018).

[8] C. Barrett, Sturcture of Metals: Crystallographic Methods, Principles, and Data, McGraw-Hill Book Company, Inc., 1943.

[9] B.A. Simkin, B.C. Ng, M.A. Crimp, T.R. Bieler, Crack opening due to deformation twin shear at grain boundaries in near-γ TiAl, Intermetallics. 15 (2007) 55–60. doi:10.1016/j.intermet.2006.03.005.

[10] H. Li, C.J. Boehlert, T.R. Bieler, M.A. Crimp, Analysis of slip activity and heterogeneous deformation in tension and tension-creep of Ti–5Al–2.5Sn (wt %) using in-situ SEM experiments, Philos. Mag. 92 (2012) 2923–2946. doi:10.1080/14786435.2012.682174.

[11] H. Li, D.E. Mason, T.R. Bieler, C.J. Boehlert, M.A. Crimp, Methodology for estimating the critical resolved shear stress ratios of α-phase Ti using EBSD-based trace analysis, Acta Mater. 61 (2013) 7555–7567. doi:10.1016/J.ACTAMAT.2013.08.042.

[12] V. Vitek, V. Paidar, Chapter 87 Non-planar Dislocation Cores: A Ubiquitous Phenomenon Affecting Mechanical Properties of Crystalline Materials, Dislocations in Solids. 14 (2008) 439–514. doi:10.1016/S1572-4859(07)00007-1.

[13] T.C. Lee, I.M. Robertson, H.K. Birnbaum, Prediction of slip transfer mechanisms across grain boundaries, Scr. Metall. 23 (1989) 799–803. doi:10.1016/0036-9748(89)90534-6.

[14] J. Luster, M.A. Morris, Compatibility of deformation in two-phase Ti-Al alloys: Dependence on microstructure and orientation relationships, Metall. Mater. Trans. A. 26 (1995) 1745–1756. doi:10.1007/BF02670762.

[15] T.B. Britton, D. Randman, A.J. Wilkinson, Nanoindentation study of slip transfer phenomenon at grain boundaries, J. Mater. Res. 24 (2009) 607–615. doi:10.1557/jmr.2009.0088.

[16] W.A. Soer, K.E. Aifantis, J.T.M. De Hosson, Incipient plasticity during nanoindentation at grain boundaries in body-centered cubic metals, Acta Mater. 53 (2005) 4665–4676. doi:10.1016/j.actamat.2005.07.001.

[17] L. Wang, Y. Yang, P. Eisenlohr, T.R. Bieler, M.A. Crimp, D.E. Mason, Twin nucleation by slip transfer across grain boundaries in commercial purity titanium, Metall. Mater. Trans. A Phys. Metall. Mater. Sci. 41 (2010) 421–430. doi:10.1007/s11661-009-0097-6.

[18] L. Wang, R.I. Barabash, Y. Yang, T.R. Bieler, M.A. Crimp, P. Eisenlohr, W. Liu, G.E. Ice, Experimental Characterization and Crystal Plasticity Modeling of Heterogeneous Deformation in Polycrystalline α-Ti, Metall. Mater. Trans. A. 42 (2011) 626–635. doi:10.1007/s11661-010-0249-8.

[19] Z. Shen, R.H. Wagoner, W.A.T. Clark, Dislocation pile-up and grain boundary interactions in 304 stainless steel, Scr. Metall. 20 (1986) 921–926. doi:10.1016/0036-9748(86)90467-9.

[20] T.R. Bieler, P. Eisenlohr, F. Roters, D. Kumar, D.E. Mason, M.A. Crimp, D. Raabe, The role of heterogeneous deformation on damage nucleation at grain boundaries in single phase metals, Int. J. Plast. 25 (2009) 1655–1683. doi:10.1016/j.ijplas.2008.09.002.

[21] L.L. Hsiung, On the mechanism of anomalous slip in bcc metals, Mater. Sci. Eng. A. 528 (2010) 329–337. doi:10.1016/j.msea.2010.09.017.

[22] Z.Q. Wang, I.J. Beyerlein, An atomistically-informed dislocation dynamics model for the plastic anisotropy and tension-compression asymmetry of BCC metals, Int. J. Plast. 27 (2011) 1471–1484. doi:10.1016/j.ijplas.2010.08.011.

[23] C.R. Weinberger, B.L. Boyce, C.C. Battaile, Slip planes in bcc transition metals, Int. Mater. Rev. 58 (2013) 296–314. doi:10.1179/1743280412Y.0000000015.

[24] D. Raabe, Simulation of rolling texture of b.c.c. metals considering grain interaction and crystaloraphic slip on {100}, {112} and {123} planes, Mater. Sci. Eng. A. 197 (1995) 31–37. doi:10.1016/0921-5093(94)09770-4.

[25] W. Wasserbäch, Anomalous Slip in High-Purity Niobium and Tantalum Single Crystals, Phys. Status Solidi. 147 (1995) 417–446. doi:10.1002/pssa.2211470213.

[26] A. Seeger, Why anomalous slip in bcc metals?, Mater. Sci. Engng A. 319–321 (2001) 254–260.

[27] G.I. Taylor, The Deformation of Crystals of β -Brass, Proc. R. Soc. London. Ser. A, Contain. Pap. a Math. Phys. Character. 118 (n.d.) 1–24. doi:10.2307/94885.

[28] J.W. Christian, Some surprising features of the plastic deformation of body-centered cubic metals and alloys, Met. Trans. A. 14A (1983) 1237–1256. doi:10.1007/BF02664806.

[29] R. Gröger, A.G. Bailey, V. Vitek, Multiscale modeling of plastic deformation of molybdenum and tungsten: I. Atomistic studies of the core structure and glide of 1/2 <1 1 1> screw dislocations at 0 K, Acta Mater. 56 (2008) 5401–5411. doi:10.1016/j.actamat.2008.07.018.

[30] R. Gröger, V. Racherla, J.L. Bassani, V. Vitek, Multiscale modeling of plastic deformation of molybdenum and tungsten: II. Yield criterion for single crystals based on atomistic studies of glide of 1 / 2 <111> screw dislocations, Acta Mater. 56 (2008) 5412–5425. doi:10.1016/j.actamat.2008.07.037.

[31] V. Vitek, M. Mrovec, J.L. Bassani, Influence of non-glide stresses on plastic flow: From atomistic to continuum modeling, Mater. Sci. Eng. A. 365 (2004) 31–37. doi:10.1016/j.msea.2003.09.004.

[32] C. Zambaldi, Y. Yang, T.R. Bieler, D. Raabe, Orientation informed nanoindentation of α-titanium: Indentation pileup in hexagonal metals deforming by prismatic slip, J. Mater. Res. 27 (2012) 356–367. doi:10.1557/jmr.2011.334.

[33] M.M. Biener, J. Biener, A.M. Hodge, A. V. Hamza, Dislocation nucleation in bcc Ta single crystals studied by nanoindentation, Phys. Rev. B - Condens. Matter Mater. Phys. 76 (2007) 1–6. doi:10.1103/PhysRevB.76.165422.

[34] W. Zielinski, H. Huang, W.W. Gerberich, Microscopy and microindentation mechanics of single crystal Fe−3 wt. % Si: Part II. TEM of the indentation plastic zone, J. Mater. Res. 8 (1993) 1300–1310. doi:10.1557/JMR.1993.1300.

[35] D. Wu, T.G. Nieh, Incipient plasticity and dislocation nucleation in body-centered cubic chromium, Mater. Sci. Eng. A. 609 (2014) 110–115. doi:10.1016/j.msea.2014.04.107.

[36] D. Wu, J.R. Morris, T.G. Nieh, Effect of tip radius on the incipient plasticity of chromium studied by nanoindentation, Scr. Mater. 94 (2015) 52–55. doi:10.1016/j.scriptamat.2014.09.017.

[37] A.C. Fischer-Cripps, Contact Mechanics, in: 2004: pp. 1–20. doi:10.1007/978-1-4757-5943-3_1.

[38] K. V. Rajulapati, M.M. Biener, J. Biener, A.M. Hodge, Temperature dependence of the plastic flow behavior of tantalum, Philos. Mag. Lett. 90 (2010) 35–42. doi:10.1080/09500830903356893.

[39] W.A. Soer, J.T.M. De Hosson, Detection of grain-boundary resistance to slip transfer using nanoindentation, 2005. doi:10.1016/j.matlet.2005.03.075.

[40] M.G. Wang, A.H.W. Ngan, Indentation strain burst phenomenon induced by grain boundaries in niobium, J. Mater. Res. 19 (2004) 2478–2486. doi:10.1557/JMR.2004.0316.

[41] P.C. Wo, A.H.W. Ngan, Investigation of slip transmission behavior across grain boundaries in polycrystalline Ni3Al using nanoindentation, J. Mater. Res. 19 (2004) 189–201. doi:10.1557/jmr.2004.0023.

[42] Y. Su, C. Zambaldi, D. Mercier, P. Eisenlohr, T.R. Bieler, M.A. Crimp, Quantifying deformation processes near grain boundaries in α titanium using nanoindentation and crystal plasticity modeling, Int. J. Plast. 86 (2016) 170–186. doi:10.1016/j.ijplas.2016.08.007.

[43] K.L. Johnson, Contact Mechanics, Cambridge University Press, Cambridge, 1985. doi:10.1017/CBO9781139171731.

[44] D. Kramer, H. Huang, M. Kriese, J. Robach, J. Nelson, A. Wright, D. Bahr, W.W. Gerberich, Yield strength predictions from the plastic zone around nanocontacts, Acta Mater. 47 (1998) 333–343. doi:10.1016/S1359-6454(98)00301-2.

[45] F. Roters, P. Eisenlohr, L. Hantcherli, D.D. Tjahjanto, T.R. Bieler, D. Raabe, Overview of constitutive laws, kinematics, homogenization and multiscale methods in crystal plasticity finite-element modeling: Theory, experiments, applications, Acta Mater. 58 (2010) 1152–1211. doi:10.1016/j.actamat.2009.10.058.

[46] F. Roters, P. Eisenlohr, T.R. Bieler, D. Raabe, Crystal Plasticity Finite Element Methods, Wiley-VCH Verlag GmbH & Co. KGaA, Weinheim, Germany, 2010. doi:10.1002/9783527631483.

[47] D. Peirce, R.J. Asaro, A. Needleman, An analysis of nonuniform and localized deformation in ductile single crystals, Acta Metall. 30 (1982) 1087–1119. doi:10.1016/0001-6160(82)90005-0.

[48] H. Lim, J.D. Carroll, C.C. Battaile, T.E. Buchheit, B.L. Boyce, C.R. Weinberger, Grain-scale experimental validation of crystal plasticity finite element simulation of tantalum oligocrystals, Int. J. Plast. 60 (2014) 1–18.

[49] S. Becker, R.; Panchanadeeswaran, Effects of grain interactions on deformation and local texture in polycrystals, Acta Metall. Mater. 43 (1995) 2701–2719.

[50] F. Roters, P. Eisenlohr, C. Kords, D.D. Tjahjanto, M. Diehl, D. Raabe, DAMASK: The düsseldorf advanced material simulation kit for studying crystal plasticity using an fe based or a spectral numerical solver, Procedia IUTAM. 3 (2012) 3–10. doi:10.1016/j.piutam.2012.03.001.

[51] A. Koester, A. Ma, A. Hartmaier, Atomistically informed crystal plasticity model for bcc iron, Acta Mater. 60 (2012) 3894–3901.

[52] R. Gröger, V. Vitek, Multiscale modeling of plastic deformation of molybdenum and tungsten. III. Effects of temperature and plastic strain rate, Acta Mater. 56 (2008) 5426–5439. doi:10.1016/J.ACTAMAT.2008.07.027.

[53] MATLAB - MathWorks, (n.d.). https://www.mathworks.com/products/matlab.html.

[54] D. Mercier, C. Zambaldi, T.R. Bieler, A Matlab toolbox to analyze slip transfer through grain boundaries, IOP Conf. Ser. Mater. Sci. Eng. 82 (2015) 12090. doi:10.1088/1757-899X/82/1/012090.

[55] D. Mercier, czambaldi, RaulSanchezMartin, Claudio, techfips, stabix: STABiX v1.6.3, (2015). doi:10.5281/ZENODO.14854.

[56] Python, https://www.python.org/.

[57] Marc - Advanced Nonlinear Simulation Solution, http://www.mscsoftware.com/product/marc.

[58] Abaqus Unified FEA - SIMULIA™ by Dassault Systèmes®, https://www.3ds.com/products-services/simulia/products/abaqus/.

[59] B.L. Adams, S.I. Wright, K. Kunze, Orientation imaging: The emergence of a new microscopy, Metall. Trans. A. 24 (1993) 819–831. doi:10.1007/BF02656503.

[60] A.J. Schwartz, M. Kumar, B.L. Adams, eds., Electron Backscatter Diffraction in Materials Science, Springer US, Boston, MA, 2000. doi:10.1007/978-1-4757-3205-4.

[61] S. NISHIKAWA, S. KIKUCHI, Diffraction of Cathode Rays by Mica, Nature. (1928). doi:10.1038/1211019a0.

[62] M.N. Alam, M. Blackman, D.W. Pashley, High-Angle Kikuchi Patterns, Proc. R. Soc. A Math. Phys. Eng. Sci. (1954). doi:10.1098/rspa.1954.0017.

[63] S. Wright, M. Nowell, J. Basinger, Precision of EBSD based Orientation Measurements, Microsc. Microanal. 17 (2011) 406–407. doi:10.1017/S143192761100290X.

[64] Hikari EBSD Camera Series | EDAX, (n.d.). https://www.edax.com/products/ebsd/hikari-ebsd-camera-series.

[65] EBSD Detector Symmetry - Home, (n.d.). http://symmetry.oxford-instruments.com/.

[66] M. Wright, S; Nowell, High speed EBSD, Adv. Mater. Process. (2008) 29–31.

[67] F.J. Humphreys, Grain and subgrain characterisation by electron backscatter diffraction, J. Mater. Sci. 36 (2001) 3833–3854. doi:10.1023/A:1017973432592.

[68] J. Guyon, H. Mansour, N. Gey, M.A. Crimp, S. Chalal, N. Maloufi, Sub-micron resolution selected area electron channeling patterns, Ultramicroscopy. 149 (2015) 34–44. doi:10.1016/j.ultramic.2014.11.004.

[69] P.. A. Ruedl, E; Delavignette, Electron microscopic study of dislocations and fission damage in platinum foils, J. Nucl. Mater. 6 (1962) 46–68.

[70] W.J. Tunstall, P.B. Hirsch, J. Steeds, Effects of surface stress relaxation on the electron microscope images of dislocations normal to thin metal foils, Philos. Mag. 9 (1964) 99–119. doi:10.1080/14786436408217476.

[71] P. Morin, M. Pitaval, D. Besnard, G. Fontaine, Electron–channelling imaging in scanning electron microscopy, Philos. Mag. A. 40 (1979) 511–524. doi:10.1080/01418617908234856.

[72] D.C. Joy, D.E. Newbury, D.L. Davidson, Electron channeling patterns in the scanning electron microscope, J. Appl. Phys. 53 (1982). doi:10.1063/1.331668.

[73] B.A. Simkin, M.A. Crimp, An experimentally convenient configuration for electron channeling contrast imaging, Ultramicroscopy. 77 (1999) 65–75. doi:10.1016/S0304-3991(99)00009-1.

[74] M.A. Crimp, Scanning electron microscopy imaging of dislocations in bulk materials, using electron channeling contrast, Microsc. Res. Tech. 69 (2006) 374–381. doi:10.1002/jemt.20293.

[75] H. Mansour, J. Guyon, M.A. Crimp, N. Gey, B. Beausir, N. Maloufi, Accurate electron channeling contrast analysis of dislocations in fine grained bulk materials, Scr. Mater. 84–85 (2014) 11–14. doi:10.1016/j.scriptamat.2014.03.001.

[76] S. Zaefferer, N. Elhami, Theory and application of electron channeling contrast imaging under controlled diffraction conditions, Acta Mater. 75 (2014) 20–50.

[77] A.J. Wilkinson, G. Meaden, D.J. Dingley, High-resolution elastic strain measurement from electron backscatter diffraction patterns: New levels of sensitivity, Ultramicroscopy. 106 (2006) 307–313. doi:10.1016/j.ultramic.2005.10.001.

[78] A.J. Wilkinson, E.E. Clarke, T.B. Britton, P. Littlewood, P.S. Karamched, High-resolution electron backscatter diffraction: An emerging tool for studying local deformation, J. Strain Anal. Eng. Des. 45 (2010) 365–376. doi:10.1243/03093247JSA587.

[79] J.R. Seal, T. Bieler, M. Crimp, B. Britton, A. Wilkinson, Characterizing Slip Transfer In Commercially Pure Titanium Using High Resolution Electron Backscatter Diffraction (HR-EBSD) and Electron Channeling Contrast Imaging (ECCI), Microsc. Microanal. 18 (2012) 702–703. doi:10.1017/S1431927612005363.

[80] T.J. Ruggles, D.T. Fullwood, Estimations of bulk geometrically necessary dislocation density using high resolution EBSD, Ultramicroscopy. 133 (2013) 8–15. doi:10.1016/j.ultramic.2013.04.011.

[81] F.J. Humphreys, Y. Huang, I. Brough, C. Harris, Electron backscatter diffraction of grain and subgrain structures - Resolution considerations, J. Microsc. 195 (1999) 212–216. doi:10.1046/j.1365-2818.1999.00579.x.

[82] M.A. Crimp, B.A. Simkin, B.C. Ng, Demonstration of the g · b x u = 0 edge dislocation invisibility criterion for electron channelling contrast imaging, Philos. Mag. Lett. 81 (2001) 833–837. doi:10.1080/09500830110088755.

[83] V.I. Nikolaichick, I.I. Khodos, A review of the determination of dislocation parameters using strong- and weak-beam electron microscopy, J. Microsc. 155 (1989) 123–167. doi:10.1111/j.1365-2818.1989.tb02879.x.

[84] J. Ahmed, A.J. Wilkinson, S.G. Roberts, Study of dislocation structures near fatigue cracks using electron channelling contrast imaging technique (ECCI), J. Microsc. 195 (1999) 197–203. doi:10.1046/j.1365-2818.1999.00574.x.

[85] C.J. Gardner, B.L. Adams, J. Basinger, D.T. Fullwood, EBSD-based continuum dislocation microscopy, Int. J. Plast. (2010). doi:10.1016/j.ijplas.2010.05.008.

[86] K.Z. Troost, P. Van Der Sluis, D.J. Gravesteijn, Microscale elastic-strain determination by backscatter Kikuchi diffraction in the scanning electron microscope, Appl. Phys. Lett. (1993). doi:10.1063/1.108758.

[87] J.F. Nye, Some geometrical relations in dislocated crystals, Acta Metall. (1953). doi:10.1016/0001-6160(53)90054-6.

[88] T.J. Ruggles, D.T. Fullwood, J.W. Kysar, Resolving geometrically necessary dislocation density onto individual dislocation types using EBSD-based continuum dislocation microscopy, Int. J. Plast. 76 (2016) 231–243. doi:10.1016/j.ijplas.2015.08.005.

[89] F. Ram, Z. Li, S. Zaefferer, S.M. Hafez Haghighat, Z. Zhu, D. Raabe, R.C. Reed, On the origin of creep dislocations in a Ni-base, single-crystal superalloy: An ECCI, EBSD, and dislocation dynamics-based study, Acta Mater. 109 (2016) 151–161. doi:10.1016/j.actamat.2016.02.038.

[90] A. Vilalta-Clemente, G. Naresh-Kumar, M. Nouf-Allehiani, P. Gamarra, M.A. di Forte-Poisson, C. Trager-Cowan, A.J. Wilkinson, Cross-correlation based high resolution electron backscatter diffraction and electron channelling contrast imaging for strain mapping and dislocation distributions in InAlN thin films, Acta Mater. 125 (2017) 125–135. doi:10.1016/j.actamat.2016.11.039.

[91] C.M.I. Department of Nanometrology, Gwyddion – Free SPM (AFM, SNOM/NSOM, STM, MFM, …) data analysis software, (n.d.). http://gwyddion.net/.

[92] M. Levy, H.E. (Henry E.. Bass, R.R. Stern, V. Keppens, Handbook of elastic properties of solids, liquids, and gases, Academic Press, 2001.

[93] ParaView, (n.d.). https://www.paraview.org/.

[94] Brigham Young University, OpenXY, (2016). https://github.com/BYU-MicrostructureOfMaterials/OpenXY.

[95] T.J. Ruggles, T.M. Rampton, A. Khosravani, D.T. Fullwood, The effect of length scale on the determination of geometrically necessary dislocations via EBSD continuum dislocation microscopy, Ultramicroscopy. 164 (2016) 1–10. doi:10.1016/j.ultramic.2016.03.003.

[96] J.R. Rice, Tensile crack tip fields in elastic-ideally plastic crystals, Mech. Mater. 6 (1987) 317–335. doi:10.1016/0167-6636(87)90030-5.

[97] J.W. Kysar, Y. Saito, M.S. Oztop, D. Lee, W.T. Huh, Experimental lower bounds on geometrically necessary dislocation density, Int. J. Plast. 26 (2010) 1097–1123. doi:10.1016/j.ijplas.2010.03.009.

[98] Y.N. Picard, M.E. Twigg, J.D. Caldwell, C.R. Eddy, M.A. Mastro, R.T. Holm, Resolving the Burgers vector for individual GaN dislocations by electron channeling contrast imaging, Scr. Mater. 61 (2009) 773–776. doi:10.1016/j.scriptamat.2009.06.021.

[99] G. Naresh-Kumar, B. Hourahine, P.R. Edwards, A.P. Day, A. Winkelmann, A.J. Wilkinson, P.J. Parbrook, G. England, C. Trager-Cowan, Rapid nondestructive analysis of threading dislocations in wurtzite materials using the scanning electron microscope, Phys. Rev. Lett. 108 (2012). doi:10.1103/PhysRevLett.108.135503.

[100] M.G. Crimp, M. A.; Hile, J. T.; Bieler, T. R.; Glavicic, Dislocation density measurements in commercially pure titanium using electron channeling contrast imaging, TMS Lett. 1 (2004) 15–16.

[101] J. Jiang, T.B. Britton, A.J. Wilkinson, Measurement of geometrically necessary dislocation density with high resolution electron backscatter diffraction: Effects of detector binning and step size, Ultramicroscopy. 125 (2013) 1–9. doi:10.1016/j.ultramic.2012.11.003.

[102] T.B. Britton, J. Jiang, R. Clough, E. Tarleton, A.I. Kirkland, A.J. Wilkinson, Assessing the precision of strain measurements using electron backscatter diffraction - part 1: Detector assessment, Ultramicroscopy. 135 (2013) 126–135. doi:10.1016/j.ultramic.2013.08.005.

[103] B.L. Adams, J. Kacher, EBSD-based microscopy: Resolution of dislocation density, Comput. Mater. Contin. 14 (2009) 183–194.

[104] M.D. Vaudin, G. Stan, Y.B. Gerbig, R.F. Cook, High resolution surface morphology measurements using EBSD cross-correlation techniques and AFM, Ultramicroscopy. 111 (2011) 1206–1213. doi:10.1016/j.ultramic.2011.01.039.

[105] L.E. Murr, M.A. Meyers, C.-S. Niou, Y.J. Chen, S. Pappu, C. Kennedy, Shock-induced deformation twinning in tantalum, Acta Mater. 45 (1997) 157–175. doi:10.1016/S1359-6454(96)00145-0.

[106] J. Wang, Z. Zeng, C.R. Weinberger, Z. Zhang, T. Zhu, S.X. Mao, In situ atomic-scale observation of twinning- dominated deformation in nanoscale body-centred cubic tungsten, (2015). doi:10.1038/NMAT4228.

[107] A. Ojha, H. Sehitoglu, Twinning stress prediction in bcc metals and alloys, (2014). doi:10.1080/09500839.2014.955547.

[108] Y.M. Wang, A.M. Hodge, J. Biener, A. V. Hamza, D.E. Barnes, K. Liu, T.G. Nieh, Deformation twinning during nanoindentation of nanocrystalline Ta, Appl. Phys. Lett. 86 (2005) 1–3. doi:10.1063/1.1883335.

[109] K.P.D. Lagerlöf, On deformation twinning in b.c.c. metals, Acta Metall. Mater. 41 (1993) 2143–2151. doi:10.1016/0956-7151(93)90384-5.